Estimation of Seismic Parameters by Source Strength Variation

An Experimental Analysis using Valhall Data

Fredrik G Jakobsen

Abstract

In 2008 at SEG's annual meeting Professor Martin Landrø proposed a new way of deriving 4D noise by source strength variation. It was proposed that by shooting two surveys over the exact same area and process the datasets as two surveys in a 4D survey, the sensitivity of the 4D set-up could be determined. Based on this proposal BP Norge decided to shot a test with firing pressure 1750 psi, in contrast to the 2000 psi production pressure. These two datasets constitutes the data analysed in this thesis.

No known work has been done one this type of data and an experimental approach was used in order to find application for the extra information given by varying the source strength.

Several analysis done on the amplitude effect of the pressure variation suggested a less dramatical change in amplitude (around 5%) than the established literature suggested (8.5%). The frequency dependence of the amplitude change has also been investigated and is still not perfectly understood.

Estimation of a noise profile has been done by several different methods suggesting both a continuously increase in noise with depth as well as a more intricate behaviour. The validity of these noise estiamtion are not perfectly understood and care should be given when evaluating the results.

A new method for deriving the formation quality factor is also proposed. This method is considered to have great potential and although the derived quality factors were found to be inconsistent and illogical, it is believed that with better processing and greater source amplitude change this method could be used by the industry.

Sammendrag

I 2008 på det årlige SEG møte foreslo professor Martin Landrø en ny måte å måle 4D støy ved å endre kildestyrke. Forslaget gikk ut på å skyte to seismikklinjer med to forskjellige trykk for så å prossessere linjene som to årganger i en 4D undersøkelse. Ved å analysere 4D bilde laget med disse to undersøkelsene kunne 4D støynivået bli bestemt. Basert på dette forslaget samlet BP Norge inn en ekstra testlinje skutt med 1750 psi samt en linje skutt med produksjonstrykk på 2000 psi. Disse to seismikklinjene danne grunnlaget for analysene i denne oppgaven.

Dette er det første arbeidet gjort med denne type data. Forskjellige typer eksperimentelle metoder ble brukt for å prøve å finne måter å utnytte den ekstra informasjonen gitt ved denne type datasammenligning.

Flere forskjellige metoder ble brukt for å avekke den reelle amplitudeendringen som følge av endring i kildestyrke og de fleste analysene viste en mindre endring i kildevariasjon (ca. 5%) enn det som var utledet fra etablerte formler (8.5%).

Ved hjelp av dataene ble det estimert flere støy-profiler som viste forskjellige tendenser. Både en konsistent økning i støy med dyp samt en mer komplisert støy-profil ble estimert.

Det ble også funnet en ny måte å estimere kvalitetsfaktoren Q på. Potensialet i denne metoden er stort selv om resultatene i denne oppgaven gav flere ulogiske verdier. Ved å prosessere daten bedre og ytterligere øke amplitudeforskjellene vil nøyaktigheten og detaljnivået i denne Q-faktor analysen kunne bli utnyttet med stor suksess i industrien.

Acknowledgement

Contents

List of Figures

ix

List of Tables

1 4D - seismic

1.1 Intro

Taken from the authors project work (Jakobsen 2012).

4D seismic, or time laps seismic, denotes the time as a new dimension in the seismic industry. The technology is based on changes in reservoir properties while it produces and has in the last decades grown to become an important part of the reservoir characterization and production strategies of many hydrocarbon-fields.

As a hydrocarbon-field produces, both the fluid composition and the reservoir pressure are changing. This leads to a change in the physical properties of the reservoir, resulting in a different seismic response over time. These type of responses are related to active production areas in the reservoir, giving rise to many applications. Some of them being:

- Identifying produced areas in the reservoir.

- Locating undrained compartments in the reservoir.

- Optimizing infill-well placement.

- Discriminate between fluid and pressure effects.

- Distinguishing between compacted and non-compacted area of the reservoir.

- Indicating stress changes in the overburden.

- Monitor injected fluids (e.g. water, CO_2 and N_2).

Most of the potential of these applications are more relevant, and more economic, as the complexity of the field increases. It is therefore important to note that time-laps seismic might not be the best tool for managing all reservoirs. In addition to the structural complexity the physical properties of the reservoir-rock is also an important factor in determine the suitability for time-laps seismic. Up to this date, time-laps seismic has almost exclusively been used in the monitoring of siliciclastic reservoirs, with the exception of some chalk fields. Since carbonates in general are stiffer than sandstones, the fluid properties are less dominant in the total rock and time-laps effects would therefore be more subtle.

The first full field time-laps survey done, was on the Gullfaks field in the north sea. This highly complex sandstone field proved to be one of the greatest success stories for the time laps technology. As a joint Statoil-Schlumberger project it compared seismic data after 9

and 10 years of production with the base survey from 1986. The project identified several untouched pockets of oil and calculations have estimated the added value at Gullfaks to be around 1 billion USD (Amundsen and M. Landrø 2007a).

"Petroleum Geoscience: From Sedimentary Environment to Rock Physics, chapter 19" 2010

1.2   Rock Physics

Taken from the authors project work (Jakobsen 2012).

In order to relate and quantify the reservoir changes responsible for changes in the acoustic properties observed in a 4D signal, models are needed. Models that connect the production related variations to changes in the acoustic impedance.
The seismic signal is made up of reflections of the primary source signal, where the magnitude of the reflections are determined by the relative contrast in acoustic impedance (equation 1 and 2).

$$R = \frac{Z_1 - Z_0}{Z_1 + Z_0} \tag{1}$$

Here Z denotes the acoustic impedance.

$$Z = \rho v \tag{2}$$

Where ρ is the rock density and v is the wave velocity in the rock. There are two kind of body waves called s- and p-waves, each with their own velocities and thus, reflection coefficients.

$$v_p = \sqrt{\frac{K + \frac{4}{3}\mu}{\rho}} \qquad v_s = \sqrt{\frac{\mu}{\rho}} \tag{3}$$

$$\rho_{bulk} = \phi \rho_{fluid} + (1 - \phi)\, \rho_{matrix} \tag{4}$$

Where v_p and v_s are the P- and S- wave velocities respectively. The K is the bulk modulus (the rocks resistance to uniform compression) and the μ is the shear modulus (the rocks rigidity to shear strain). Since a fluid is defined as a substance that does not withstand shear stress, the shear modulus is unaffected by fluid changes in the formation. In contrast the bulk modulus are highly effected by the pore fluid properties. A well recognized way

of relating changes in rock bulk modulus to changes in pore fluid is by using the Gassmann model (Gassmann 1951).

$$\frac{K_{sat}}{K_0 - K_{sat}} = \frac{K_{dry}}{K_0 - K_{dry}} + \frac{K_{fl}}{\phi \left(K_0 - K_{fl}\right)} \tag{5}$$

For fluid substitution uses of the Gassmann model, equation 5 could be rewritten as:

$$K_{sat,2} = \frac{K_0}{\left(\frac{K_{sat,1}}{K_0 - K_{sat,1}} - \frac{K_{fluid,1}}{\phi \left(K_0 - K_{fluid,1}\right)} + \frac{K_{fluid,2}}{\phi \left(K_0 - K_{fluid,2}\right)}\right)^{-1} + 1} \tag{6}$$

In equation 5 and 6 the parameters K_{sat}, K_{dry}, K_0 and K_{fluid} are the bulk modulus of respectively: the saturated rock, dry rock, grain mineral and pore fluid. To preform a partial fluid-substitution the bulk modulus for the fluid-mixture has to be calculated using Reuss average.

The bulk modulus is also affected by the pressure of the reservoir. The Hertz-Midlin (Mindlin 1949) is one of the models that are used to quantify how changes in the reservoir pressure affects the seismic response.

$$K_{eff} = \left[\frac{C^2 (1 - \phi)^2 \mu^2}{18\pi^2 (1 - \nu)^2} P\right]^{1/3} \tag{7}$$

$$\mu_{eff} = \frac{5 - 4\nu}{5(2 - \nu)} \left[\frac{3C^2 (1 - \phi)^2 \mu^2}{2\pi^2 (1 - \nu)^2} P\right]^{1/3} \tag{8}$$

were ν and μ are the Poisson ratio and shear modulus of the grain material, C the number of contact points per grain, ϕ is the rock porosity and P is the effective pressure.

Based on these equations it is possible to relate the changes in p-wave reflectivity in a reservoir to changes in both pressure and pore fluid. S-wave reflectivity on the other hand is only affected by the pressure changes (disregarding the minor fluid-density effect given by equation 4). Since most of the 4D surveys are acquired with hydrophones much effort is put in how to differentiate between the pressure and the fluid induced reflectivity changes. For fields with permanent recording cables both the p- and the s-wave response are being recorded. This information could be used to first identify the pressure induced difference by analysing the s-wave data. Then the fluid effect could be extracted from the p-wave data by removing the pressure induced effects found in the s-wave analysis.

It is important to note that in this section only pressure and fluid effects are discussed. There are also other changes in the reservoir that could affect the reflectivity. Such effects are compaction, leading to lower porosity. Also velocity-changes in the overburden could be observed. This could lead to a time shift of the reservoir that could potentially change the observed response.

2   4D - noise

Taken from the authors project work (Jakobsen 2012).

The basis for 4D analysis are the production induced differences in the seismic parameters. Changes in the fluid composition, porosity and layer thickness are being detected while areas with no difference in seismic properties should, in theory, give no 4D signal at all. There are however limitations in how similar two surveys can get. The difference is measured and quantified as 4D noise that impairs the quality. There are several different factors influencing the 4D noise levels including:

- Source and receiver positioning.

- Source repeatability (the guns ability to produce the same signal over time).

- Weather.

- Noise from near-by operations (e.g. seismic or platform related).

- Acquisition set-up (e.g. cables and gun array).

These factors could be divided into two categories, the repeatability of the survey and the background noise level. The repeatability is controlled by how similar two surveys are, and the problem lies in getting the source and receiver to be as similar as possible the base survey in order to eliminate all spacial differences. For the background noise levels the solution is less hands-on. Since most of the sources of background noise is related to external processes it is more difficult to control. These problems are best handled with proper planning (avoid shooting two surveys simultaneously) and patience (waiting for better weather). However waiting on favourable weather conditions are costly and in many cases not practicable.

In order to quantify the 4D-noise level, and thus the 4D quality, it is common to use the normalized root mean square (NRMS)

$$NRMS = 2\frac{RMS(monitor - base)}{RMS(monitor) + RMS(base)} \tag{9}$$

This is usually done in an area where no production induced differences are expected. To quantify the importance of shot location Hydro launched a test survey where they shot 10000 shots in a spiral around the recording down-hole, geophone array. An analysis were made by M. Landrø 1999 where the NRMS levels of shot pairs were compared.
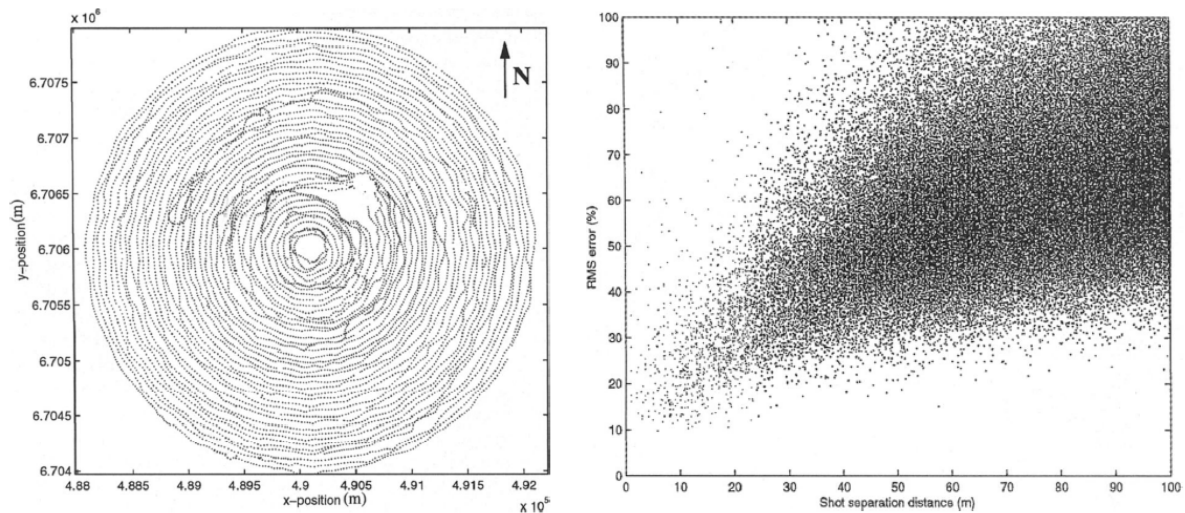
Figure 2.1: Left: Shot geometry of the Oseberg test survey. Right: NRMS meassured between shot pairs plotted as a function of shot separation and RMS error. Both figures from M. Landrø 1999.

Figure 2.1 shows a clear trend in increasing NRMS values with increasing shot distance. In addition a huge increase in the distribution is observed as the shot distance increases. It is important to note that this type of sensitivity study is vastly dependent on the complexity of the local geology and therefore not directly applicable to other areas.

Most of the issues have seen a huge progress since the early 4D experiments. Both the increased navigation accuracy and improved cable steering (bird) technology are important contributors. These technologies makes it possible to more precisely place the vessel and the cables into the desired position. Even though there has been a big increase in repeatability, further progress will be more difficult to improve since the remaining issues are in general more subdivided and harder to control. One such issue is the repeatability of the source. In order to further increase the quality of 4D seismic it is important to have a stable source that allows minimal errors between shots. For permanent receivers the noise mitigation is easier. The receivers are located at the same position as the base survey and the only variable in positioning are the positioning of the source. Also the reduction in seismic equipment needed for a survey, drastically reduces the stand-by cost, making it more affordable to wait for better weather.

3 Previous Work And New Methods

3.1 Noise Estimation by Source Strength Variations

Taken from the authors project work (Jakobsen 2012).

In order to properly managing a 4D project it is important to be aware of what kind of 4D signal we expect. By using rock physics models, as discussed in section 1.2, it is possible to estimate the seismic response of different scenarios. However to completely analyse the feasibility of a given 4D project this is not enough. If the rock physics show that an amplitude variation of 12 % is expected it is important to understand the repeatability of the survey in the terms of 4D noise. If the 4D noise is found to be 15 %, a change in amplitude of 12 % would probably not be detected. This notion of the expected 4D noise could improve the way in which a survey is carried out.

In 2008 at SEG's Annual Meeting M. Landrø proposed a way of calibrating the 4D signal by varying the firing strength. The data for this test is acquired by first shoot one production (standard pressure) line over the field and then repeat the line with a varying source strength(e.g. from 100 % to 50 %) from one end of the line to another. Then process the lines as if they were two lines in a 4D survey. By subtracting the test line from the production line it is possible to quantify the change in amplitude needed to observe a given reflector. This threshold is believed to be varying with depth, and based on this test a 4D-noise-to-depth map could be derived. As a way of controlling the source strength it has been proposed to vary the firing pressure along the shot line in a controlled manner. Another approach to this problem (Barker and M. Landrø 2012) is to shoot several lines with different pressures and analyse them in a similar fashion as mentioned above. This is considered easier to execute, but would lead to a low pressure-resolution, equal to the number of test-lines shot. On another hand the reflectors would be treated spatially equal, and variations in the repeatability along a horizontal reflector could be detected.

Concerns regarding inducing noise with this approach has been evaluated (Barker and M. Landrø 2012) and the biggest concern is related to the change in the bubble time period (equation 10a). It was shown that a delay in the bubble time period could potentially cause a bigger 4D signal than the change in primary amplitude (equation 10b). Since air gun arrays could be arranged in a number of different ways the bubble effect should be evaluated for the specific setup used in the survey.

$$A \sim P^{2/3} \quad \text{(a)} \qquad\qquad T \sim P^{1/3} \quad \text{(b)} \tag{10}$$

In order to extract the 4D noise levels from two different pressure surveys the following method has been used:

$$S_1 = P_1 + n_1 \rightarrow RMS(S_1) = RMS(P_1 + n_1) \tag{11}$$

$$S_2 = P_2 + n_2 \rightarrow RMS(S_2) = RMS(P_2 + n_2) \tag{12}$$

$$[S_1 - S_2] = [P_1 - P_2] + n_3 \rightarrow RMS[S_1 - S_2] = RMS(P_1 + n_3) - RMS(P_2 + n_3) \tag{13}$$

S2 is expected to behave as a scaled in-phase S1 and the relation in 13 is therfore logical sound. The noise term in equation 11 and 12 is contributed to the normal seismic noise that is not strictly 4D related. Equation 13 however also contains the 4D noise since the RMS is derived after subtraction.

$$NRMS_1 = \frac{2(RMS(S_1) - RMS(S_2))}{RMS(S_1) + RMS(S_2)} = \frac{2(RMS(P_1 + n_1) - RMS(P_2 + n_2))}{RMS(P_1 + n_1) + RMS(P_2 + n_2)} \tag{14}$$

$$NRMS_2 = \frac{2RMS[S_1 - S_2]}{RMS(S_1) + RMS(S_2)} = \frac{2\left(RMS(P_1 + n_3) - RMS(P_2 + n_3)\right)}{RMS(P_1 + n_1) + RMS(P_2 + n_2)} \tag{15}$$

By arranging the equations as 14 and 15 shows, two different NRMS values are derived. Both these equations have the same denominator and a subtraction will to some extent remove the P terms resulting in a method to estimate the noise term n_1, n_2 and n_3. This leaves a term dominated by noise and normalized by the average amplitude.

$$Noise \sim NRMS_2 - NRMS_1 \tag{16}$$

$$Noise \sim \frac{RMS(P_1 + n_3) - RMS(P_1 + n_1) + RMS(P_2 + n_2) - RMS(P_2 + n_3)}{\frac{1}{2}(RMS(P_1 + n_1) + RMS(P_2 + n_2))} \tag{17}$$

In this report equation 17 has been used when noise has been derived. This method is not necessarily the ultimate method of deriving the noise from two different pressure-shot surveys, but is considered fairly robust.

8

Table 1: Absorption constants for rocks. From *Explorational Seismology [Utdrag]* 1995

	Q
Sedimentary rocks	20-200
Sandstone	70-130
Shale	20-70
Limestone	50-200
Chalk	135
Dolomite	190
Rocks with gas in pore space	5-50
Metamorphic rocks	200-400
Igneous rocks	75-300

3.2 Q-estimation

In order to extract as accurate information as possible from the ground it is important to know how the signal has been altered on its way through the subsurface. Considering the isotropic case normal alterations would be: geometrical spreading, reflection/transition of part of the energy at interfaces and absorption.

$$A(t) = Pexp(\frac{-\pi ft}{Q}) \tag{18}$$
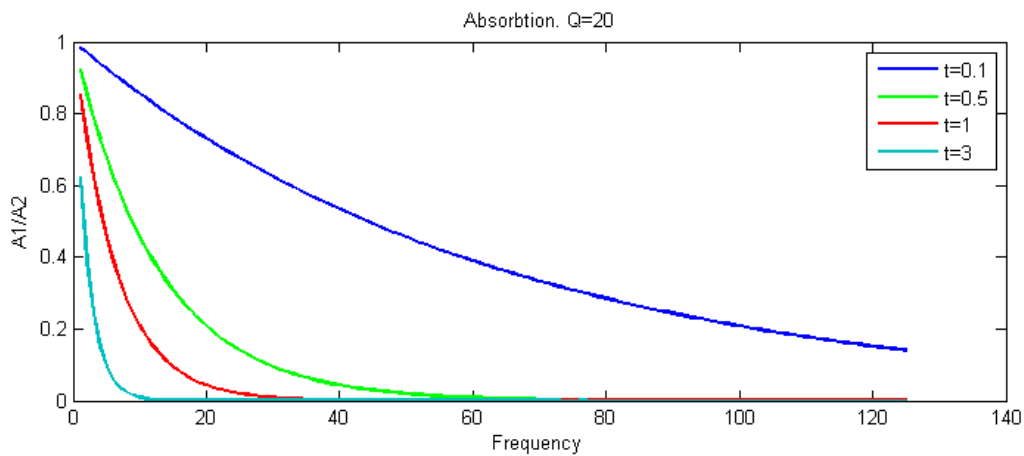
Figure 3.1: Shows absorption as a function of frequency for four different times. Constant Q value 20.

Equation 18 shows how the anelasticity act on the original signal (P) as a function of frequency (f), time (t) and quality factor (Q). This means that the frequency content of a signal is greatly altered as a function of depth. This effect is illustrated by figure 3.1. Normal Q-values are shown in table 1. If this alteration is not properly understood

errors could be made in the evaluation of amplitude data. Analysis such as AVO could be complicated as the absorption effect is superimposed on the AVO effects. The anelastic absorption is determined by several different rock physics properties, such as porosity, saturation and pore pressure. Combined with the geological knowledge of the area this could be used as an additional tool in both exploration and reservoir management, adding valuable information to better interpret the data.

Previous methods of estimating the Q-value has been mainly focused on using VSP (vertical seismic profile) with methods such as spectral ratio evaluation (Stainsby and Worthingtont 1985). By rearranging equation 18 as done in equation 19 it is possible to evaluate the slope of the line $ln(A/P)$ and estimate the Q factor.

$$A = KPexp(\frac{-\pi ft}{Q}) \rightarrow ln\left(\frac{A}{P}\right) = ln(K) - \left(\frac{-\pi ft}{Q}\right) \tag{19}$$

K represents other amplitude altering effects such as geometrical spreading and transition losses. These amplitude effect are independent of frequencies and should, for a given t be treated as constants. The slope of the natural logarithm of the ratio of the reflected spectrum and the emitted spectrum should then give the Q-factor for the given depth.

For this thesis a new method of extracting the Q-factor has been evaluated. Based on an idea by the authors advisor, Martin Landrø (Martin Landrø 2013), this new method utilizes the change in sub-surface response as the amplitude of the source changes.

$$A_1 = KP_1exp(\frac{-\pi ft}{Q_{avg}}) \qquad\qquad A_2 = KP_2exp(\frac{-\pi ft}{Q_{avg}}) \tag{20}$$

$$\Delta A = \left(KP_1exp(\frac{-\pi ft}{Q})\right) - \left(KP_2exp(\frac{-\pi ft}{Q_{avg}})\right) \tag{21}$$

$$ln(\Delta A) = ln\left(K\Delta P\right) - \frac{\pi ft}{Q_{avg}} \tag{22}$$

Equation 22 shows a linear behaviour of ln(ΔA) as a function of frequency with the intersection point f=0 being determined by all other amplitude reducing effects. By evaluating strong reflectors in the seismic, this equation could potentially determine spatial variations in the Q value both in depth and in the plane. These values would give an average Q value from the sea-floor down to the analysed reflector. To calculate Q_{avg} in a layered model equation 23 is used (Bale and Stewart 2002). This equation show that

in order to make $Q_{int} > 0$ (which is the only valid values for Q), equation 24 has to be fulfilled. Instabilities could occur in calculations of Q_{int} if the difference of the two sides in equation 24 gets very small.

$$\frac{1}{Q_{int}^{(n+1)}} = \frac{1}{t^{n+1} - t^n}\left(\frac{t^{n+1}}{Q_{avg}^{n+1}} - \frac{t^n}{Q_{avg}^n}\right) \tag{23}$$

$$\frac{t^{n+1}}{Q_{avg}^{n+1}} > \frac{t^n}{Q_{avg}^n} \tag{24}$$

11

4 Methodology

In this thesis several programs and software packages has been used to derive, manipulate and present the data.

4.1 Promax

For the most of the initial QC and processing work (described in section 7.4), the Promax software has been used. The program offers all the normal processing options with robust filters and comprehensive migration algorithms. Since Promax is designed to handle large seismic survey data it preforms well when it comes to run-time. However, since the program is built for conventional processing of seismic data, it is considered rigid if a more untraditional approach is needed.

4.2 MATLAB

MATLAB is an environment for numerical computation, visualization and programming and since it is unbiased it is also rather flexible. The combination of easy to use built in function and freedom to design new processes has made MATLAB the most used tool in the making of this thesis. It is also worth mentioning that the openness of MATLAB should be approached with care as built in function such as filters and regression are considered as semi black boxes and is not perfectly understood. Even though the processes in Promax has higher degree of black-box feel to it, the processes are intended used on seismic data. All filters and processes used has therefore been thoroughly tested before final use. All plots and most of the figures has been made using the plotting environment of MATLAB.

4.2.1 SegyMAT

SegyMAT (Hansen 2013) is a freeware software package designed to read and write SEG-Y files with MATLAB. The package is easy to use and is comprehensive enough to allow both reading and writing of all seismic data used in this thesis. The package also comes with a simple GUI making the total package an excellent tool for manipulating seismic data within the MATLAB framework. Although SegyMAT has a poor run-time performance compared with Promax, the benefits of working with the datasets in MATLAB compensates for the slow run-time.

4.3   Nucleus

Nucleus is a package of advanced tools for survey planning, seismic modelling and feasibility studies. For this study the marine source modelling module has been used to generate a synthetic response of the source used in the surveys analysed.

5 Frequency spectrum characteristics

An important part of a seismic analysis would contain the evaluation of a frequency spectrum. A frequency spectrum contains information on the frequency contained in the analysed data. It is therefore crucial to understand the different features that usually appears in a seismic frequency spectrum.

If the reflected wavelet was consisting of a perfect peak the resolution would be limited by the sampling interval only. However, since the ground absorbs the signal on a per-cycle basis the higher frequencies are damped much faster than the lower frequencies. The standard sampling rate is therefore 4ms giving a Nyquist frequency of 125 Hz. As mentioned above, a signal consisting of only one sharp spike would contain all frequencies. However if the signal consists of two spikes the frequency content of the signal would be altered as shown in figure 5.1. As this is the case for a marine source due to the ghost, it is important to understand how this effects the frequency content of the signal.
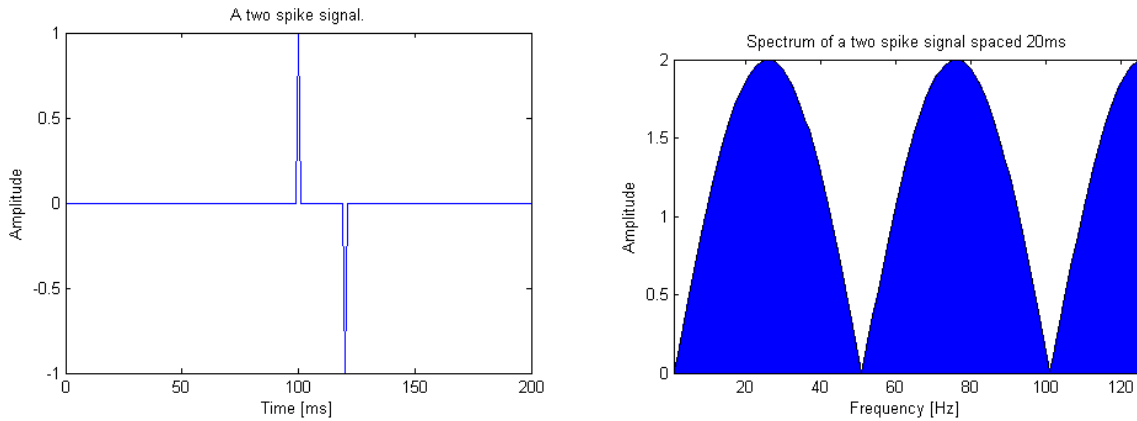
Figure 5.1: Left: Two spikes similar to primary and ghost signal. Right: Frequency spectrum of amplitude response to the right.

Since the most prominent features of an unprocessed seismic signal is the primary and the first multiple arrival (with their ghosts), their effect on the spectrum as a function of offset is investigated. The survey analysed in this work is shot over ocean bottom cables (OBC) and these calculations will therefore reflect an OBC geometry as shown in figure 5.2.

It can be shown, based on the geometry in figure 5.2 that the ray path lengths can be written as:

$$P = \sqrt{x^2 + Z_S^2} \tag{25}$$

15
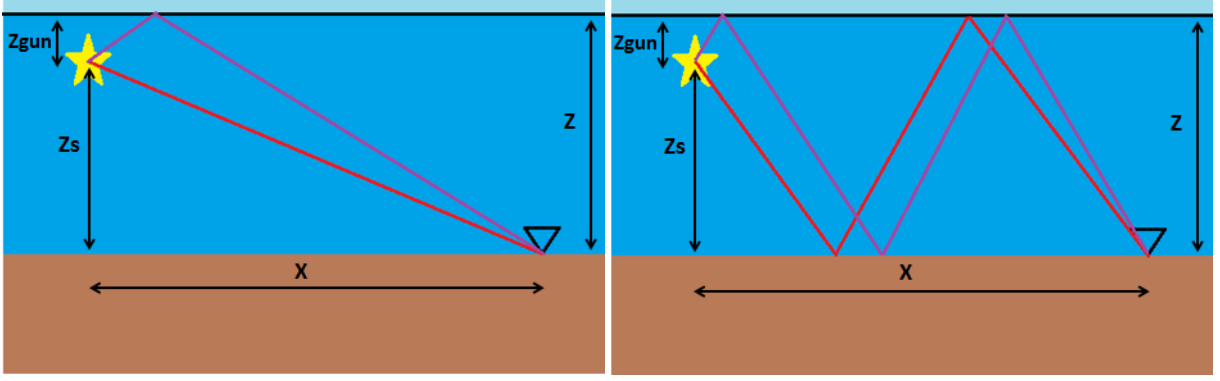
Figure 5.2: Left: Ray paths of the direct arrival (red) with ghost (purple). Right: Ray paths of the first multiple(red) with ghost (purple). Geometry based on ocean bottom cables.

$$P_G = \sqrt{\left(\frac{Z_{gun}x}{Z + Z_{gun}}\right)^2 + Z_{gun}^2} + \sqrt{x - \left(\frac{Z_{gun}x}{Z + Z_{gun}}\right)^2 + Z^2} \tag{26}$$

$$M = \sqrt{\left(\frac{Z_S x}{2Z(1 + Z_{S)}}\right)^2 + Z_S^2} + 2\sqrt{\left(\frac{x - \left(\frac{Z_S x}{Z + Z_S}\right)}{2}\right)^2 + Z^2} \tag{27}$$

$$M_G = \sqrt{\left(\frac{Z_{gun}x}{2Z + Z_{gun}}\right)^2 + Z_{gun}^2} + 3\sqrt{\left(\frac{x - \frac{Z_{gun}x}{2Z + Z_{gun}}}{2}\right)^2 + Z^2} \tag{28}$$

In order to replicate the LoFS14 survey conditions similar parameters has been used: Water velocity of 1500 m/s, 5 m gun depth and water depths of 70 meters. The offset has been varied from 0-100 meters. The amplitude is calculated on a geometrical spreading basis of 1/R. In addition the multiple reflections has been affected by a reflection coefficient set to 0.57 in order to replicate the ocean bottom reflection strength. Figure 5.3 show the signal at 0 and 100 m offset and a low pass filtered version of the whole shot gather. Notice how the peaks move tighter together as the offset increases.

From this, basic model containing only 4 reflections, it is clear that a change in offset alters the characteristics of the signal. Figure 5.4 shows a FX impulse-response of the model shown in figure 5.3. The X value in this plot denotes the offset of the shot. The most prominent result is the stretching of the spectrum-oscillations together with the weakening of the spectrum amplitude. The weakening of the spectrum is expected as the model takes into account geometrical spreading. The "stretching" of the spectrum is also expected as the notches observed in figure 5.1 reflects the time between events with the relation $\frac{1}{P}$ where P is the time between the events. As the offset is increasing, the
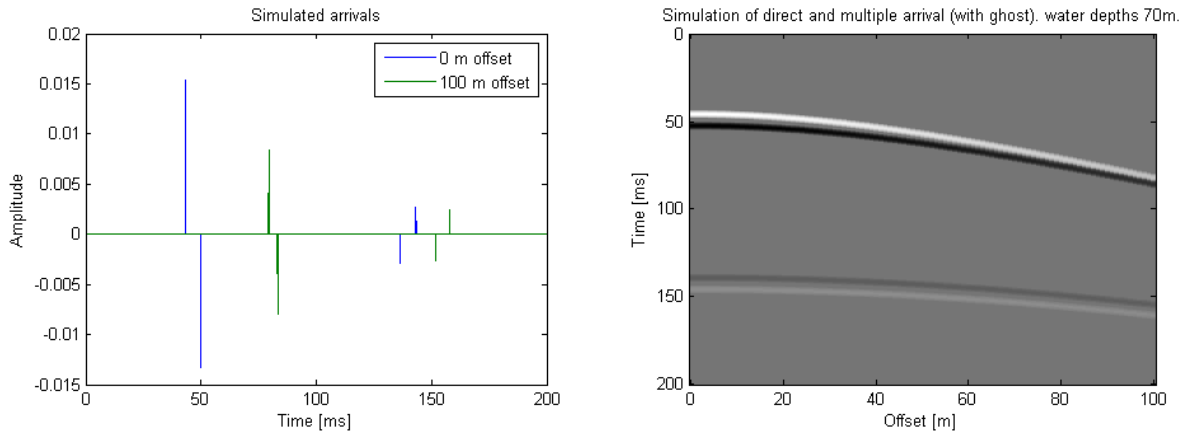
Figure 5.3: Left: Results of the model at 0 (blue) and 100 meter (green) offset. Right: Result of the model from x=0-100 meters.
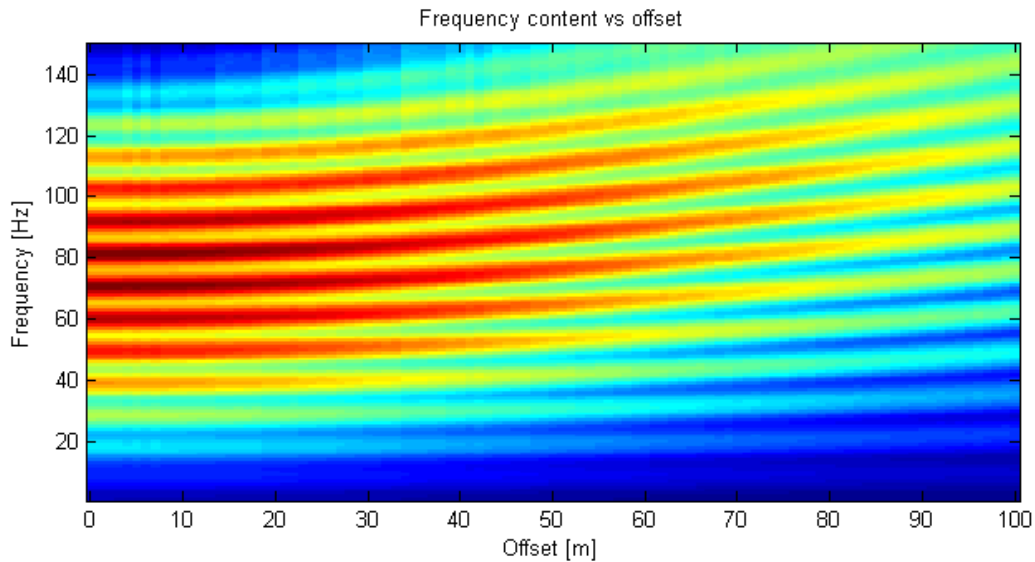
Figure 5.4: FX plot of the results in figure 5.3.

ray-path distance will proximate each other and the delay in spikes will be less, resulting in a broadening of the spectrum notches.

By convolving the impulse model used to create figure 5.4 with the pulse in figure 5.5 the FX-plot in figure 5.6 could be derived.

By adding the bubble the FX plot got one new interesting feature. Two peaks at 11 and 21 Hz which seems unaffected by the offset (disregarding the dimming due to geometrical spreading spreading). These lines are the spectrum signature of the bubble pulse and they can be used to derive the bubble time period. The difference in notch frequency here is 10 Hz witch corresponds to a bubble time period of 100 ms.
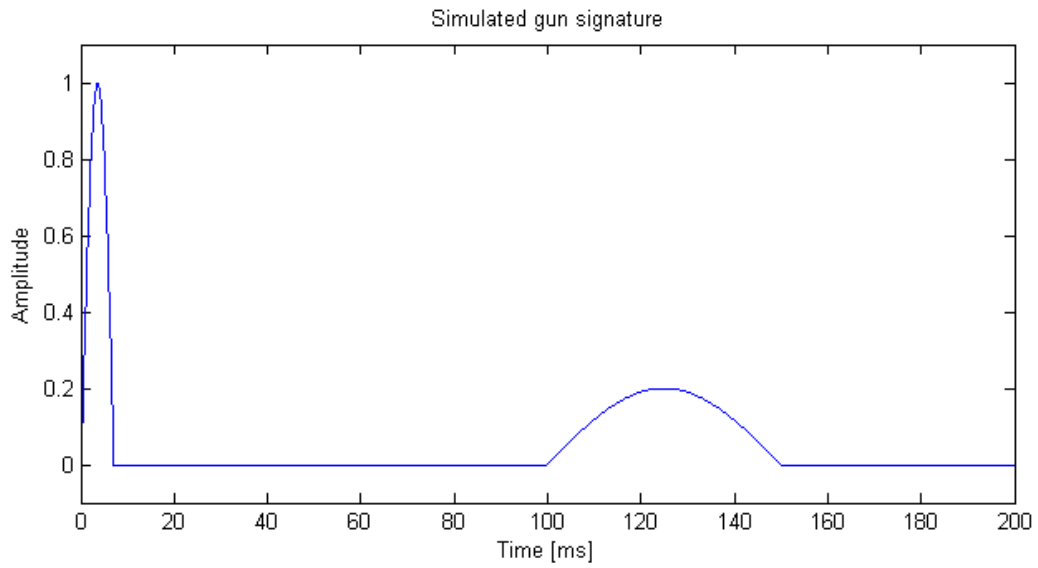
Figure 5.5: Pulse with bubble. Bubble time period 100 ms. Primary-to-bubble ratio=5.
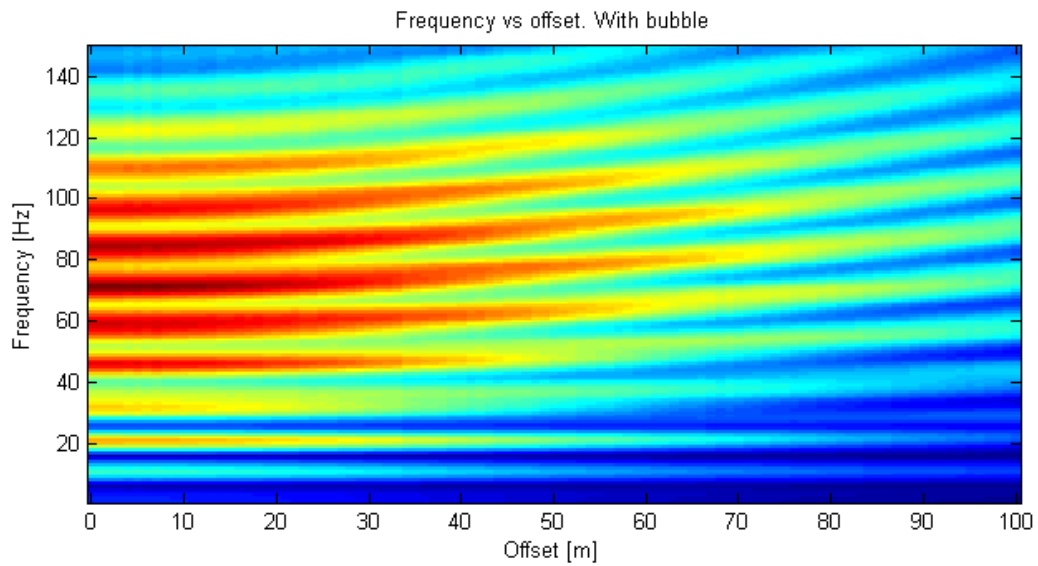
Figure 5.6: FX-plot of model in figure 5.3 convolved with signal in 5.5. Note the addition of bubble notches unaffected by offset.

18

6 Valhall Geology

Modified from the authors project work (Jakobsen 2012).

The Valhall field is located in the southernmost part of the Norwegian North-Sea with water depths of about 70 m. It was discovered in 1975 by Amaco and put into production seven years later in 1982 and is today operated by BP Norge AS with partner Hess Corperation(NPD 2012). With an estimated original oil in place of 2.6 billion MMSTB (O. Barkved et al. 2003) the filed is the historical 8th largest oil discovery on the Norwegian continental shelf. Today, after 30 years of production, Valhall field has the 3rd most recoverable resources still in the ground. The reservoir is at about 2400 meters depth
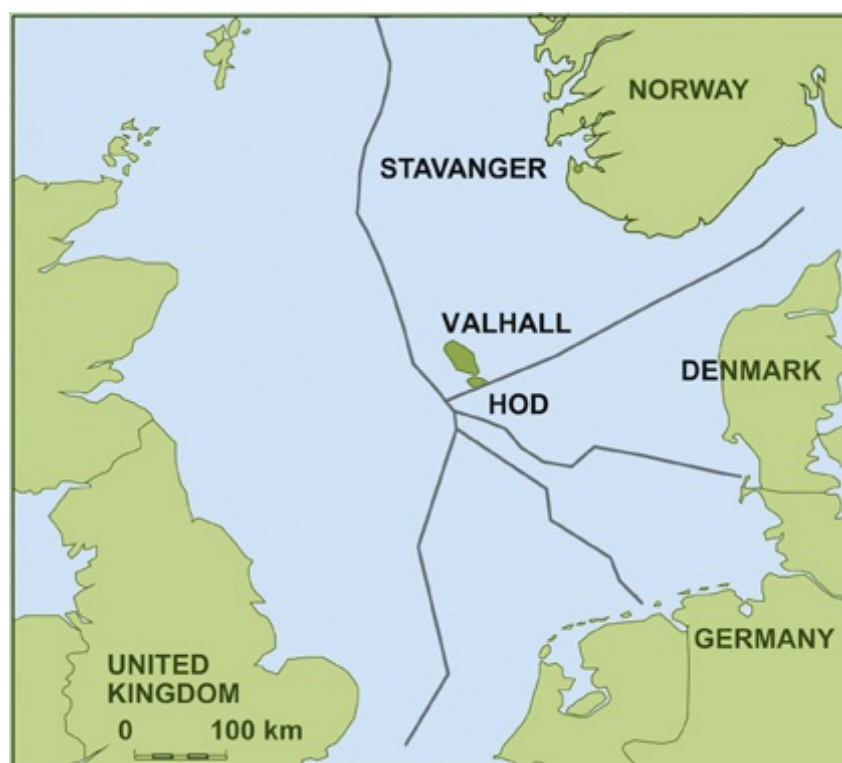
Figure 6.1: Valhall field, located in the North-Sea

and consists of the Late Cretaceous Tor and Hod chalks. Reservoir porosity is excellent ranging from 36 to 50%. Due to the tiny grain size in the chalks, primary permeability is in the order of 1-10 mD. However, due to extensive fracturing the effective permeability is generally much higher, reaching 300 mD in some parts of the reservoir. The chalk is capped by the Rogaland formation shale and sourced by the Kimmeridge Clay. Structurally the field is a gentle anticline with the four way closure extending in excess of 240 km^2 (Munns 1984).

The high porosity is a result of a rapid and early sealing of the reservoir where the Ro-

galand formation sealed of the chalk formations in a way such that formation water was not able to escape, making the formation over-pressured. The pressure helped supporting the increasingly heavier overburden and made it possible for the excellent porosity to be preserved. This has also shown to be a problem in the production of the field as the soft chalk undergoes heavy compaction as the filed is produced and the pressure drops. This compaction is manifested all they way to the sea bottom and could be demonstrated by plotting the sea-floor depth at each receiver at the Valhall field. This has been done in figure 6.2 and it clearly show a synform structure with heaviest subsidence in the Valhall platform area.
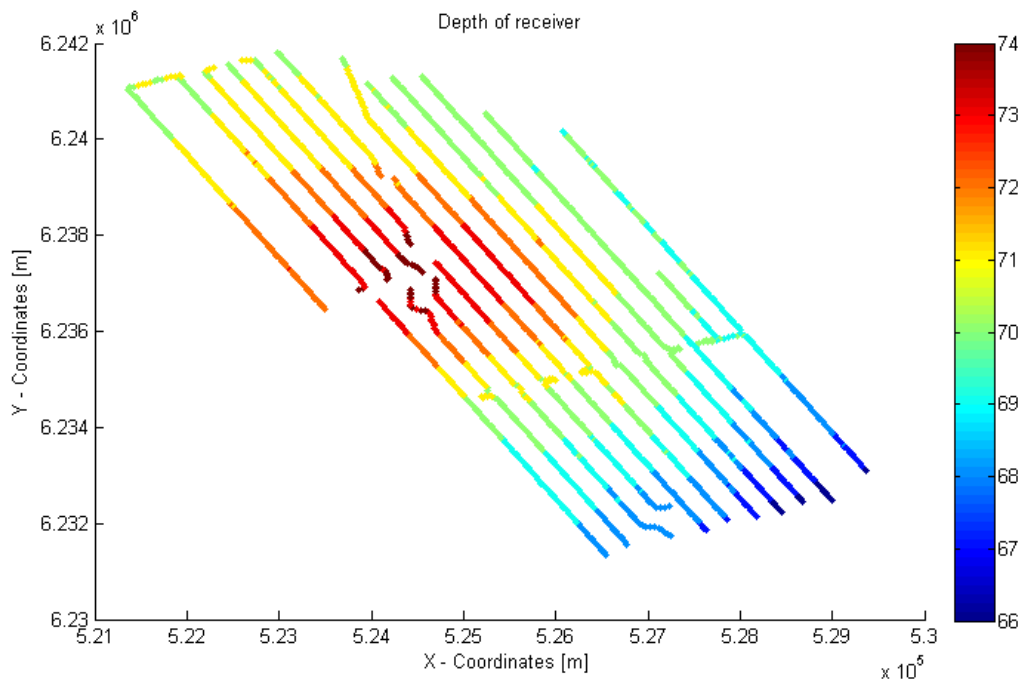
Figure 6.2: Subsidence at Valhall field

7 The Dataset

In 2003 BP Norge AS installed permanent 4C receiver cables on the sea floor. This was the first full field installation of a permanent receiver system on an offshore field (bp.com 2012). Since then there has been shot on average 1.5 surveys a year. The main motivation for doing so was to support the water injection system in the reservoir and improve production well placement as well as identifying unproduced oil pockets within the reservoir (O. I. Barkved, Amundsen, and M. Landrø 2009). In addition the 4C receiver could increase the structural model in the area corrupted by the gas cloud. The data analysed in this report is acquired as a part of the 14 [th] LoFS survey from September 2011.

7.1 Source array setup

The source array used for the LoFS 14 acquisition consists of 20 BOLT Annular Port Guns arranged in 3 sub arrays. The total capacity of the array is of 2000 cubic inches and has a normal operating pressure of 2000 psi. The guns are distributed in a symmetric set-up as shown in figure 7.1. The source depth in both surveys was 5 meters. Synthetic response of this set-up with both production- and test pressure is found in section 8.2.4.
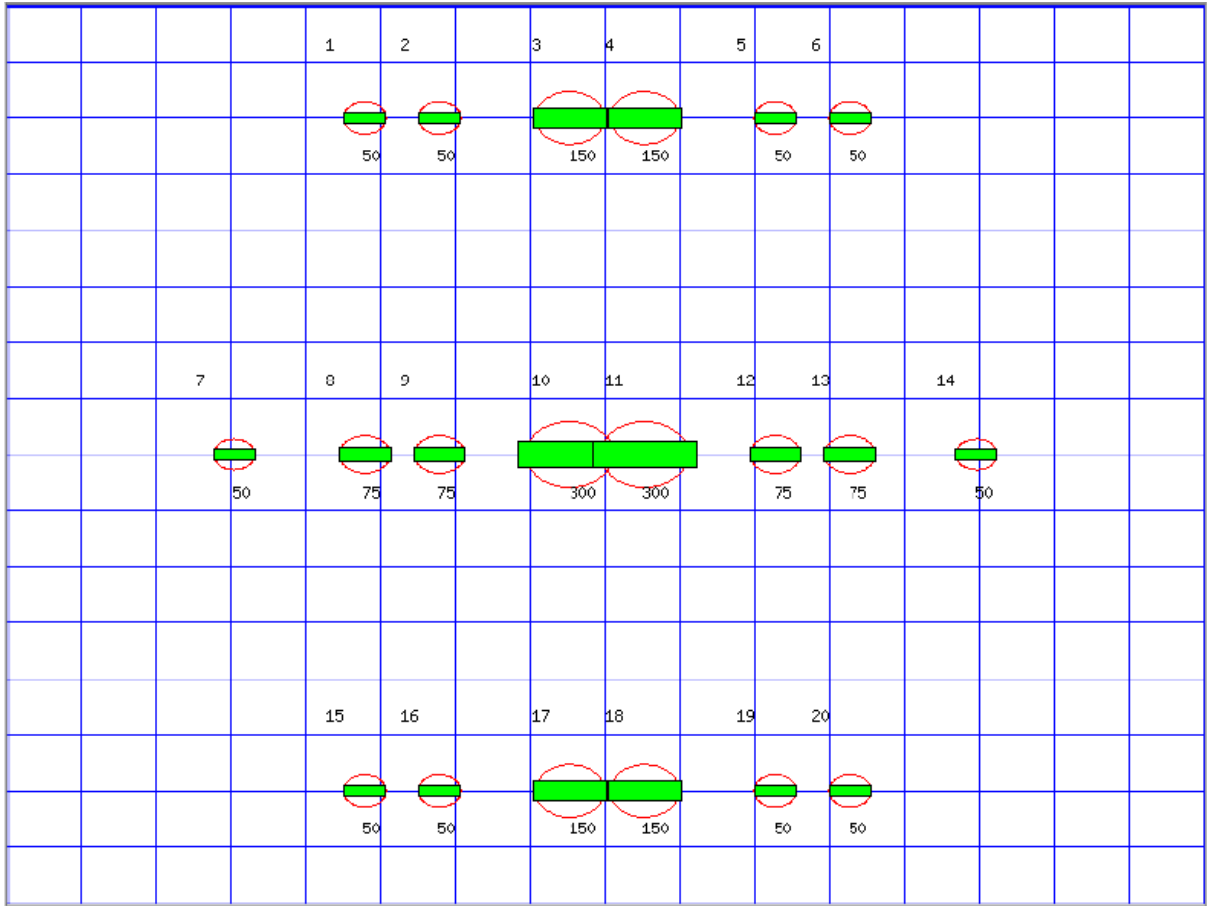
Figure 7.1: Shows the arrangment of guns in the array. Volume of gun in cubic inches. 1m grid, plane view.

7.2 Receivers

The hydrophone receiver used in the LoFS set-up is the *Deepender^{TM} 5000-X Hydrophone* mounted together in a 4C SubSea digitizer and has a pressure rating of 5000psi. More on the receiver in appendix A.

7.3 Acquisition

The dataset analysed contained two shot-lines with all the LoFS receivers recordings, a total of 2414. One production-line shot with a firing pressure of 2000 psi and one test-line shot with a firing pressure of 1750 psi. A total of 200 shots where shot over the same northernmost line of the LoFS set-up in a south-east trending direction with a shot spacing of 50 meters.

As an initial QC, the header values containing the coordinates of the source and receiver was plotted as shown in figure 7.2. From this plot it is possible to identify the receivers containing the desired data to be the north-east most line. It was also discovered that shot number 147 and 148 was missing from the production-line.
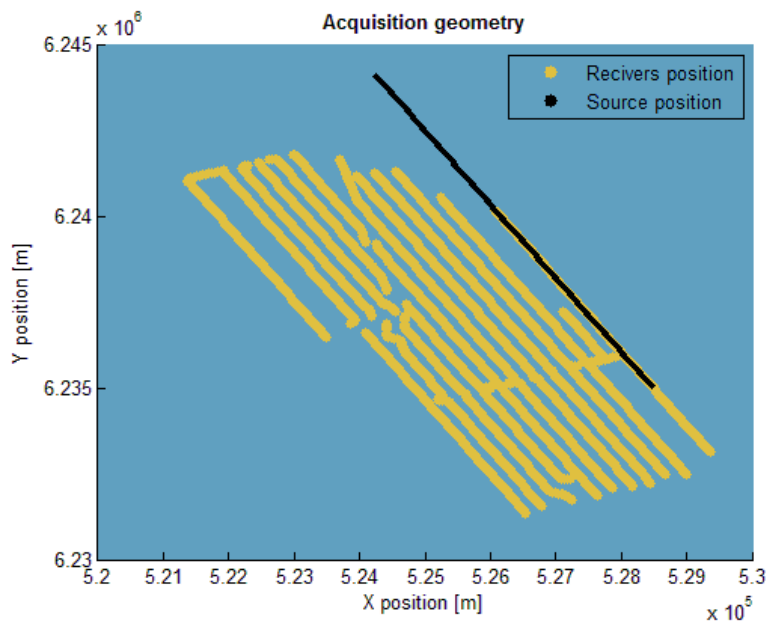
Figure 7.2: Positioning of shot and receivers

For this study, only the data from the receivers located under the shot-line were of interest and it was necessary to confine these. Figure 7.3 shows the receivers used in further analysis. Reducing the total amount of receivers to 157.
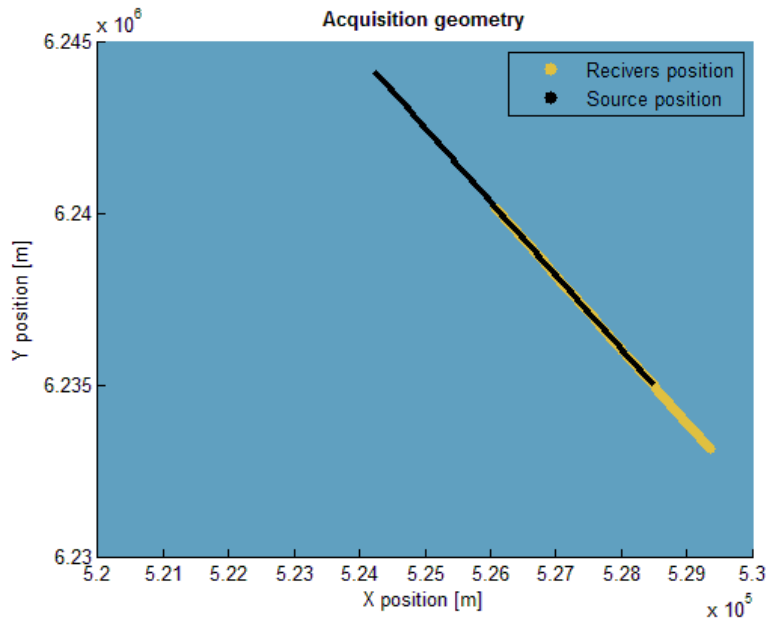
Figure 7.3: Position of receivers used in further analysis together with source position

7.4 Processing

The datasets were both run through two different processing flows as shown in figure 7.4.

Geometry: First the missing shots in the production line were handled by removing the same shots from the test line. The geometry was defined based on the source and receiver locations. Since the distance between both shots and receivers in this survey is 50 meters, the bin size is set to 25 meters. The first shot of the production data (northernmost shot) marks the start of the CMPs and is defining the center of CMP number 1.

Velocity analysis: A supergather is made by combining five traces every tenth, forming the basis for the velocity analysis. The velocities were picked using the production pressure data since it contains stronger reflections and therefore better semblance plots.

NMO correction: NMO correction was applied using the velocities picked in the velocity analysis. Same velocities was used for both lines. A stretch mute percentage of 10 was applied.
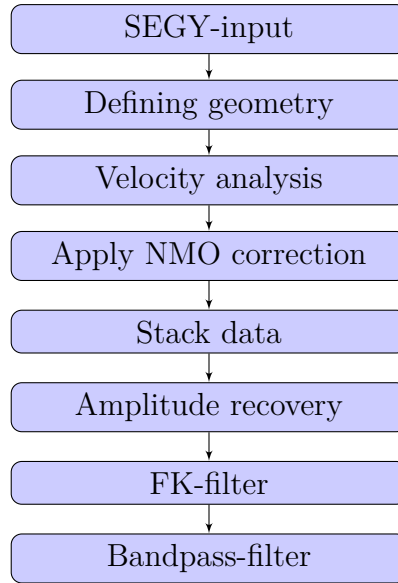
Figure 7.4: Processing flow for the data

Gain: For amplitude recovery a simple model of t^2 was used.

Filters: Due to the fact that most of the seismic reflectors in the stack are pretty horizontal, a FK-dip filter is applied to remove dipping noise in the stack. In addition an Ormsby style bandpass filter is applied with corner frequencies 8-12.5-90-100.

Cross Correlation: In this analysis no time-shift is expected. The cross correlation is therefore calculated between the two stacks in order to get the horizons as similar as possible timewise. The peak of the cross correlation were picked and all peaks deviating from the "zero value" is indicating a tiny time-shift between the two surveys. This deviation is then corrected for on the test stack to increase the similarity of the two lines (figure 7.5).

After the correlation correction a difference stack is made by subtracting the corrected test-stack from the production stack.

Debubble: When the pressure of a source array is changed, it is expected that the period of the bubble is altered (equation 10b). Since the ultimate goal of this pressure variation seismic is to investigate differences between the two surveys a time shift in the bubble will surely generate some 4D noise. This concern has been discussed by Barker and M. Landrø 2012 where it was concluded that due to the diversity of air gun setups the severity of this effect must be evaluated for each survey. Based on the results in
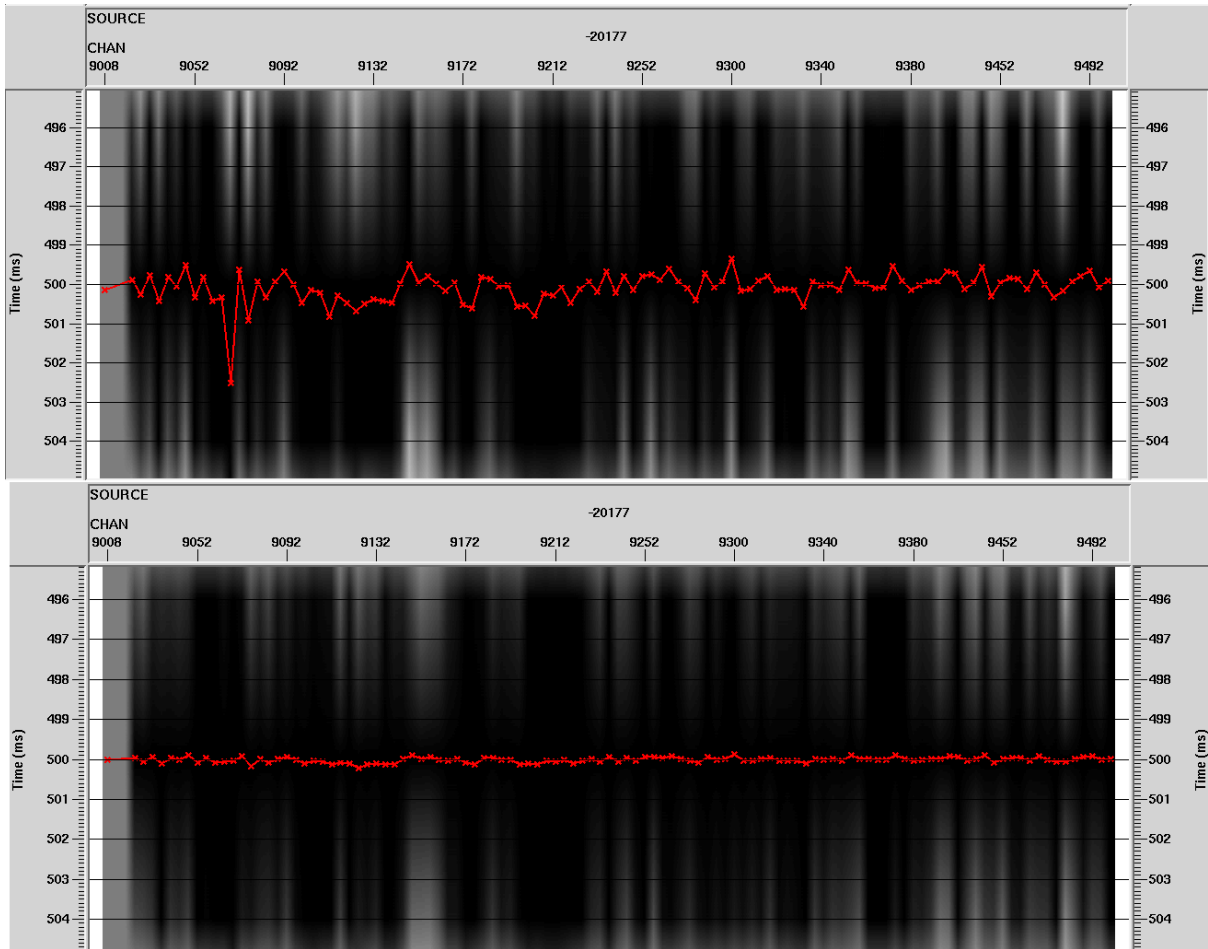
Figure 7.5: Top: Cross correlation between the lines. Bottom: Cross correlation after deviation subtraction.

section 8.2.4. It was found that the bubble-induced noise in this survey is at level with the difference in source strength. It is therefore crucial to remove the bubble in order to get more accurate results. The debubbelfilter was made based on the synthetic response of the source array created in Nucleus (input parameters from section 3.1). Onefor each pressure. The desired response input is the same wavelets, without the reverberations caused by the bubble. Therefore the values after 25 ms on figure 8.37 is put to zero. Then a match filter is derived using the Derive Match Filter function in Promax.

8 Analysis

8.1 Initial data analysis

As mentioned in section 7.3 the two lines analysed are shot with two different (constant) firing pressures as discussed in section 3.1. The data given provides a limited pressure resolution as only one test line is shot. It is still of great interest to investigate if the given amplitude change is substantial enough to be detected in the 4D analysis. It is also of interest to investigate how the 4D noise changes with depth. The production pressure is 2000 psi and the test line is shot with 1750 psi. By using equation 10(a) to calculate the amplitudes it is possible to derive the theoretical variation in the signal as a result of the pressure change.

$$\frac{\Delta A}{A} = \frac{(A_1 - A_2)}{A_1} = \frac{(P_1^{2/3} - P_2^{2/3})}{P_1^{2/3}} = \frac{(2000^{2/3} - 1750^{2/3})}{2000^{2/3}} = 8.5\% \tag{29}$$

The theoretical pressure change should therefore be 8.5%, meaning that the test pressure survey is expected to be scaled down 91.5% compared to the production pressure survey.

This difference should be observable by a mere subtraction of two similar traces. The data used has been derived from near zero-offset shots (offsets 0-25 meters) over the same receiver, with a maximum displacement toleration of 5 meters.
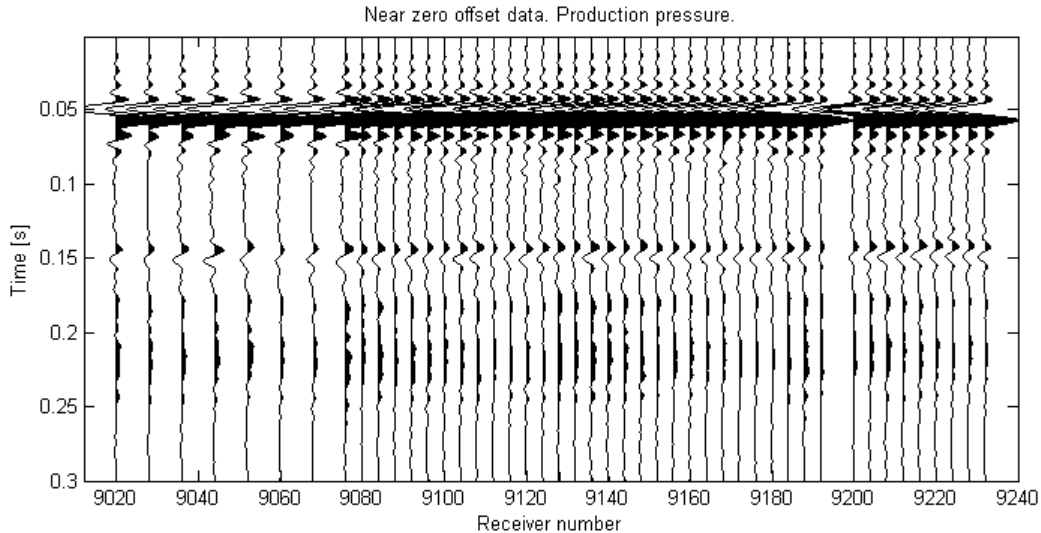
Figure 8.1: Near zero incidence angle direct arrivals from production pressure survey

As seen in figure 8.3 the amplitude difference of the direct arrival seems to be rather weak compared to changes caused by changes in the bubble pulse. It is therefore considered
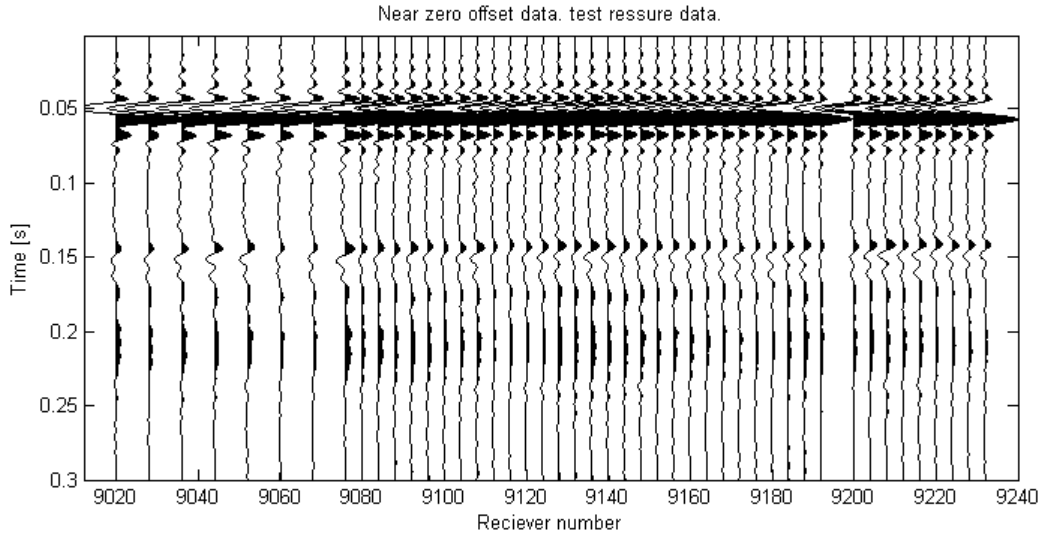
Figure 8.2: Near zero incidence angle direct arrivals from test pressure survey
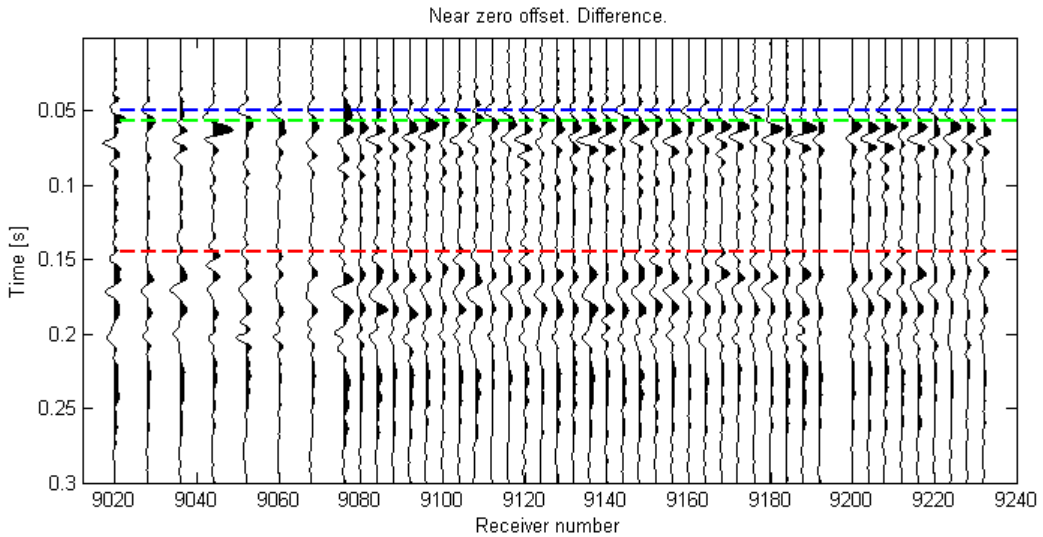
Figure 8.3: Difference plot of figure 8.1 and 8.2. Blue green and red line shows location of direct, ghost and first multiple arrival. Amplitude scale is half of figure 8.1 and 8.2.

important to implement a debubble filter as described in section 7.4.

The effect of a debubble filter is shown in a difference plot in figure 8.4. The plot shows an increased difference in the direct arrival and a reduction in the low frequent bubble noise. Since the two different surveys have a different bubble-pulse they have been run through two different debubble filters to make the signatures more simular (more on the debubble process in section 7.4). By running the surveys through two different filters some concerns are raised towards the integrity of the amplitude variation after debubbling.
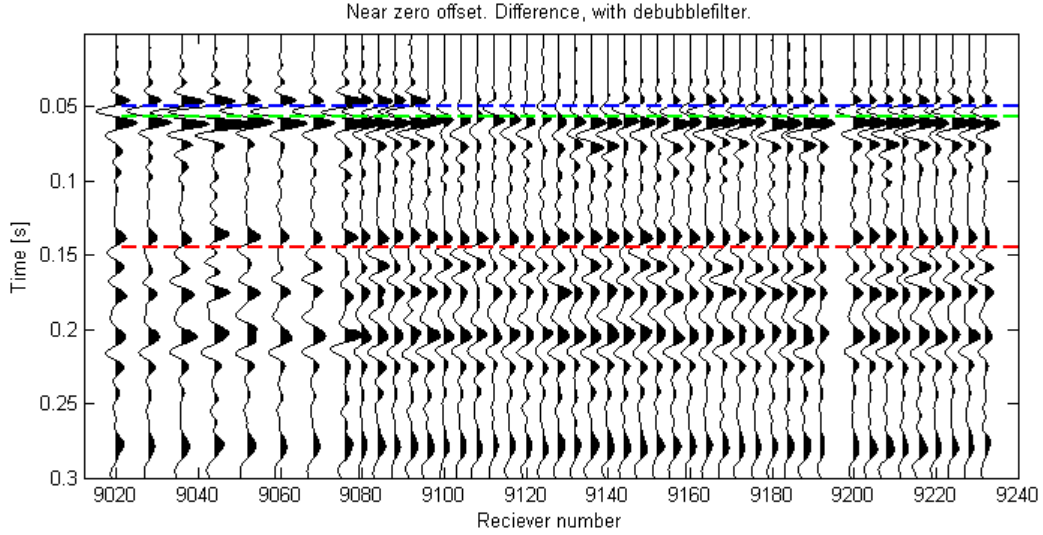
Figure 8.4: Difference plot of figure 8.1 and 8.2. Blue green and red line shows location of direct, ghost and first multiple arrival. Amplitude scale is half of figure 8.1 and 8.2.

8.2 Amplitude Variation

Since no known work has been done on pressure variant surveys, several methods for quantifying the real source difference has been used. These analysis have been conducted on the raw data with no filters or data altering processes applied.

8.2.1 Direct Arrival Analysis

For this analysis the focus has been on comparing the different parts of the direct arrival from each survey with the other. Both the maximum and minimum value, as well as the root mean square value of the direct arrival has been analysed. The data selection used is the same as described in section 8.1. In this dataset the minimum value represents the direct arrival, the maximum value represents the source ghost and the root mean square represents the overall change in amplitude. Initially the minimum value for both surveys are plotted as shown in figure 8.5. It seems like the source is acting very unstable with normal deviation of 40%. When comparing the amplitude data with the offset (figure 8.9) there seems to be a correlation where an offset effect is observable as a gentle lowering in the amplitude towards the middle of the plot. This effect can not explain the more rapid fluctuations demonstrated in the figure. Since this figure compares minimum values on a receiver-by receiver basis, and since the two surveys seems to follow the same trend, speculations are made towards the integrity of the receivers itself. These suspicions are increased when plotting all the analysed features of the wavelet for both 2000- and 1750
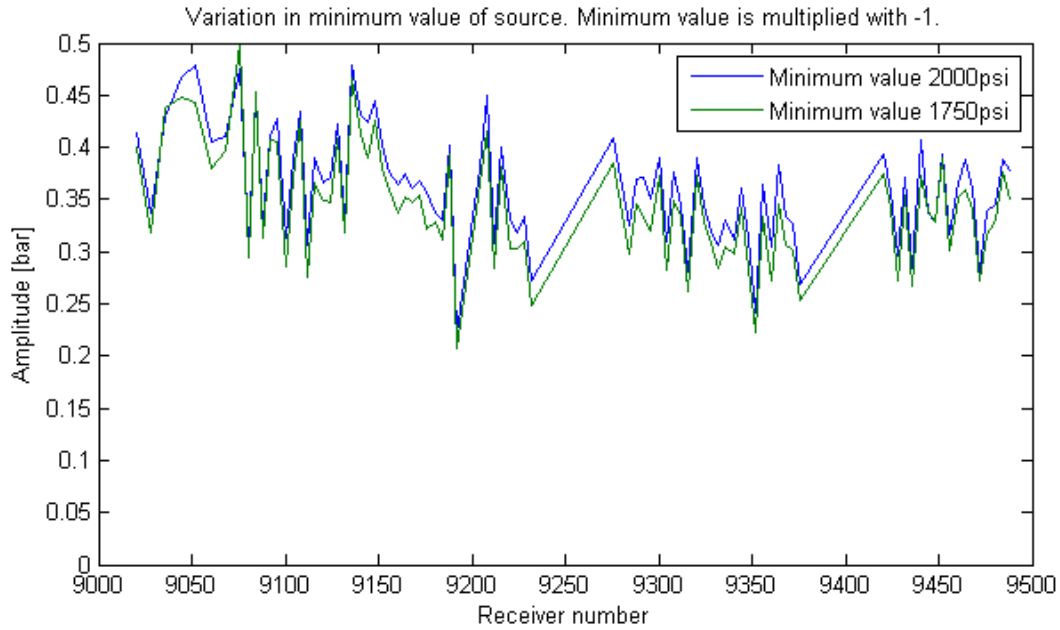
Figure 8.5: Recorded minimum amplitude for the given data-selection. Data has been made positive for convenience. Note the large in-phase variations.

psi. The result is shown in figure 8.6 and all amplitudes display the same variation with respect to receivers leading to strengthen the suspicion that the different receivers have substantially different response to a given pressure. Another less dramatical explanation for this result is near surface reflections altering the shape of the wavelet. Since the receivers are located on the ocean floor, variations in ultra-shallow reflections could alter the response of the receivers. Another possible explanation could be that the receivers have different sensitivity and that there exist a normalization factor for each receiver that is being used in production processing of this data.

Figure 8.7 shows how all the studied parameters changes with a change in pressure. A value of 90% should indicates that the low pressure survey has an amplitude that is 90% of the original pressure or an amplitude drop of 10%.

As figure 8.7 shows the biggest amplitude difference is detected in the direct arrival. The source ghost shows on average a 1% lower amplitude difference and seems to in general follow the same trends as the difference in direct arrival. It is also observable that there are some pretty large variations in the source strength difference. Ranging form bellow zero to above 10%. It is clear from these analysis that the difference in the two sources are varying quite a bit. However when the data is run through the stacking process the change in source variation is smoothed out due to the fact that a stacked trace consists of energy from different shots. An approximation of this effect is found by smoothing figure 8.7 with a 15pt boxcar filter. The resulting figure 8.8 shows a source difference variations

32
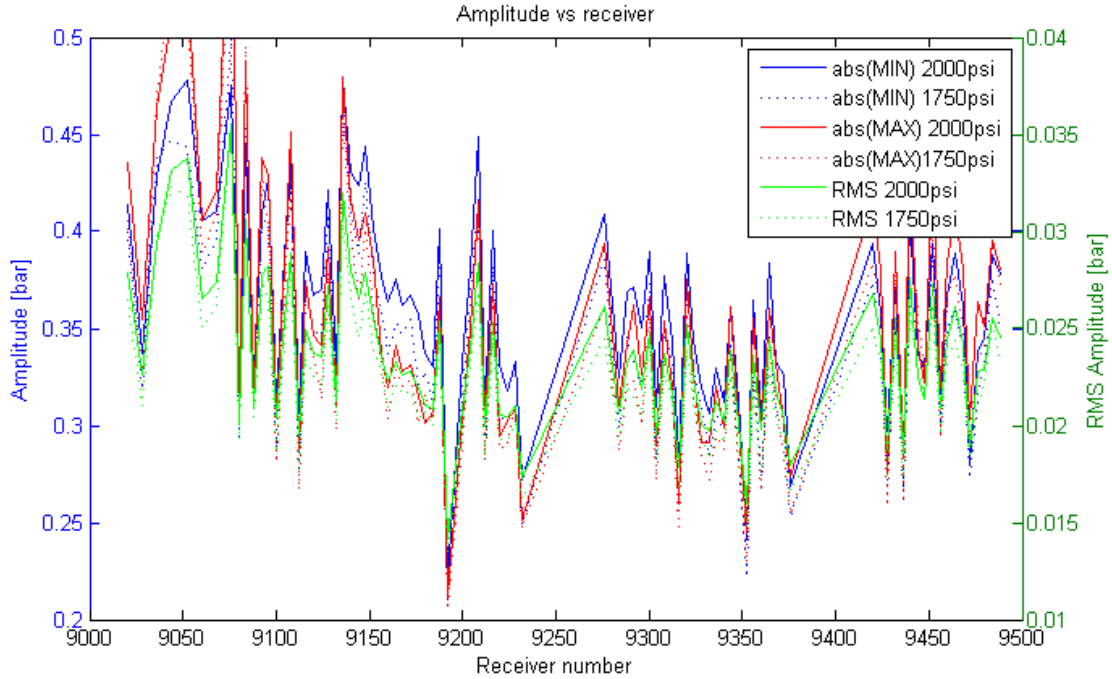
Figure 8.6: All analysed wavelet features for the given data-selection. Negative data has been made positive for convenience. Note how all wavelet features have a similar variation in both surveys. RMS value plotted on scaled axis but show same trend.

that might be observable in the stack.

Figure 8.8 shows the lines are more similar at the edges of the plot. By comparing this observation with a figure of the offset and difference in offset (figure 8.9) it seems like the difference in direct and source ghost amplitude is varying with offset. This indicates either a change in directivity between the surveys or a change in the ghost reflection surface i.e. sea surface. By assuming that the effect is purely a change in sea surface reflectivity a plot of ghost to direct arrival would represent the reflection coefficient of the sea surface. Figure 8.10 shows the apparent reflection coefficient plotted for each survey. There are several features here that is interesting. Firstly there is an clear offset effect resembling the absolute offset value (figure 8.9). Secondly the apparent reflection coefficient is greater than 1, indicating that this may have something to do with source directivity. The changes in apparent reflectivity from the 2000 psi survey to the 1750 psi survey could potentially be caused by a change in the sea surface. However this effect could also be result of changes in source directivity. By assuming a constant reflection coefficient from the sea surface and that the source behaves with plane symmetry, the changes in direct-ghost ratio could be related to the difference in the ray paths exit angle. Figure 8.11 shows how the difference in exit angle changes as a function of offset. This plot shows a difference in exit angle of 2.6 degrees at offset 25 meters.

33
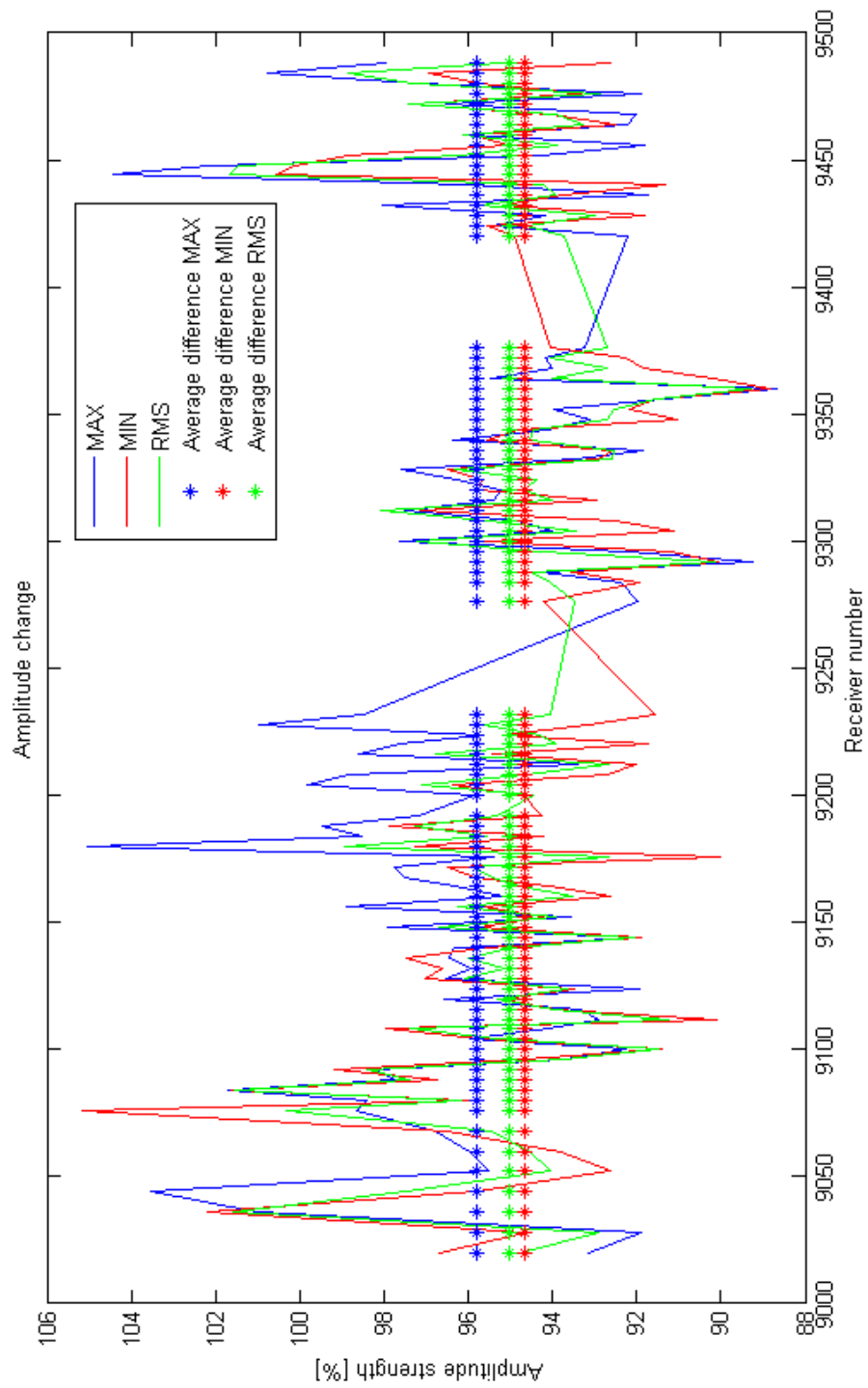
Figure 8.7: Shows the amplitude of the 1750 psi survey divided by the production pressure survey. Near-zero offset. Average values marked with stars. MAX average:95.8%, MIN average 94.6% and RMS average: 95.0%.
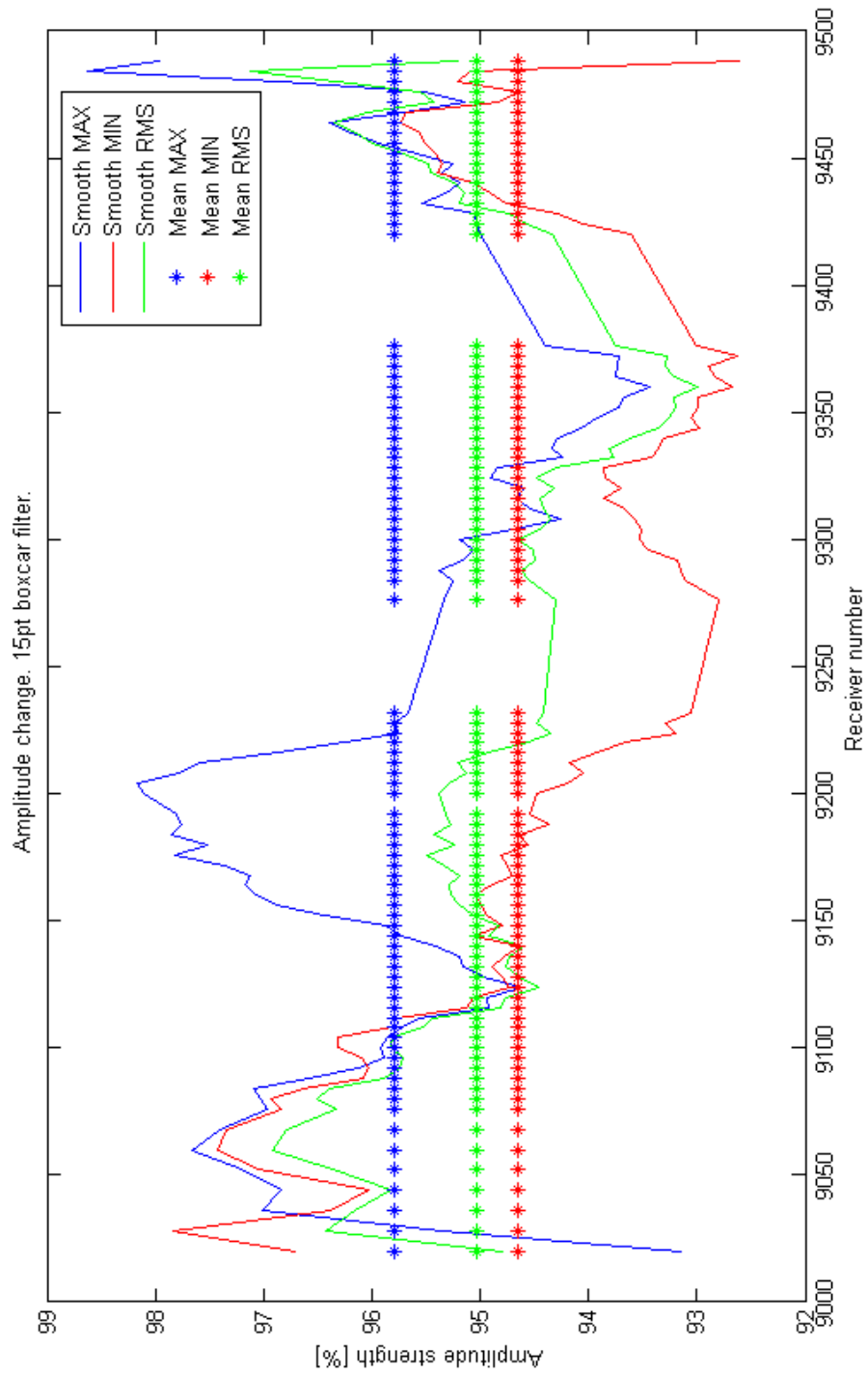
Figure 8.8: Shows the amplitude difference for near-zero offset direct arrivals relative to production pressure. Smoothed with a 15pt boxcar filter.
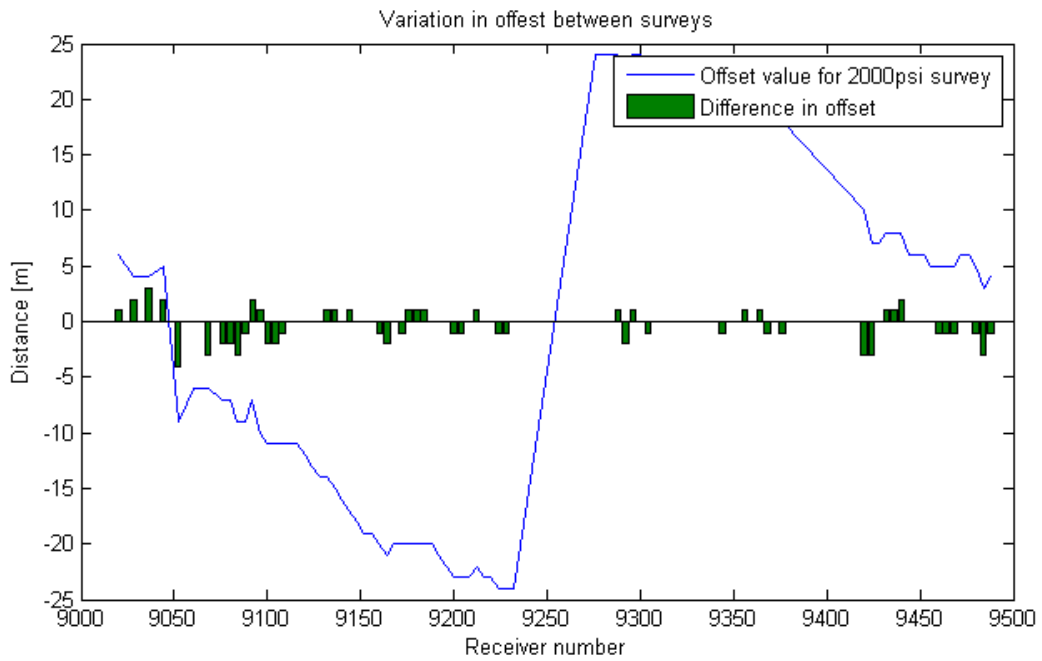
Figure 8.9: Blue line show how offset is varying with receiver number in the analysed data. Green columns show difference in shot positioning between the surveys.
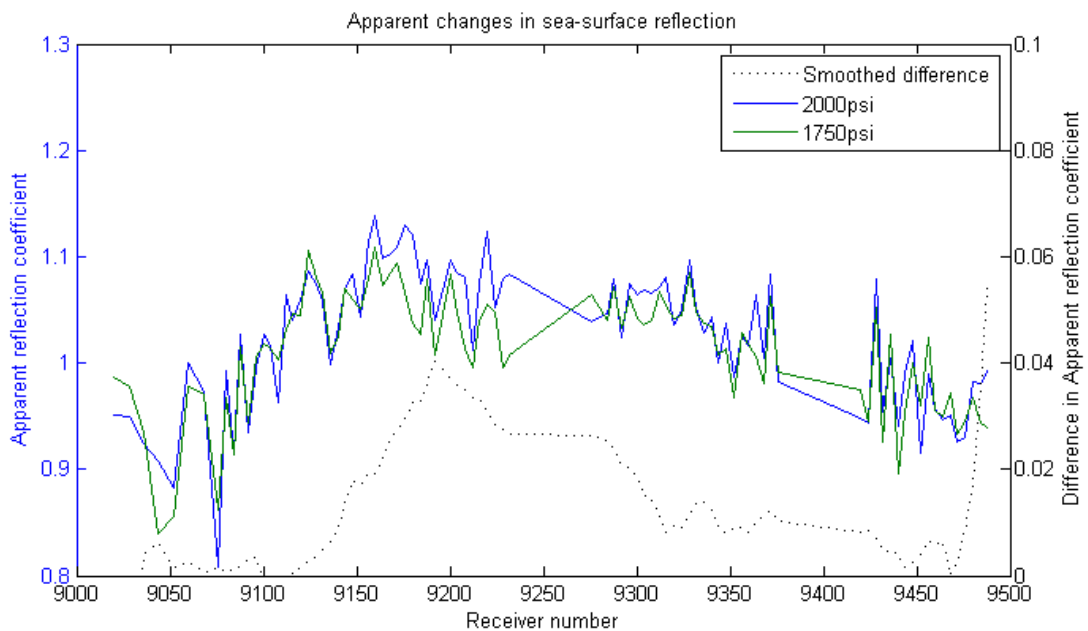
Figure 8.10: Figure showing the ghost to direct arrival ratio. Dashed black line represents a low pass filtered difference of the apparent reflection coefficient (plotted on right y-axis).
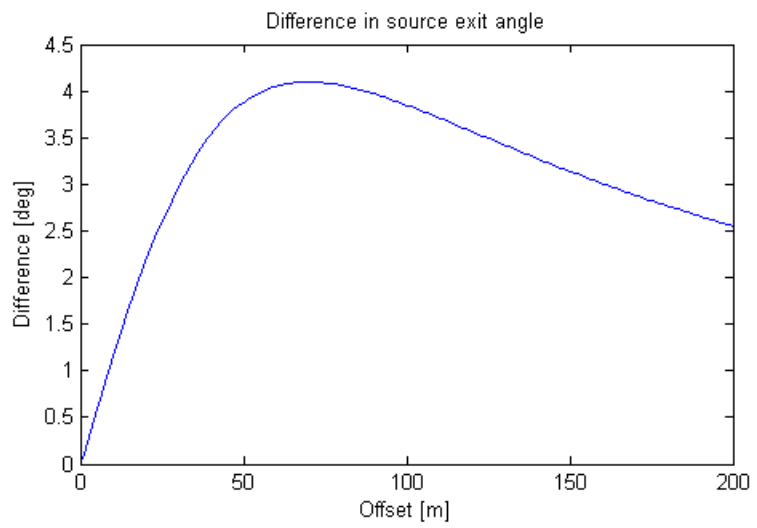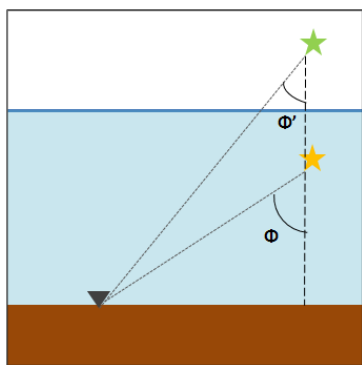
Figure 8.11: Left: is the exit angle for direct and ghost signal. Right: Plot showing how the difference in exit angel peaks at 70 meter offset.

8.2.2 Optimum scaling factor estimation

This analysis is also an attempt on characterize the changes in amplitude caused by change in source-array pressure. The approach is different from the approach in section 8.2.1. As a basis for this chapter the following relation is investigated.

$$S_1\alpha + n_1 \approx S_2 + n_2 \tag{30}$$

Where S2 is equal the full pressure signal S1 scaled by a factor alpha. Which means that if there is no noise the S2 and the correctly scaled S1 should be equal. However since this is real data there is bound to be some noise and the two surveys can not be made equal by mere scaling. Even so, by varying the scaling parameter alpha, the minimum difference would indicate the correct scaling factor.

The signal analysed was extracted from comparable shots from each survey (figure 8.12), where the shots had similar firing position (see section 8.3.2 for more on variation in shot positioning). In order to minimize the impact of the noise on the calculations all amplitudes bellow 25 µbar is zeroed out and only the first 2000ms of the signal is analysed. This operation increases the total signal to noise ratio of the shot gather and should increase the accuracy of the amplitude difference estimation. As shown in figure 8.13, the most suited scaling factor for shot number 150 is 93%.

If this analysis is done for every matching shot pair, the average value would give a good estimate of the real amplitude variation. Figure 8.14 shows the minimum in difference as a function of shot-pair number. Due to large offsets of the first 90 shots they are not a part of this source variation estimation. The rest of the shots show an average value of 89.9% which are consistent with the estimate of 91.5% in equation 29.

Since this process evaluate the surveys on a sample-by-sample basis it is rather sensitive to changes in positioning and signal character (e.g. change in bubble signature). Another, more robust approach would be to restrict the analysis to zero offset direct arrivals. These signals would be the rawest and most unaltered part of the seismic and therefore perfect for amplitude variation analysis.

The shots picked for this analysis are chosen on a minimum offset basis (same as in section 3.1). In addition, shots with greater mismatch in positioning than 5 meters are excluded. For further accuracy the signature peaks has been forced aligned at 60 ms. To counter the change in bubble time period the signal is zeroed out after the first wavelet has arrived. Figure 8.15 shows a wavelet-pair from this analysis.
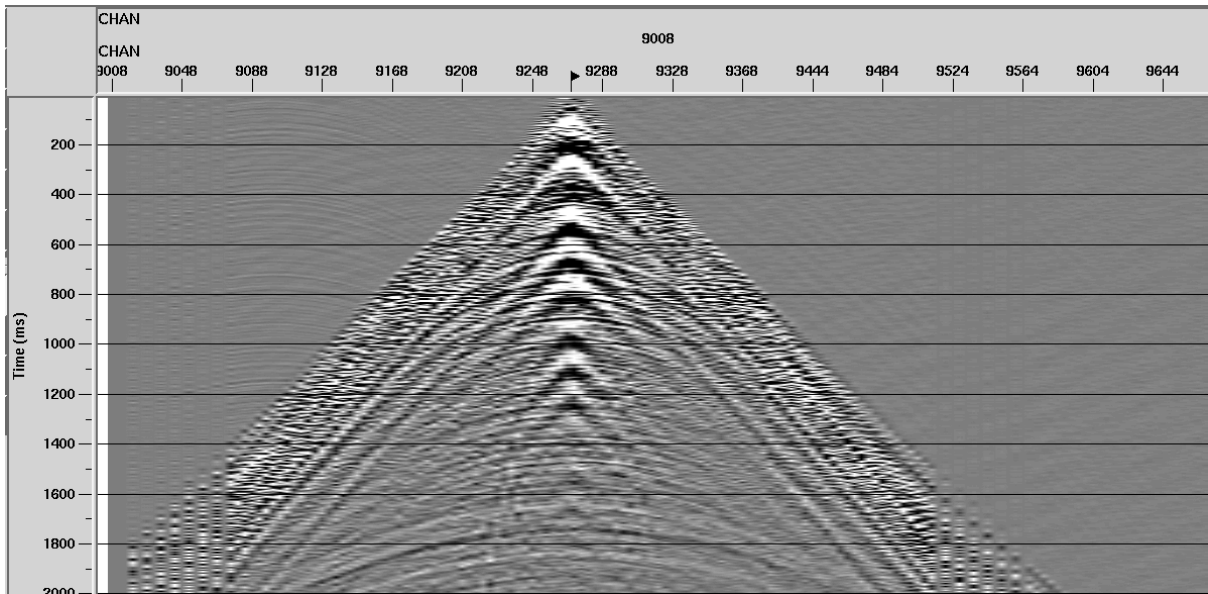
Figure 8.12: Shows the data used in the first amplitude variation analysis.
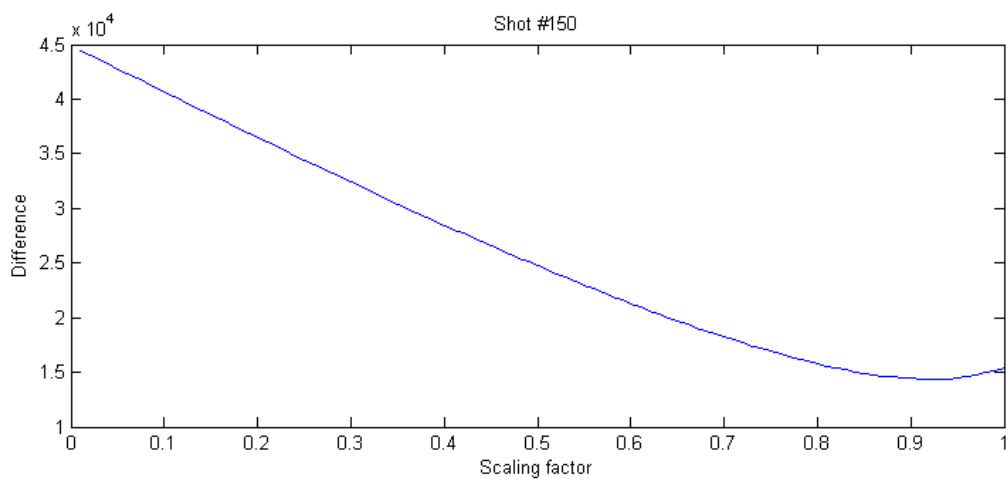
Figure 8.13: Shows difference between scaled S1 and S2 as a function of scaling factor for shot number 150. Minimum in 0.93.
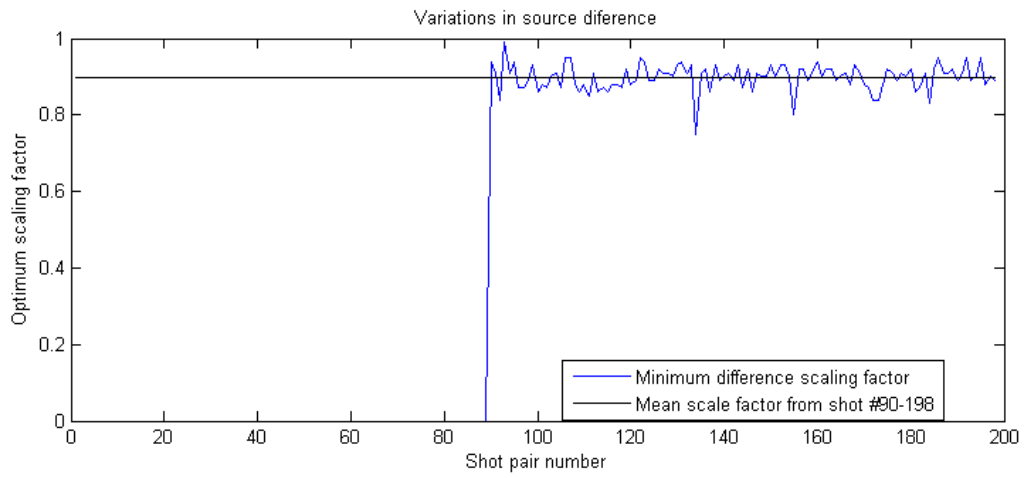
Figure 8.14: Plot shows the scaling values that minimize shot difference.
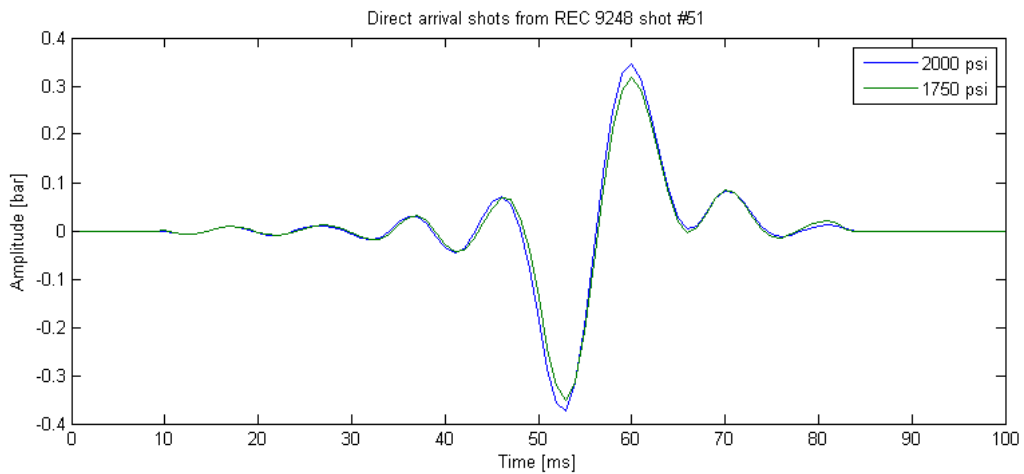
Figure 8.15: Shows a corresponding pair of analysed direct arrivals.
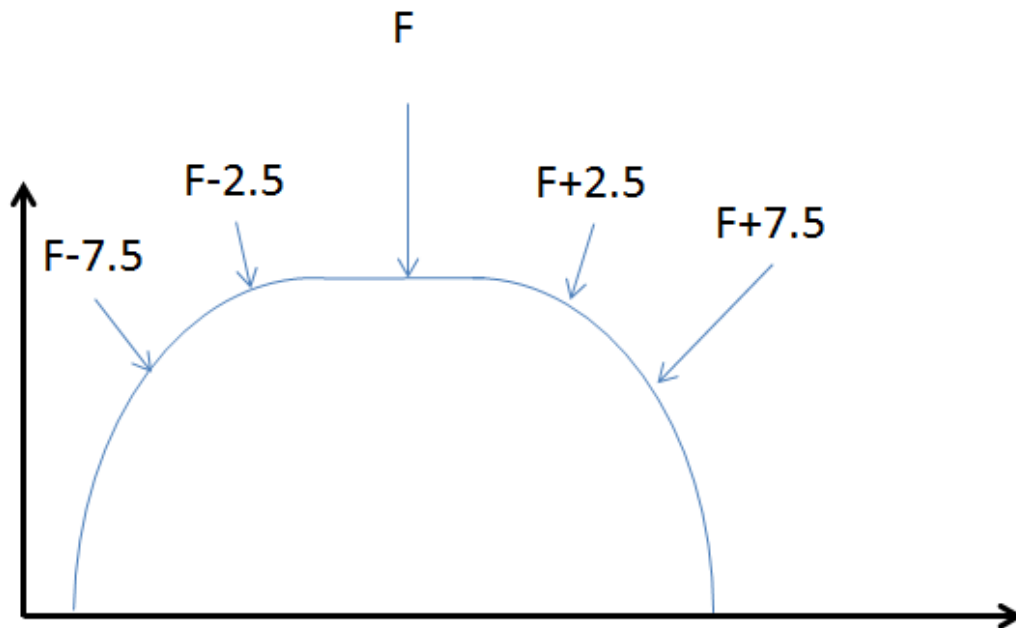
Figure 8.16: Graphically shows the deign of the sliding bandpass filter.

After this data had been run trough the same analysis as the shot gathers mentioned above the average scaling factor is found to be 94.1%, which indicates a deviation from the theoretical estimate of 30%. Due to the fact that this second analysis has a more restricted selection of data it is believed to be the most accurate.

In order to further increase the understanding of the signal variation made by the different firing pressure, it would be beneficial to investigate how the signal variation act as a function of frequency. By applying a band-pass filter to the signal before running it through the process described above, an estimate of the change in signal as a function of frequency can be derived.

A sliding bandpass filter was used defined as shown in figure 8.16 and an impulse response at f=17.5 is shown in figure 8.17.

Figure 8.18 show the result of the frequency analysis described above using both the whole stack and the direct shot arrival data. This analysis indicates how the change in firing pressure alters the signal as a function of frequency. A value of 95% for frequencies of 20 Hz would indicate that a reduction in firing pressure from 2000 psi to 1750 psi would reduce the 20 Hz portion of the signal by 5%. Therefore a value close to one in the
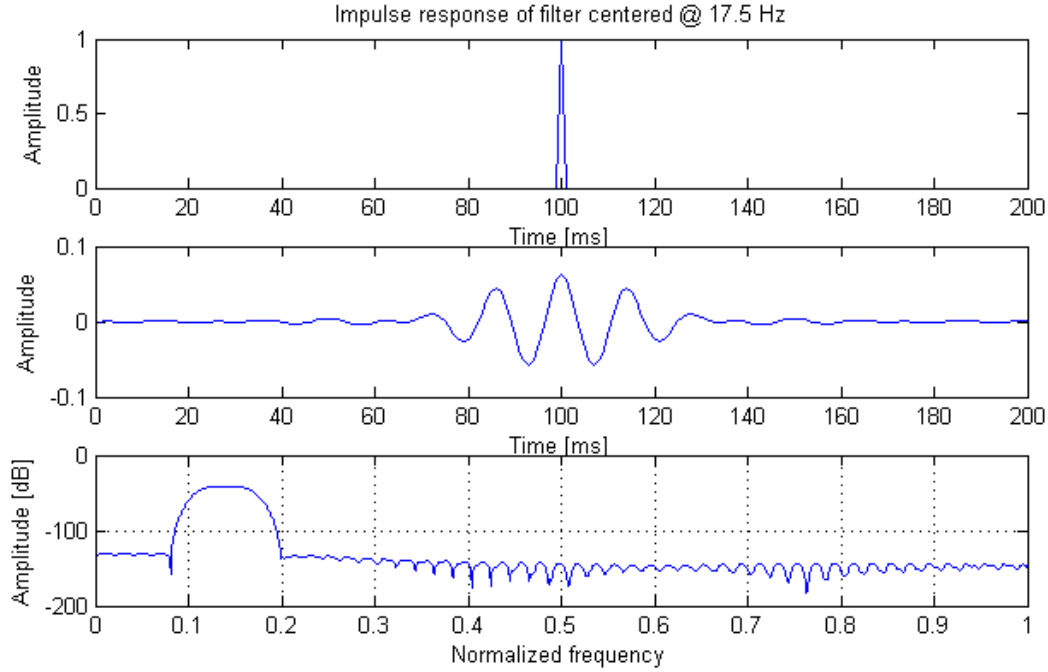
Figure 8.17: Impulse response for the bandpass filter centred around 17.5 Hz. $F_{nyq} = 125$Hz.

graph represents a high similarity between the signals and a low change in this frequency range. A great deviation from one would indicate the opposite.

Since this analysis effectively is an attempt of quantify the amplitude change in frequency one would expect to observe the same trends by a simple comparison of frequency spectrum. Figure 8.19 shows the spectrum of the whole shot data. A shift in the oscillations is observable in the frequency domain. This is most likely due to the change in the bubble time period. By smoothing the spectrums, the effect of change of the bubble is damped and the amplitude change is more evident (figure 8.20).

Since the data containing the direct arrival contain minimal bubble energy, the spectrum of the direct arrival contains less oscillations and is therefore not smoothed before it is analysed (figure 8.21).

By simply dividing the 1750 psi spectrum on the 2000 psi spectrum it should yield another estimate of the source variation as a function of frequency. The result is shown in figure 8.22.

It is easily observable that both figure 8.18 and figure 8.22 display the same trend and similar values. However the two portions of data seem to show the same inconsistency. The direct arrival analysis shows that the main change in amplitude is located in the 25-65 Hz range. On the other hand, the full shot gather analysis indicate an amplitude
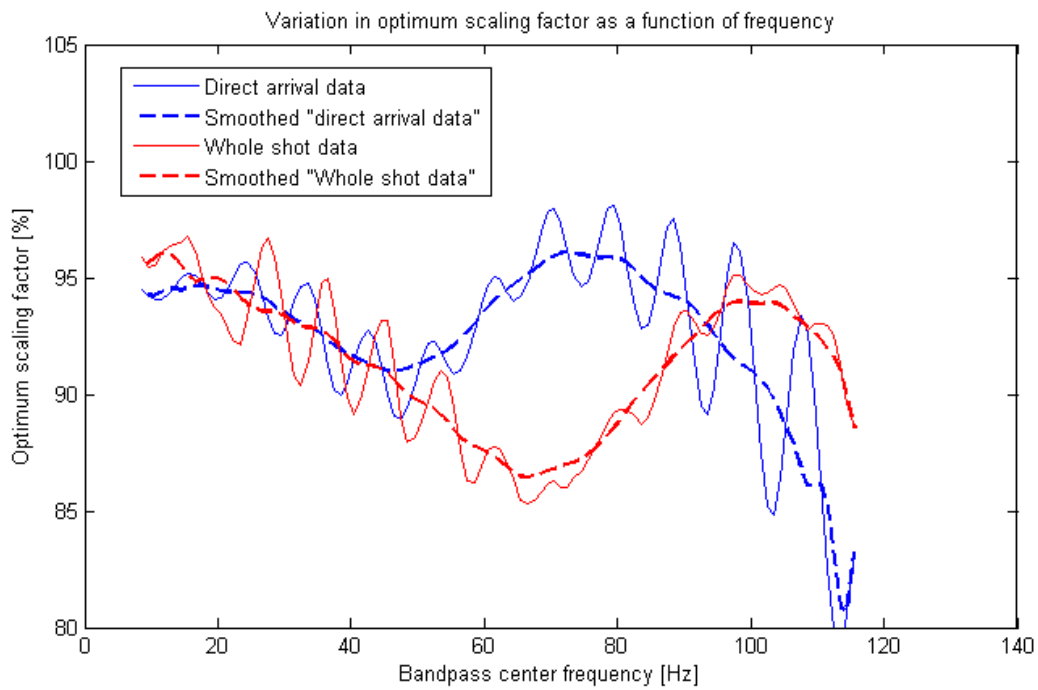
Figure 8.18: Variation in optimum scaling factor as a function of frequency. Shows how the two data selections respond to the analysis.
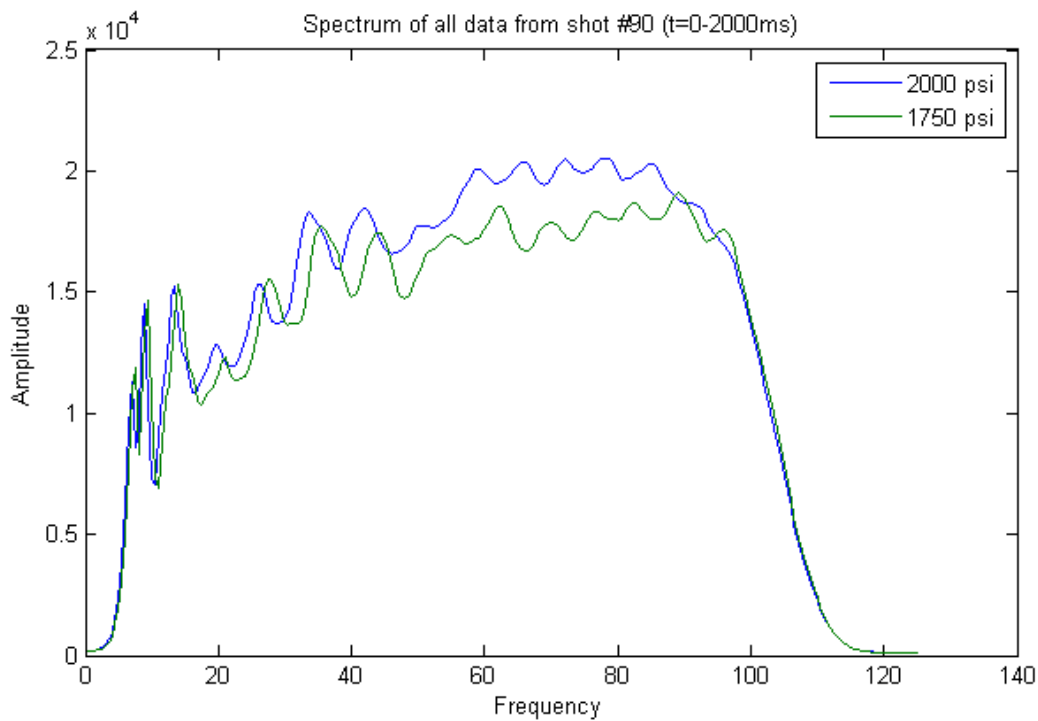
Figure 8.19: Spectrum derived from data from all receivers, all shots and from t=0-2000 ms.
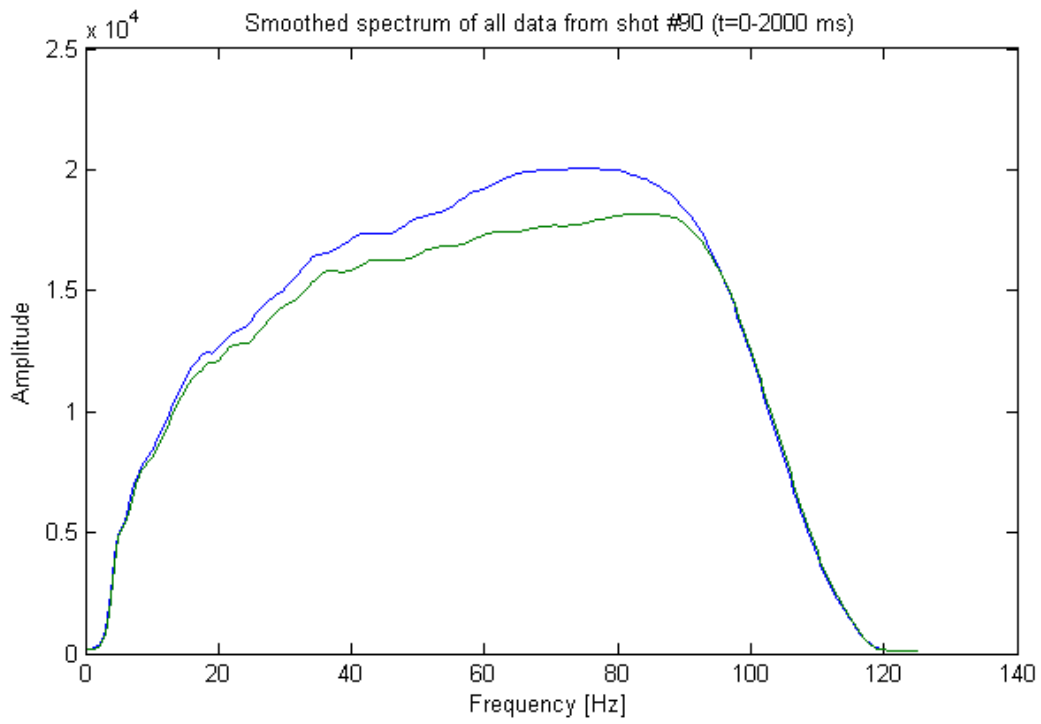
Figure 8.20: Smoothed version of figure 8.19
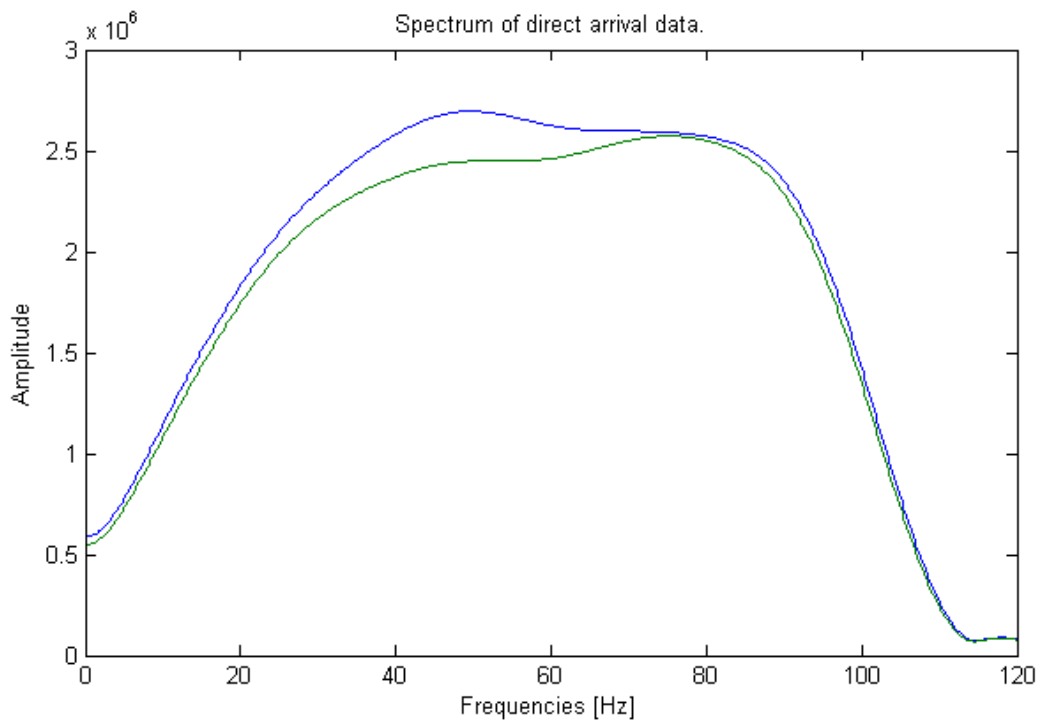
Figure 8.21: Spectrum derived from direct arrivals.

44
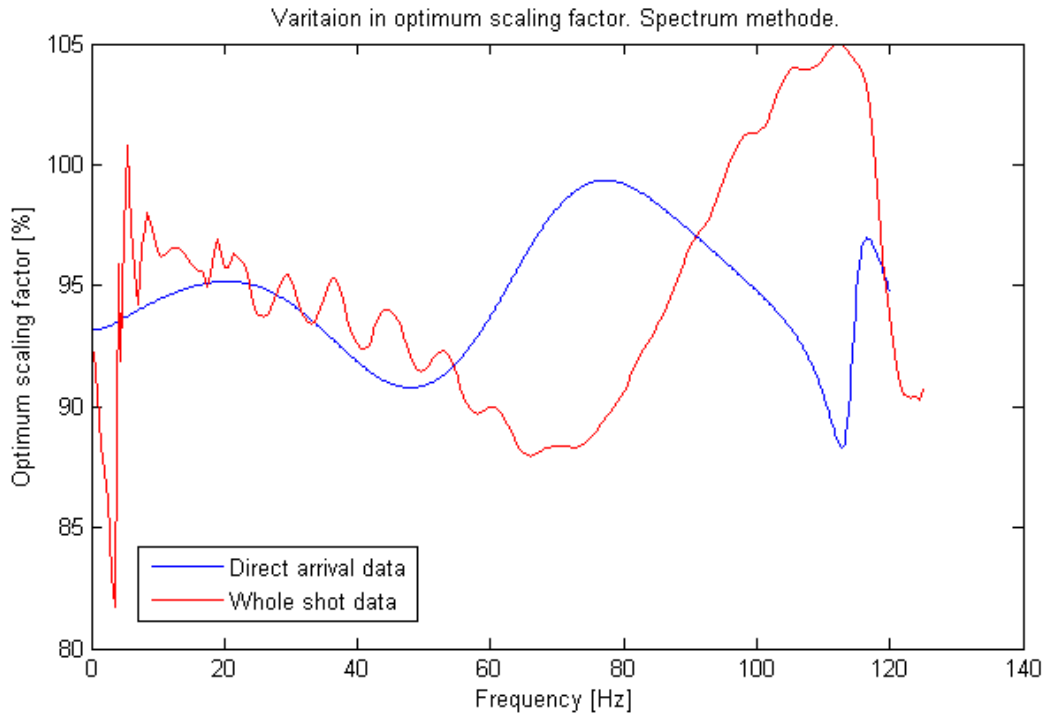
Figure 8.22: Variation in optimum scaling factor. Derived by spectral division. Noticee the similarities with figure 8.18.

effect on all frequencies from 30-90 Hz. This difference has to be understood in order to conclude this source variation analysis.

To better understand why the two sets of data seemingly show different response to source variation it is essential to find out in what way the data are different. The most obvious difference is that the direct arrival contains close to zero offset data while the shot gather contains offsets up to 3000 m. Both difference in how the primary relates to the first multiple (as discussed in section 5), the presence of refracted waves and source directivity changes are effects that could have induced this differences.

By sorting the direct arrivals on offset the signal can be more systematically analysed. Figure 8.23 and 8.24 show FX plot of traces sorted on offsets from 0-100 meters. They both show similarities with figure 5.6 and an averaging of spectrums from different offset arrivals would therefore be considered undesirable. These FX-plots was used to divide the data in to 4 different offset-groups based on their spectrum characteristics as shown in table 2. Group 4 is believed to contain mainly refracted energy as a crude estimate of total reflection from the seabed is around 50 deg.

Spectrums are then derived based on averaging the spectrums in each group for each survey. The resulting spectrums are shown in figure 8.25. The group 1 data displays

Table 2: Offset groups with incidence angle.

Group	Offset [m]	Incidence angle [deg]
1	0-10	0-9
2	11-42	10-33
3	43-70	34-50
4	70-100	50-60
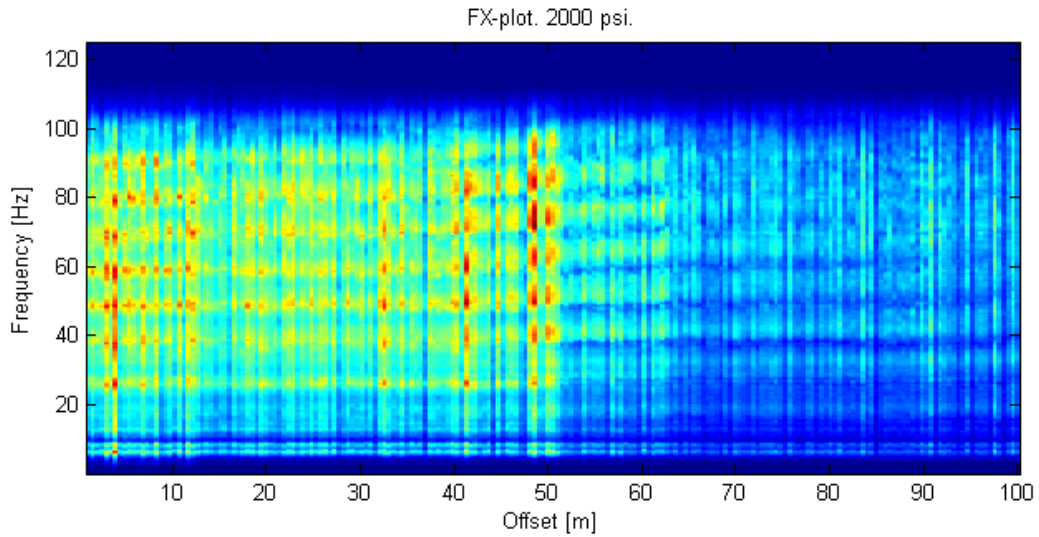
Figure 8.23: FX plot of the direct arrivals for 2000 psi survey. Note the similarities with figure 5.4.
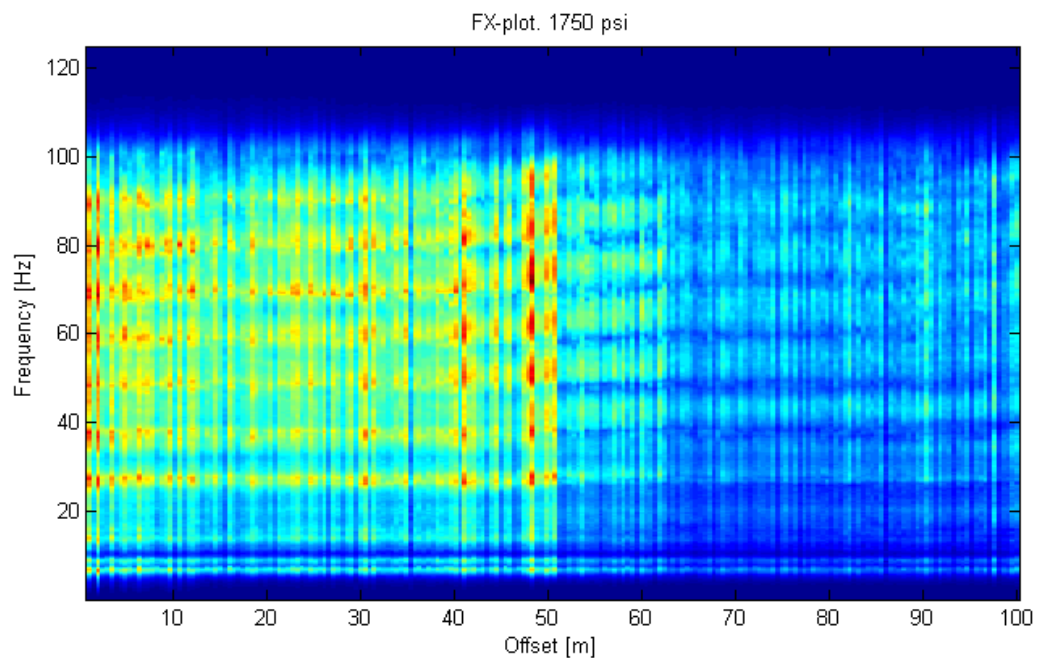
Figure 8.24: FX plot of the direct arrivals for 1750 psi survey. Note the similarities with figure 5.4.

the same trend as observed for near offset data while group 4 data show similar trend as using the whole shot gather. In figure 8.26 displays the same data as in 8.25 with muting of arrivals after the source ghost to counter the oscillations in the spectrum. These data are then again used to derive a scaling factor frequency variation plot in figure 8.27. Also notice here how the scaling curves display similar trends as in figure 8.18 and 8.22.

Keeping in mind the the results of the apparent reflectivity analysis in figure 8.10, the dataset used to derive figure 8.26 are divided into two parts divided by the zero-crossing between the primary and the ghost signal. Figure 8.28 show how an arbitrary shot is divided. Since most wavelets don't have a sample at the zero crossing the closest sample is forced equal zero. The dataset has been re-sampled to 1 ms and this helps in making the alteration less (compared to a 4 ms sampling interval). Figure 8.29 show a close-up of the zero crossing before and after the separation. With this in mind the frequency comparison of the direct and ghost signal could be analysed. The frequency spectrum of the two different signals are shown in figure 8.30 and 8.31.
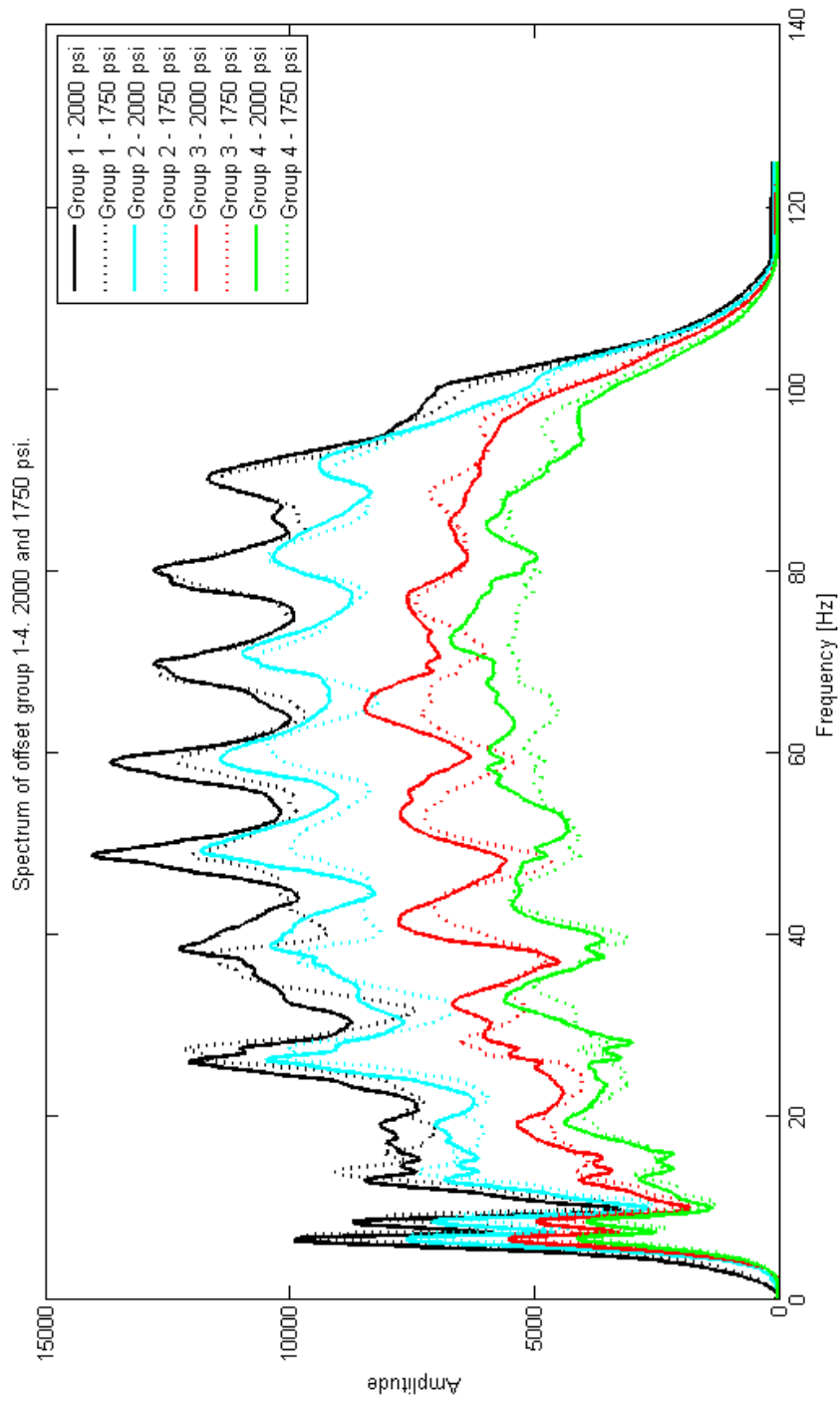
Figure 8.25: Difference in spectrum for the 4 groups described by table 2.
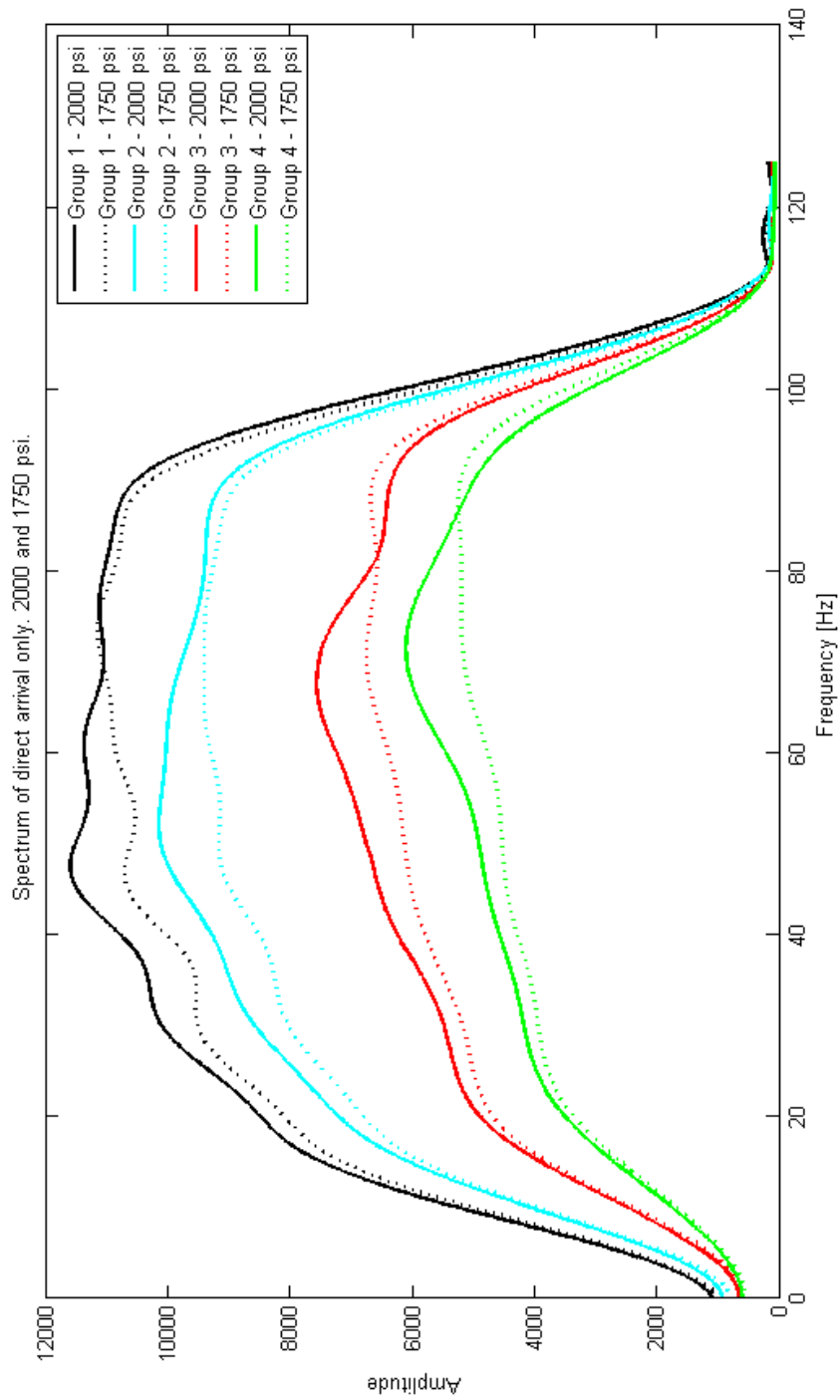
Figure 8.26: Difference in spectrum for the 4 groups described by table 2. Without bubble signal.
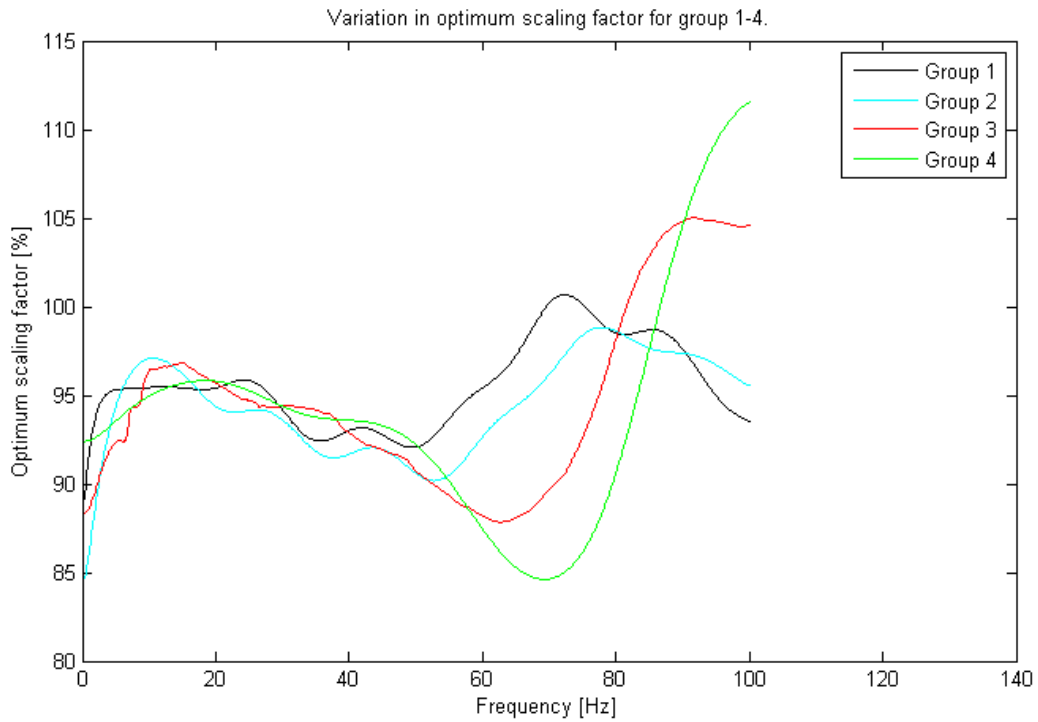
Figure 8.27: Optimum scaling factor as a function of frequency for the four offset groups described by table 2.
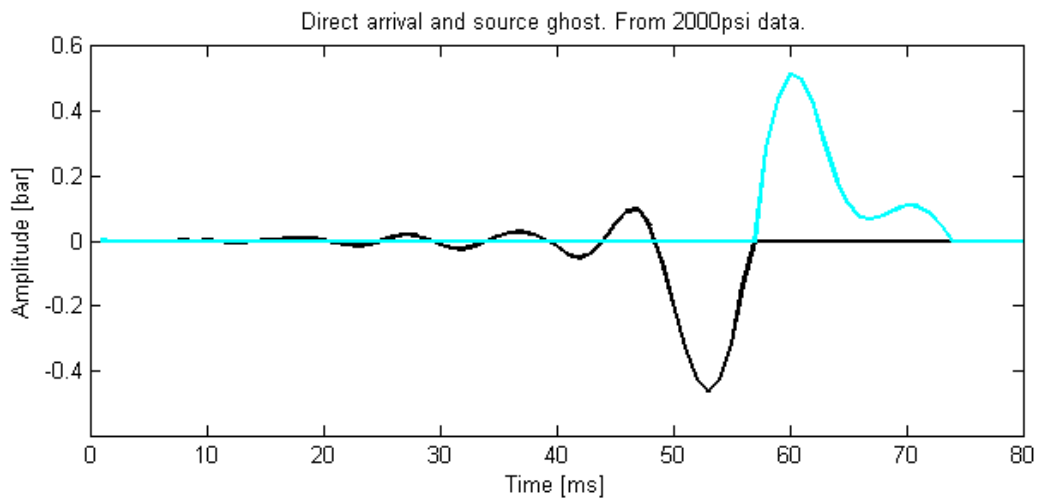
Figure 8.28: Arbitrary signal split into direct (black) and ghost (cyan) lines.
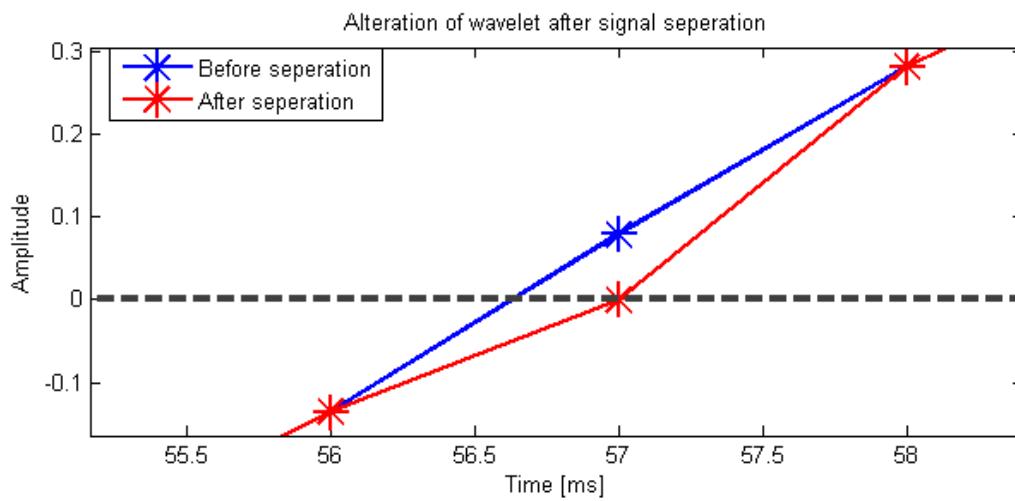
Figure 8.29: Close up of alteration due to signal separation.
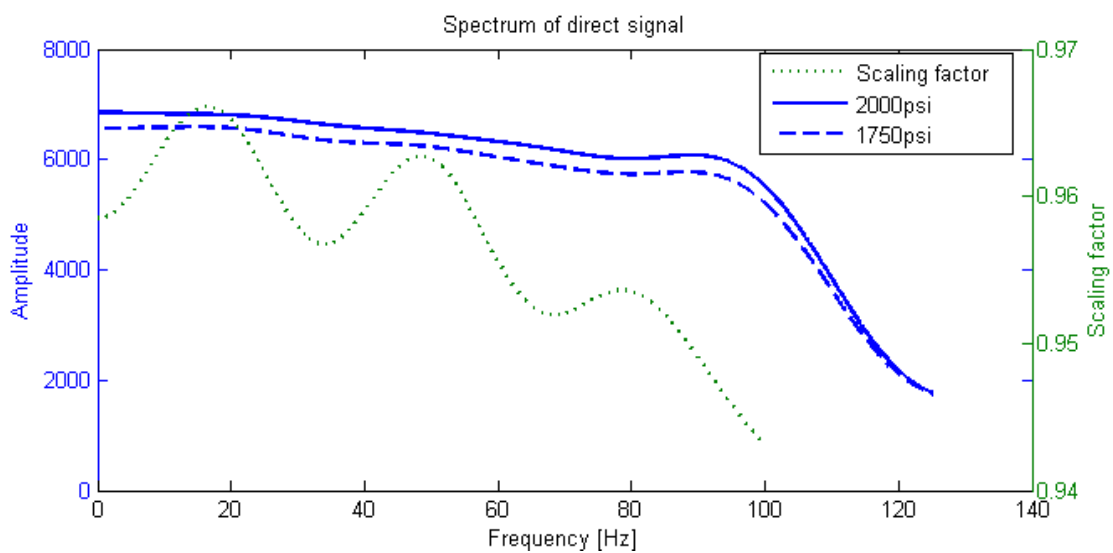
Figure 8.30: Blue line show spectrum of direct signal for both surveys. Green dotted line show derived scaling factors. Average scaling factor from 0-100Hz 95.7%.
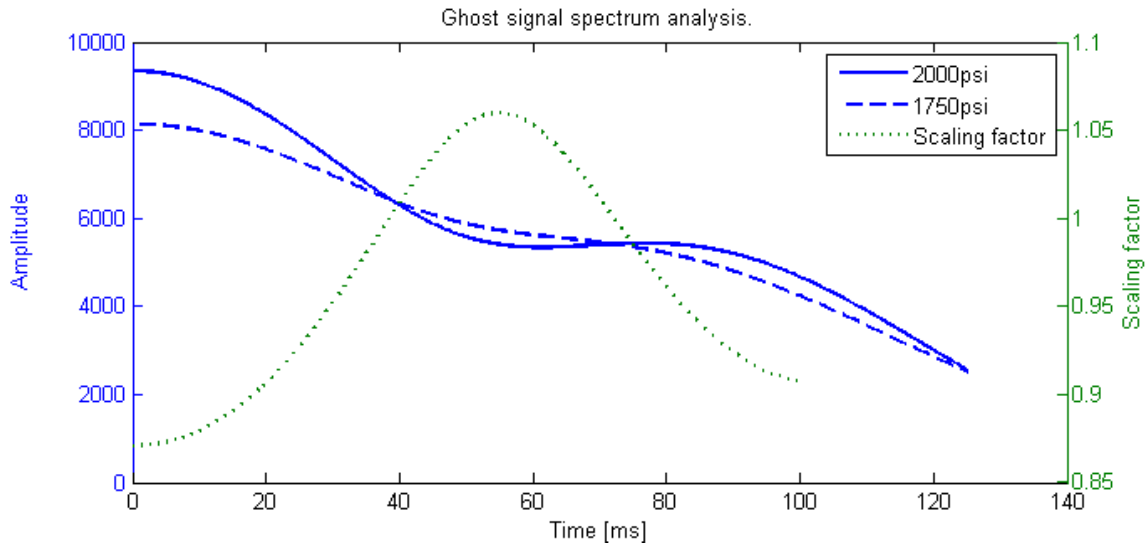
Figure 8.31: Blue line show spectrum of ghost signal for both surveys. Green dotted line show derived scaling factors. Average scaling factor from 0-100Hz 96.37%.

8.2.3 Single shot analysis

To be sure that the effect observed for zero offset data is not an artefact from the averaging process, a comparison of two and two comparable signals shot from same position and recorded at the same hydrophone was conducted. It was found 12 shots with offset less than 10 meters and a difference in shot positioning less than 4 meter. The 12 pairs was also recorded at the same recorder. The spectrum from these analysis are varying a bit when looking at one shot at a time (figure 8.32-8.35). However, the trend shown in both previous near stack analysis seems to be the predominant trend.
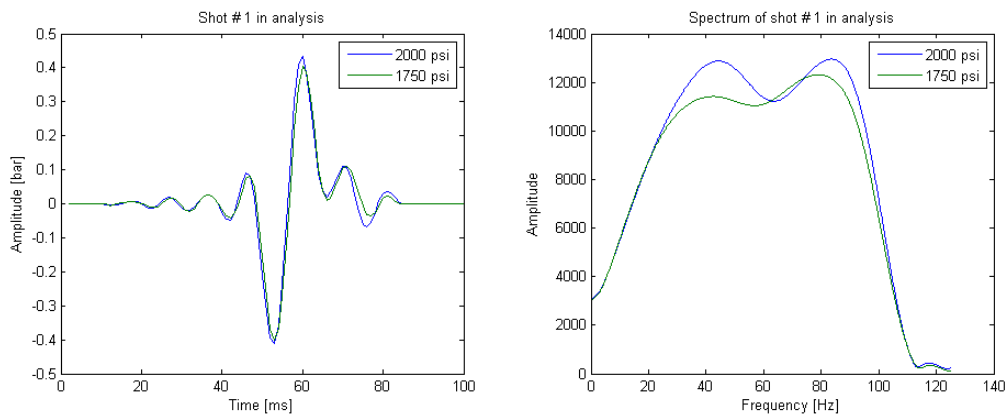
Figure 8.32: Amplitude and spectrum comparison of shot 1.
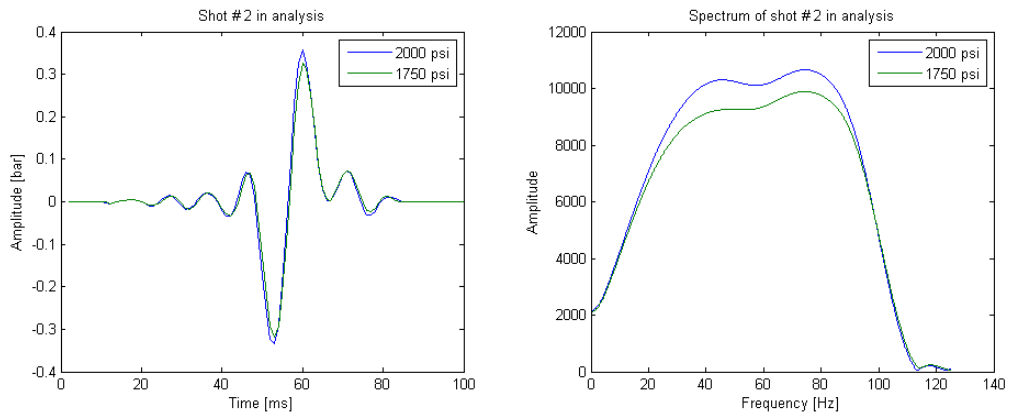
Figure 8.33: Amplitude and spectrum comparison of shot 2.
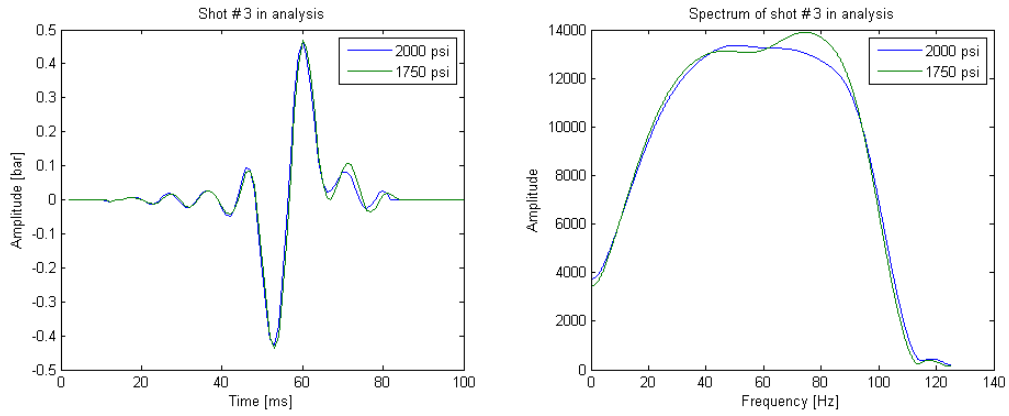
Figure 8.34: Amplitude and spectrum comparison of shot 3.
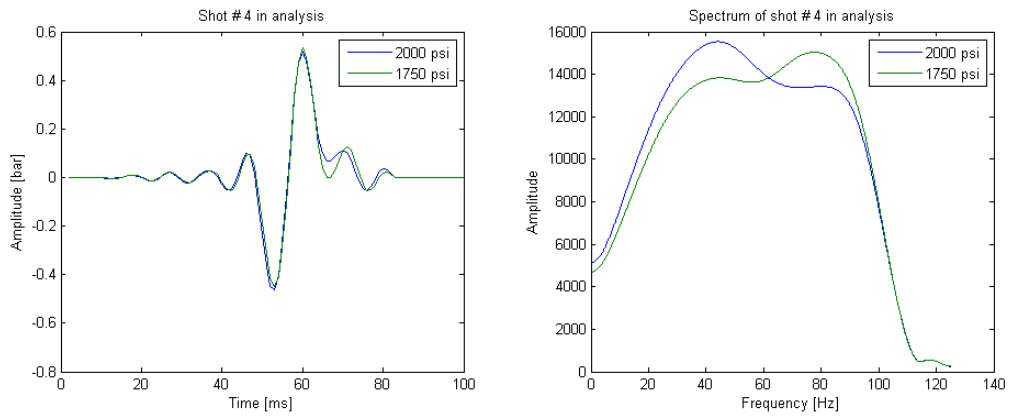
Figure 8.35: Amplitude and spectrum comparison of shot 4.
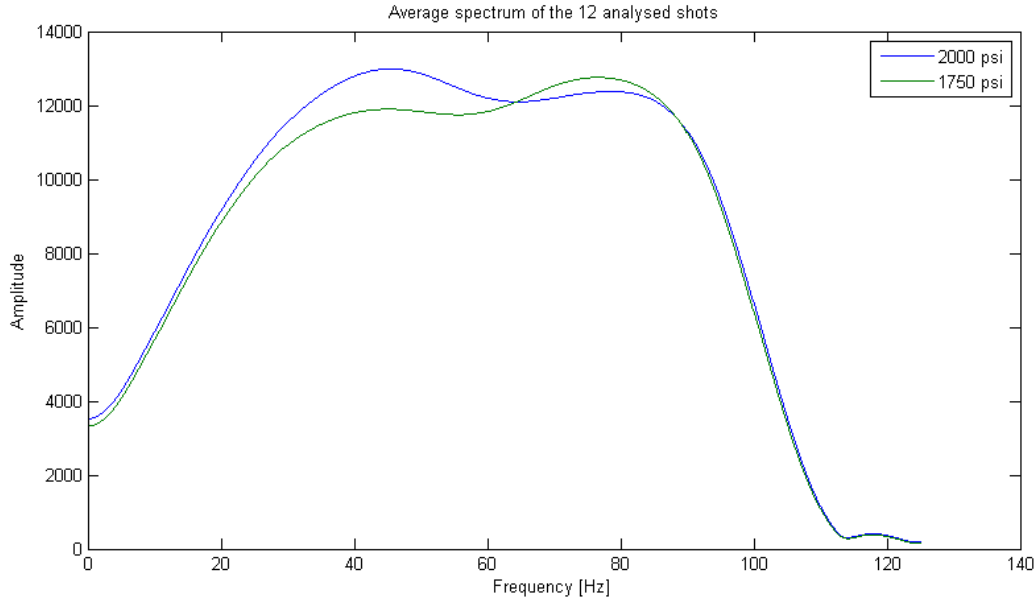
Figure 8.36: Average spectrum comparison from the 12 most comparable shots in the survey.

8.2.4 Synthetic analysis

The subject on how the spectrum change as a function of firing pressure is a poorly studied subject and it is therefore difficult to find literature that refer to it. By using the Marine Source Modeling package in the program Nucleus it is possible to simulate the experiment in order to find the expected response of increasing the firing pressure. The array (described in section 7.1) is used as a basis for the simulated air gun. The output of the simulation is shown in figure 8.37.

To counter the change in bubble time period the signal is zeroed out after time=25 ms. The resulting spectrums can be observed in figure
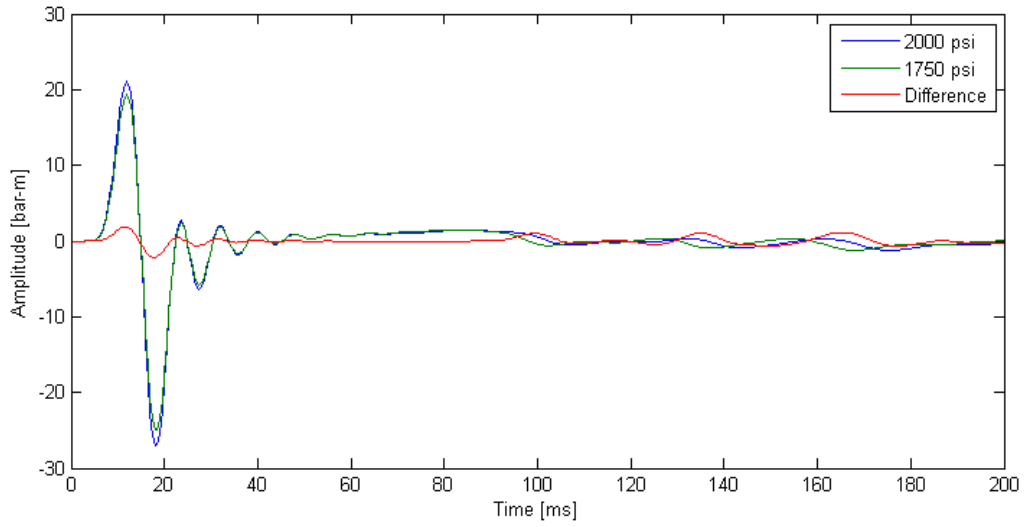
Figure 8.37: The output after running the source array simulation in nucleus. Red line shows the difference in the two firing pressures. Difference due to change in bubble pulse is similar size as change in primary wavelet.
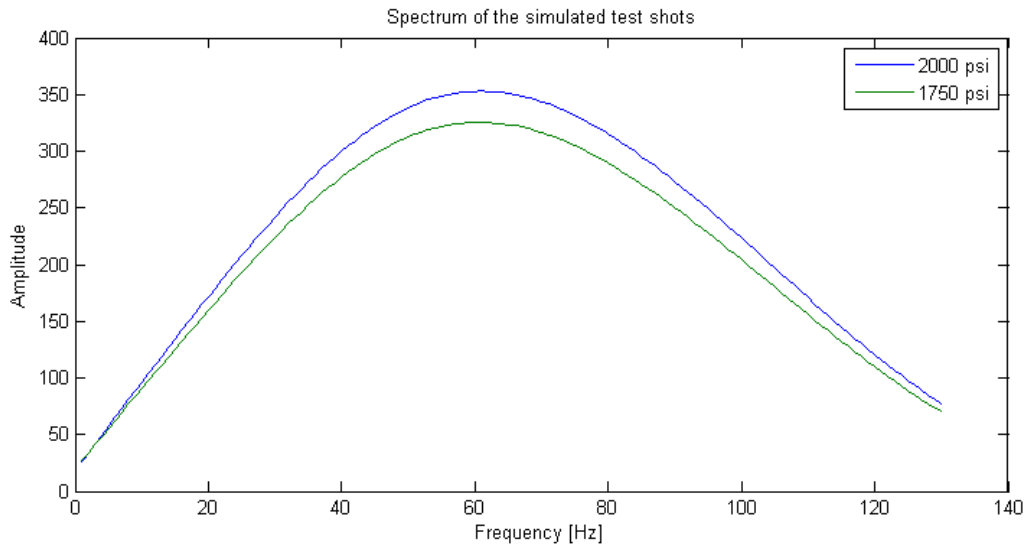
Figure 8.38: Spectrum of the simulated wavelet. Signal is put to zero after 25 ms in order for the analysis to disregard changes in bubble signature.
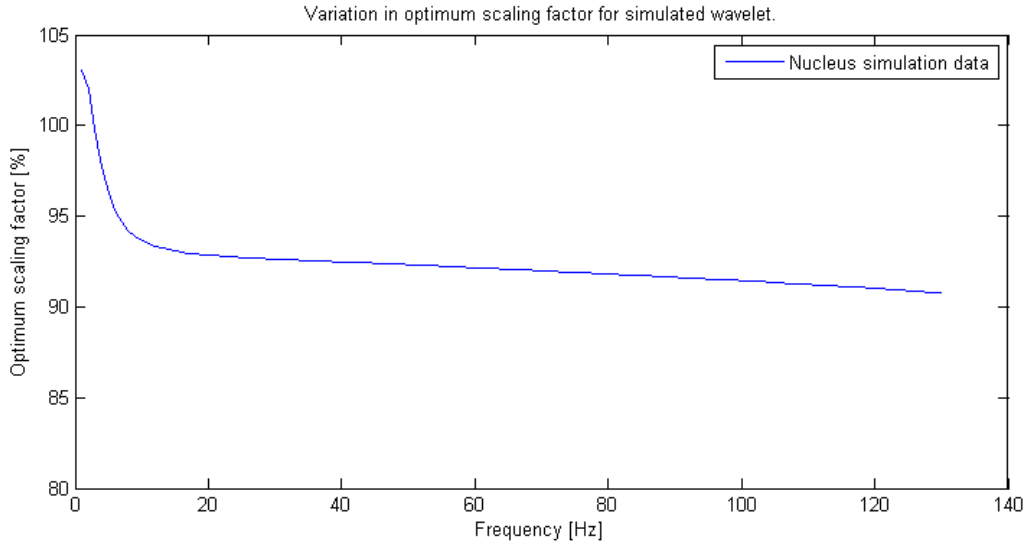
Figure 8.39: Analyses of the simulated array signals. Variation in optimum scaling factor as a function of frequency. Disregarding the edge effects the optimum scaling factor seems pretty stable over the frequency range 20-100 Hz. Mean value from 20-100Hz is 92.15%.

8.3 Noise evaluation

8.3.1 Background noise

In order to gain knowledge of the 4D potential it is important to establish the base background noise. This is done by taking the RMS of all the receivers at Valhall and derive the RMS amplitude from the first 400 ms. As seen on figure 7.3 the first shot is taken more than a kilometre from the nearest receiver making the first 400 ms contain only background noise. Figure 8.40 and 8.41 shows the result of this analysis for each receiver in the LoFS system for both surveys. The high noise area is the location of the Valhall platform and it is observed that the noise decreases radially from the platform in both surveys. The test line is located farthest away from the platform and is the line least contaminated with rig-noise with an average RMS value of 15.62 µbar for the production survey and 8.84 µbar for the test line. This shows that the production pressure survey contain about twice as much noise as the test line. Since the noise difference seems to be in the same order for the whole field it is believed that the increased noise is related to the activities at the platform. By extracting the noise frequency spectrum for the two surveys a better understanding of the difference could be achieved. The noise spectrum in figure 8.42 shows how the background noise seems to be substantially higher in the production pressure dataset for frequencies 20-100 Hz. By concentrating this analysis on the line of interest the spectral difference is decreased and limited to the area 20-60 Hz.
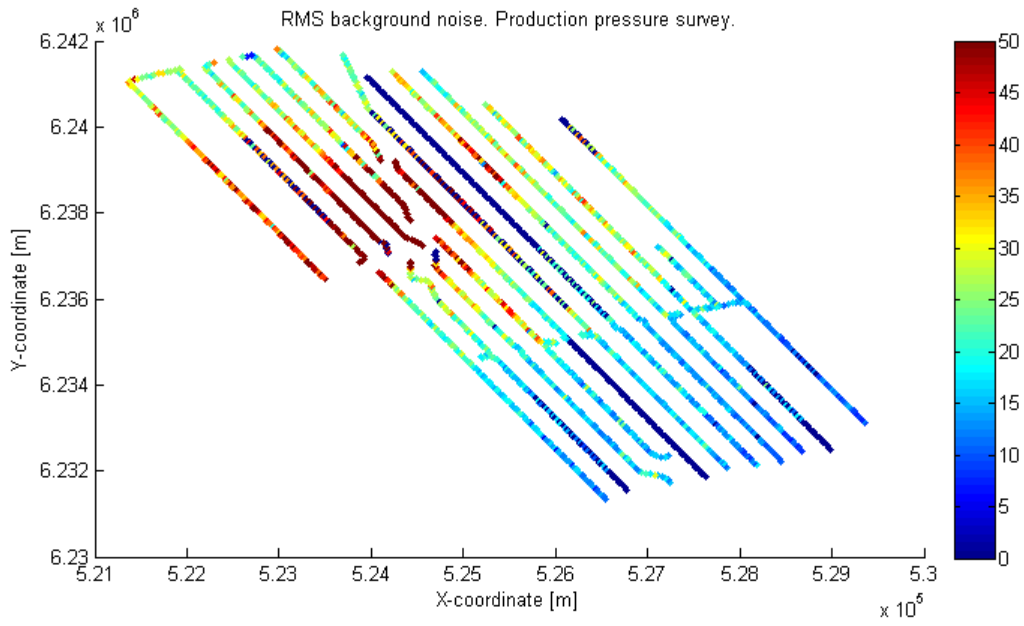
Figure 8.40: Displays the RMS background noise for the Valhall field. Color bar values are in µbar.

Even though there seems to be some inconsistency in the background noise level, a background level of 15 µbar is considered fairly small and should not corrupt the data to an extensive degree.
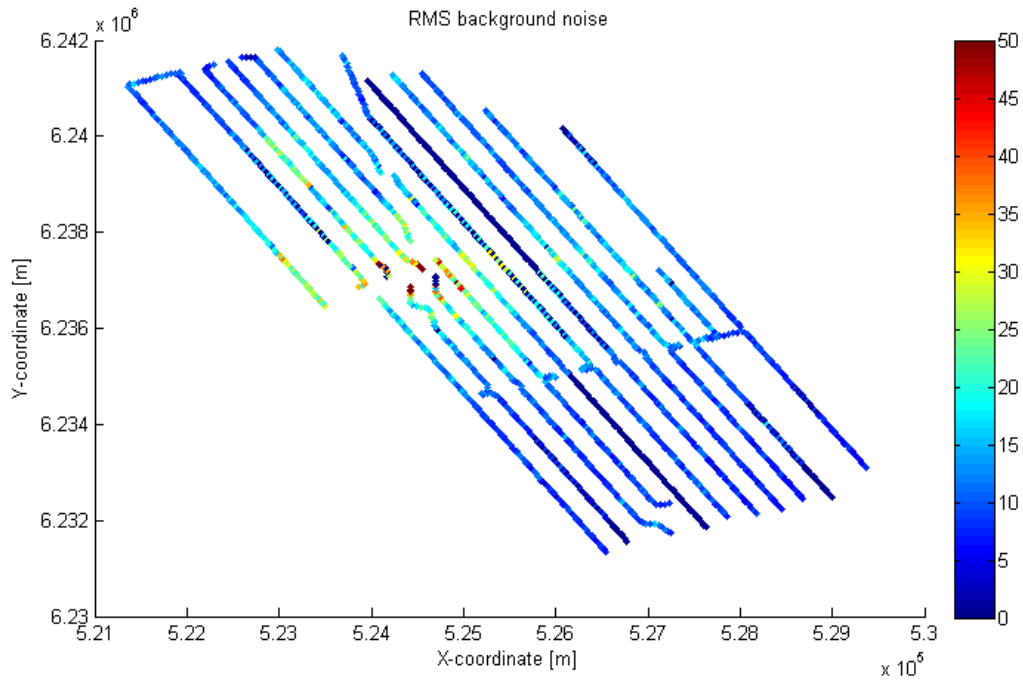
Figure 8.41: Displays the RMS background noise for the Valhall field. Color bar values are in µbar.
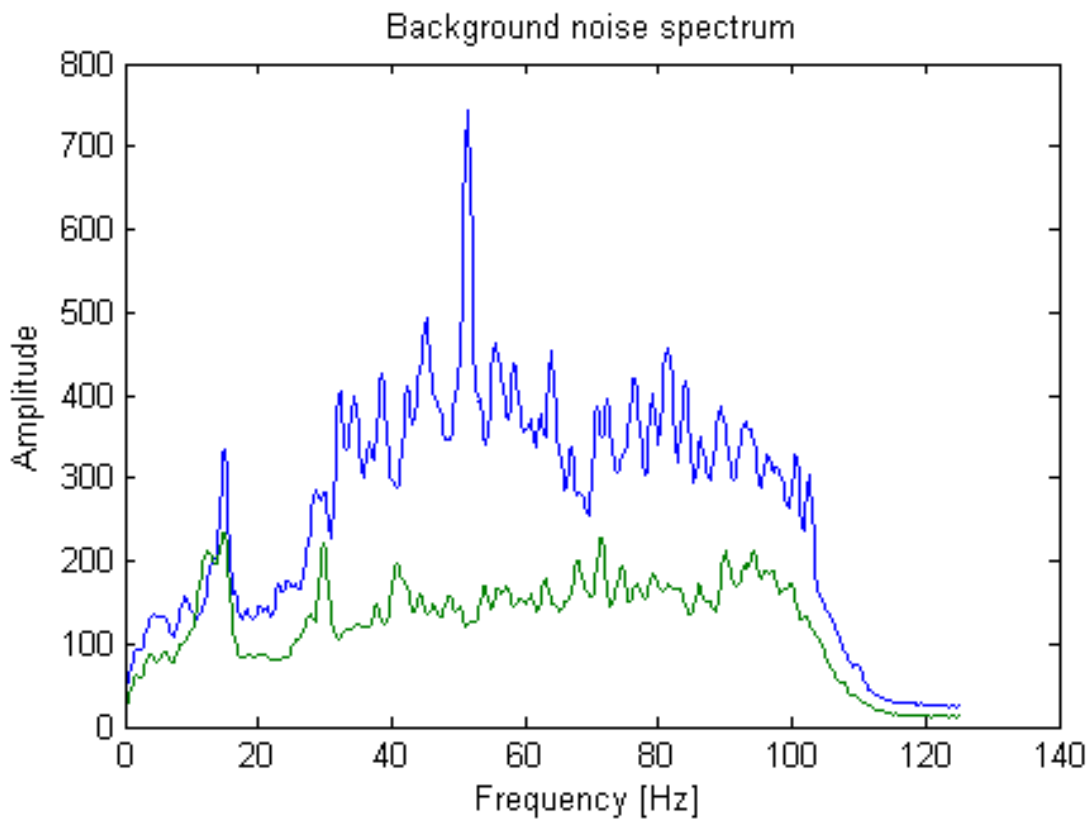
Figure 8.42: Shows the average noise frequency spectrum of the whole field.
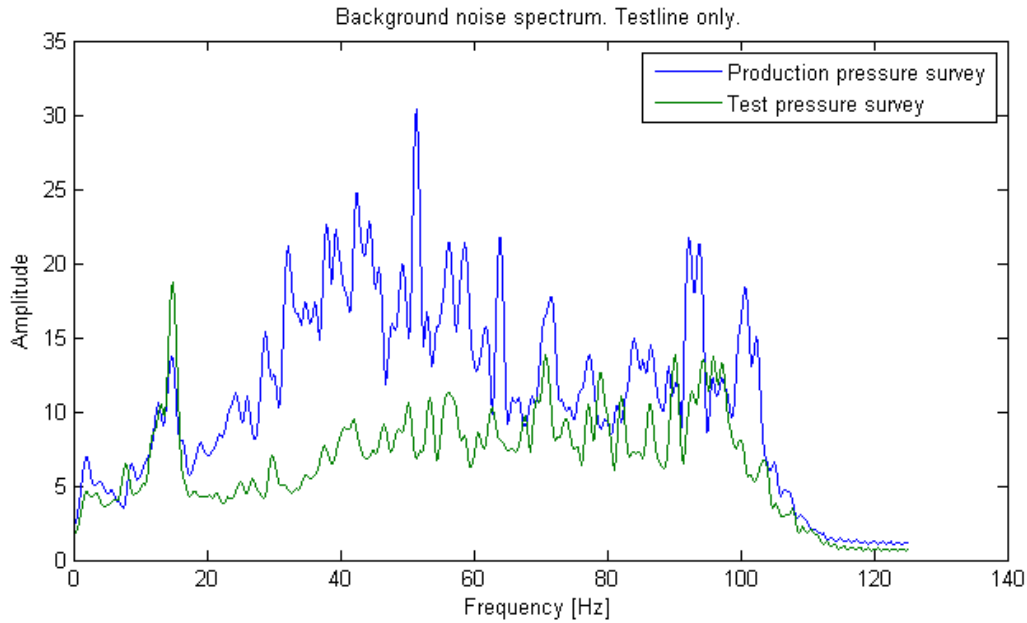
Figure 8.43: Shows the average noise frequency spectrum of the test line.

8.3.2 Positioning

Taken from the authors project work (Jakobsen 2012).

One of the biggest sources to 4D noise is in the misplacement of source and receiver from one survey to another. With the LoFS system the receiver cables are at fixed position and thus eliminating the receiver position as a variable. The source positioning on the other had is varying. By plotting the difference in source location on the respective shots the difference can be quantified and analysed.

From figure 8.44 it can be seen that the sources have some mismatch in the first 30 shots. These first shots are located at CDP 1-60 and will not contribute anything to the most shallow reflectors, and minimum to the deeper ones. After these shots the difference drops down to an average of 2.25 meters. This reveals a high quality repetition of the shot line that induces minimal 4D noise. It is still important to notice that some 4D noise due to the miss-positioning of the source could appear in the deeper reflections of the northern part of the seismic.
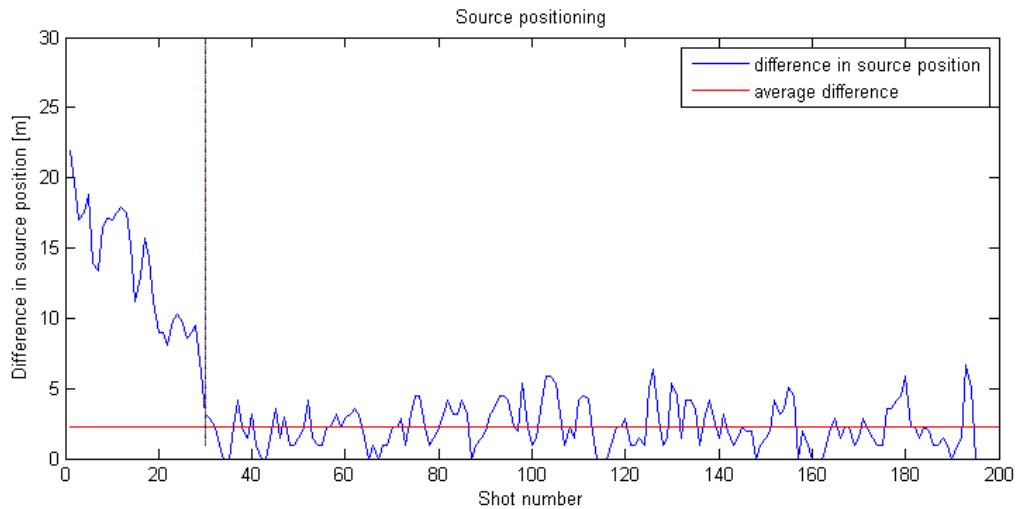
Figure 8.44: Shows the difference in source positioning and the average misplacement after shot 30. Shooting direction from north-west to south-east

8.3.3 Weather

Taken from the authors project work (Jakobsen 2012).

As an important source of background noise, the weather should be analysed. The wave-hight are considered the most crucial variable as this has the highest impact on the noise level. The nearest weather station is located at the Ekofisk complex, about 32 km north of the Valhall field. At open sea the weather is expected to have have insignificant variations over this distance and therefore these observations are good approximations to the Valhall weather conditions.

From the trace headers the date of acquisition was found to be 17th of September for the production line and 25th of September for the test-line. Both in 2011.

Figure 8.45 shows wave hight of respectively 1.8 and 1.1 meters which could account for variations in the signal. A wavy surface could induce noticeable variations in the ghost signal by varying the source depth as little as a meter. This effect is believed to be most prominent in the higher frequency area of the signal as the seismic waves tend to smooth variations in surfaces as the wavelength gets large compared to the variation.
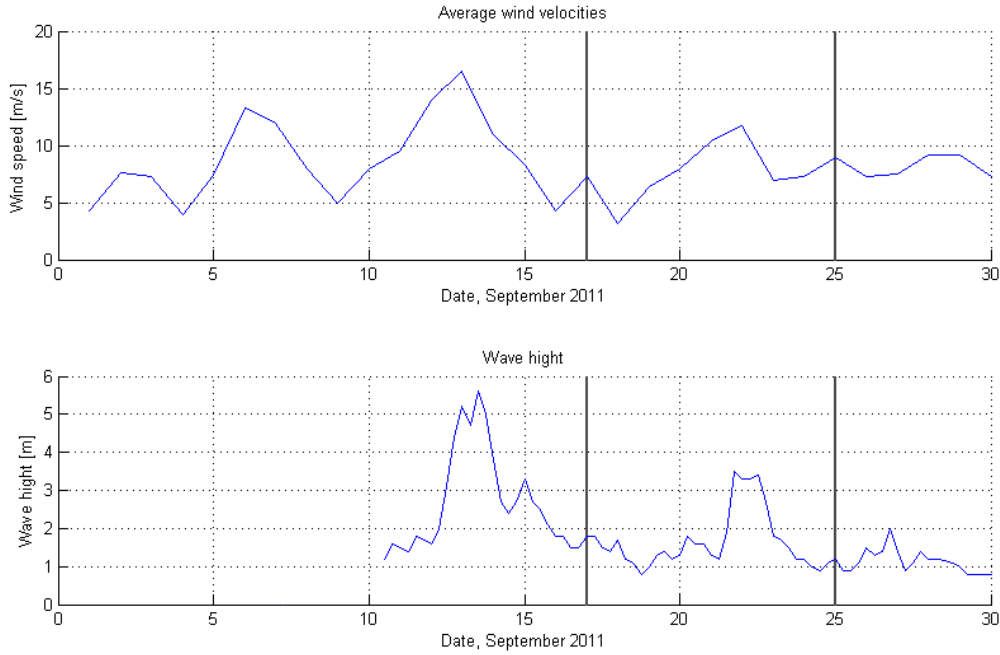
Figure 8.45: Top: Daily average wind velocity. Bottom: Wave hight. All data are from Ekofisk weather station (Lien 2012). Grey lines show time of acquisition

8.3.4 Nearby Acquisition

Modified from the authors project work (Jakobsen 2012).

By looking at the data sorted on shot number it is clear that both lines are polluted by an interfering wave field. This noise will mostly corrupt the deeper seismic as the amplitude recovery makes the late arrivals more sensitive to noise.

It is possible to remove the noise using a dip filter. This will have a small impact on the receivers that lies south of the acquisition boat but a higher impact on the receivers north of the shot (right of the shot in figure 8.46). On the northern (left) side of the shot the reflectors are dipping in the same direction as the interference and a filter would most likely remove some reflection energy. In the authors project work (Jakobsen 2012) with these data it was found that a pre stack FK-filter would corrupt the signals to an unwanted degree and that the best way to handle interfering seismic noise was to do nothing and keep all reflection energy.

To better understand the data, a filter could surgically filtered out everything but the dipping noise (figure 8.47), the noise could then be further analysed.

The filtered signal is then frequency analysed. Results shown in figure 8.48 reveals the interference noise to have a frequency content of about 10-30HZ. It is possible to bandpass-

61
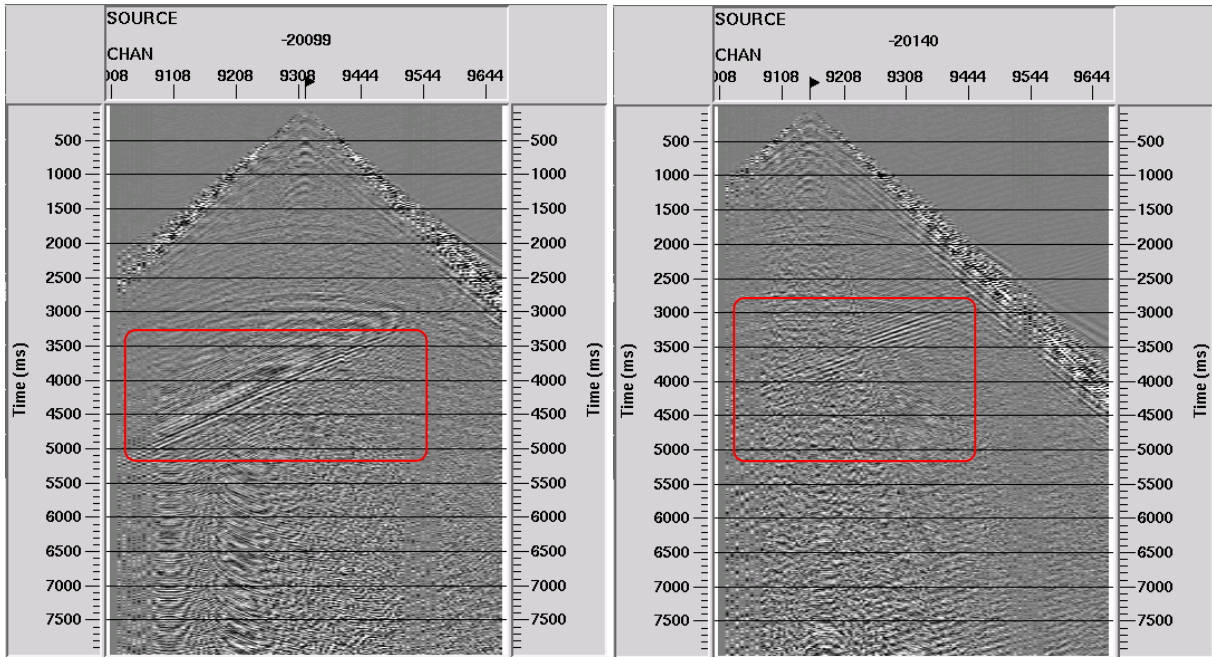
Figure 8.46: Shot-gather plot showing typical dipping interference noise (red rectangle). Left: production line. Right: test line.
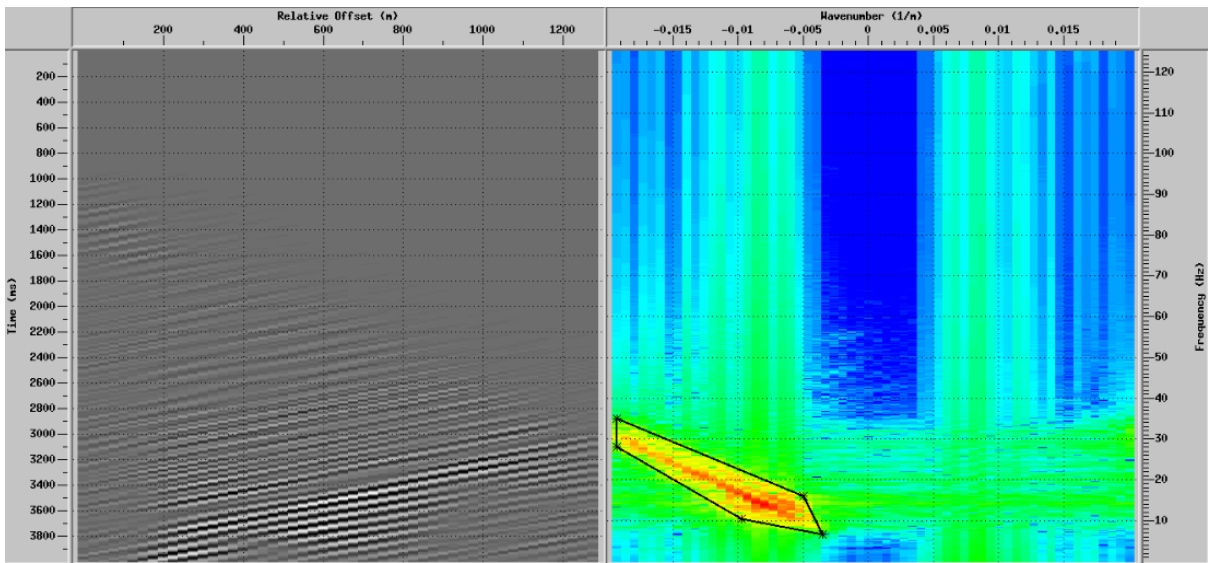
Figure 8.47: FK filter response showing the dipping noise.

filter away the noise, however a large part of the desired data lies within this range and a bandpass approach would ruin the the data.

By analysing the dip of the noise it is observed that the dip is of 17 ms per trace. If the interference were perpendicular to the receiver array the dip would have been 33 ms per trace. Using trigonometry it is possible to calculate angle of incidence to 33 deg as shown by figure 8.49. Due to symmetry it is difficult to say which of the two incidence angles
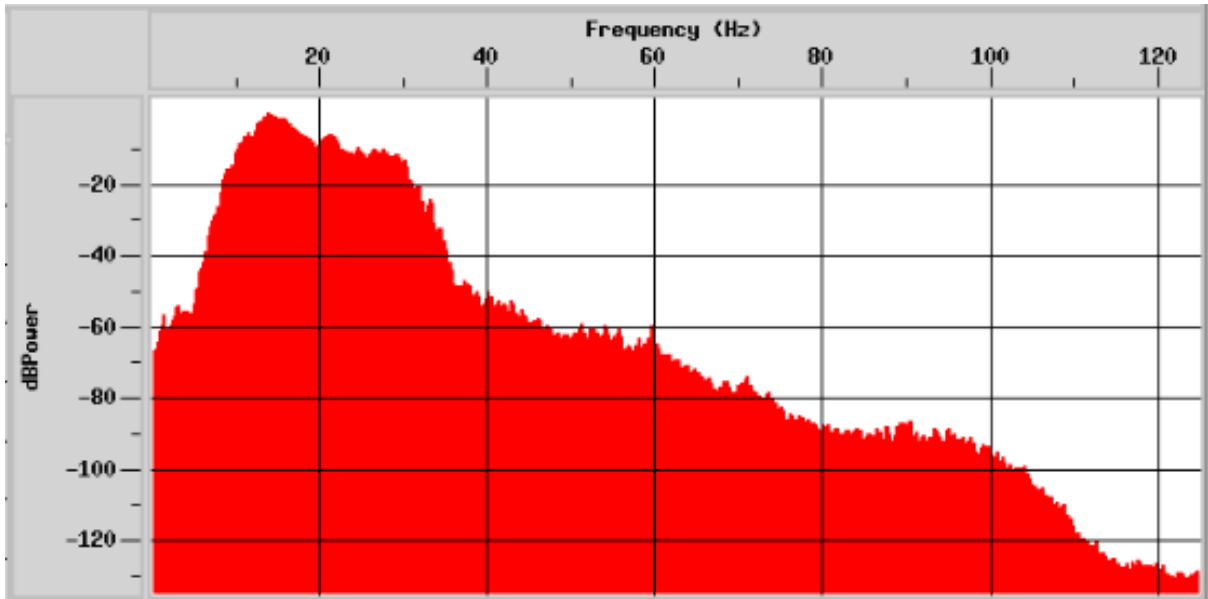
Figure 8.48: Frequency spectrum of the dipping noise.

the interference is coming from, but the most likely scenario is the line from the south as this is the area with the most offshore activity.
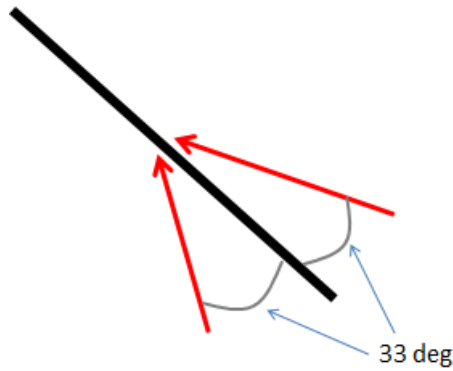
Figure 8.49: Angle of incidence for interfering seismic survey.

8.4 Reflector analysis

This section is based on discoveries made in the authors project work (Jakobsen 2012). The same analysis as described below was carried out for a seismic stack with and without pre-stack FK filter to remove the noise described in section 8.3. The findings showed that a pre-stack FK filter removed reflected energy to an unwanted degree and also increased the calculated noise. It has therefore not been used in this theses. For the noise calculations in this section the input data is the debubbled low- and high-pressure surveys as well as a difference stack between these. The processing flow used to derive the data is found in section 7.4.

Three prominent reflectors have been identified on the seismic and are subject to further analysis. The first reflector (R1) is located at about 620 ms, the second reflector (R2) is located at about 1750ms and the third (R3) is located at about 2700ms. Figure 8.50 shows how the analysed reflectors appears on the stacked production-pressure data. Figure 8.51 shows the analysed reflectors after flattening.

It is possible to extract the noise analysis by extracting the amplitudes from the reflectors of interest. By flattening the reflectors (figure 8.51) and extract the RMS amplitude based on a tight window around the now flat horizon it is possible to extract the reflectors amplitude (figure 8.52). This is done for all the reflectors (R1 R2 and R3) on both stacks and it is run through the same algorithm as described by equation 11-17. The result of each of the noise calculations are shown in figure 8.53. Since the noise is believed to be proportional with the inverse square root of the fold this is also plotted.

As figure 8.53 shows, the general trend of the calculated noise follows the inverse square root of the fold. However it is worth noting that while the noise level of R1 is located bellow the inverse square root of the fold, the noise levels increase above this line as deeper reflectors are analysed (R2 and R3).

Figure 8.54 to 8.57 contain the same data as shown in figure 8.52 and 8.53 plotted in a scatter plot. The noise reducing effect of increased fold is pretty clear in these plots. However by looking at the stack-plot in figure 8.57 it seems like there exists a limit to where an increase in fold affects the noise level. This is also observable to a certain degree in the other plots only with a bigger spread. Looking at equations 11 - 13 as well as 17 the noise consists of both random and more systematic 4D noise. Ashton, Bacon, and Dèplantè 1994 states that there exists a maximum fold where a further increase in fold will have minimum impact on the noise level. Based on the results in figure 8.54 - 8.57 this seems to be the case in this analysis as well. It seems like the noise base-level is

reached at fold 4-5 for R1, 10-15 for R2 and around 30 for R3. This base-level of noise will have a high systematic- to random noise ratio and could be used to determine how the systematic noise profile looks like. However, even if the plots seems to largely approach a base level, there exists large deviations.

From the information presented above, three different noise profiles have been identified. One based on the base-level noise described in the paragraph above and two based on a fold normalization process. The first method evaluates the noise data shown in figure 8.53 to 8.57 without any modification done. By extracting the mode (the most frequent occurring value) of the noise a good approximation to the baseline is derived. The result, shown in figure 8.59, is fitted with a quadratic function. Since the line is based on the base-line noise value (high fold values) it is dominated by the systematic noise level and is believed to be an indicator of the systematic-noise-level profile.

The other approach is based on all noise-information available by fold-normalizing the data. From figures 8.53 to 8.57 it is clear that the noise is greatly affected by the fold. Assumed that the relation in equation 31 is correct, it is possible to normalize the noise by multiplying the noise with the square root of the fold. This will make it possible to compare the three reflectors noise level and could therefore be used to estimate a noise profile. This has been done in two different ways with two different approaches. Both methods consists in finding a representative noise value for each reflector found by deriving the arithmetic mean and the mode of the data as shown in figure 8.58. Values shown with symbols in figure 8.60. By trial and error an adequate fit was found by regression of a $ax^b + c$ function. Since this method uses all the noise information given it is expected to contain more of the random noise component than the first method mentioned.

$$N_{stack} = \frac{N_{trace}}{\sqrt{fold}} \qquad \rightarrow \qquad N_{trace} = N_{stack}\sqrt{fold} \qquad (31)$$
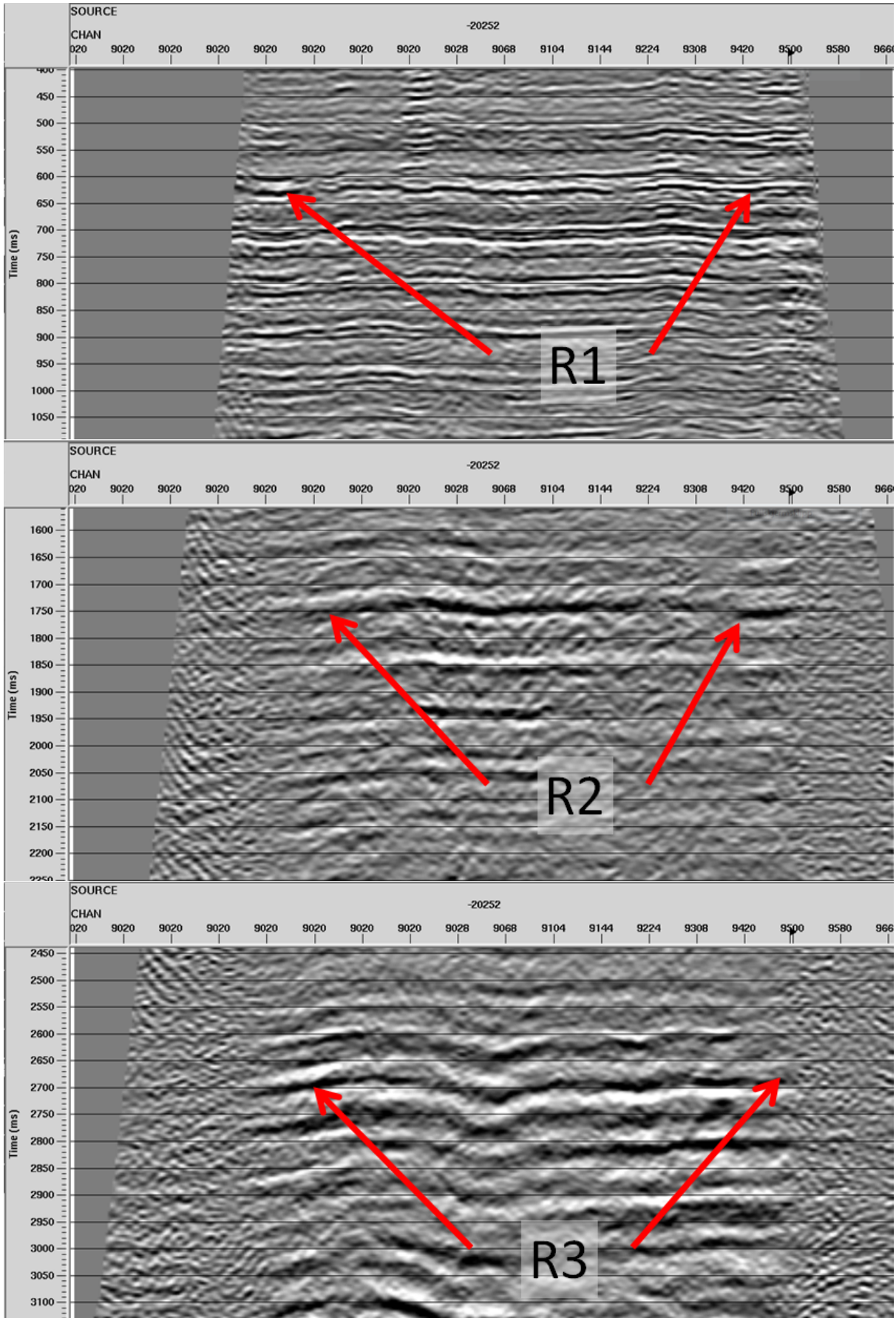
Figure 8.50: Reflectors shown on the seismic section shot with production pressure.

66
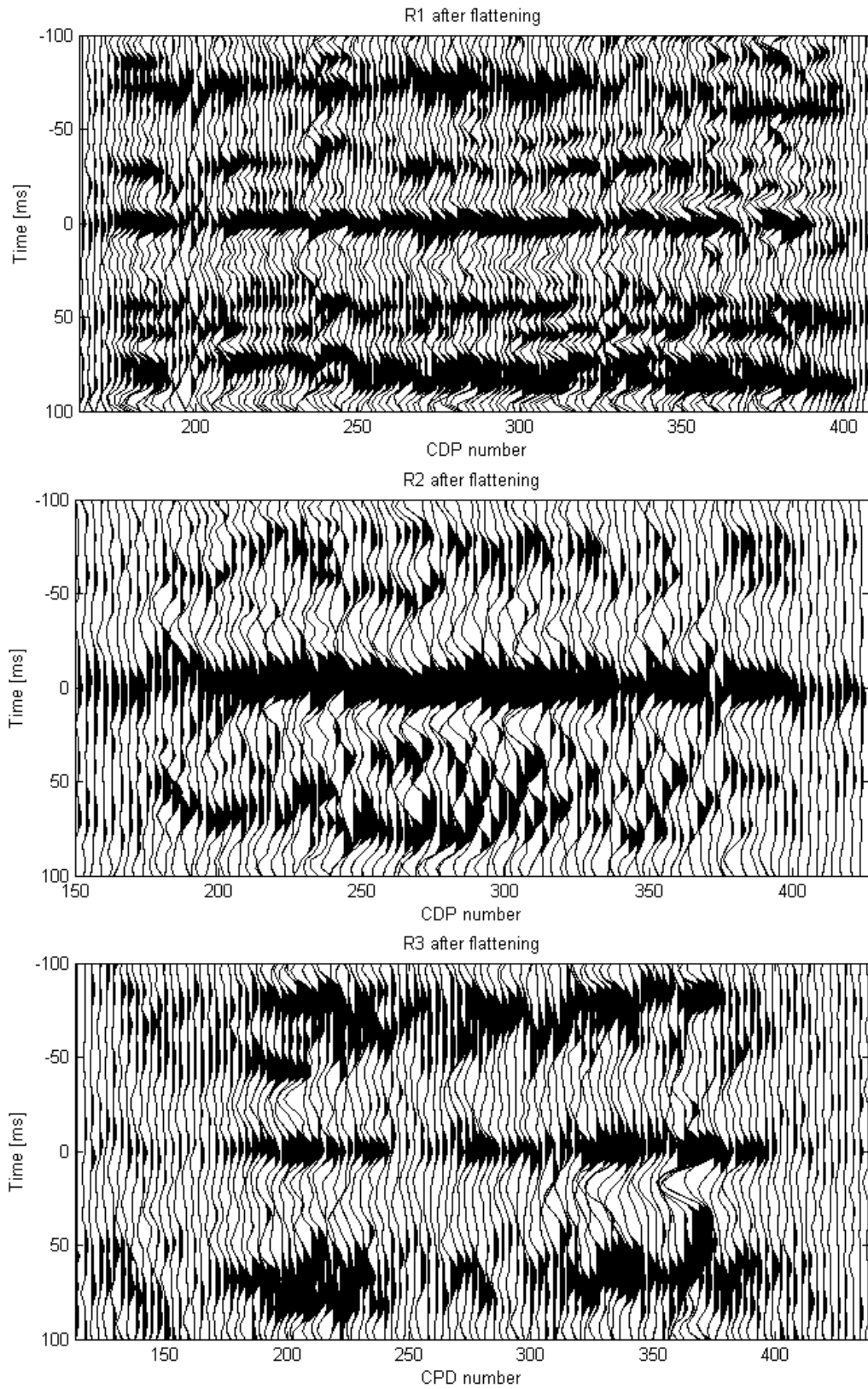
Figure 8.51: Reflectors shown on the seismic section shot with production pressure. After flattening.

67
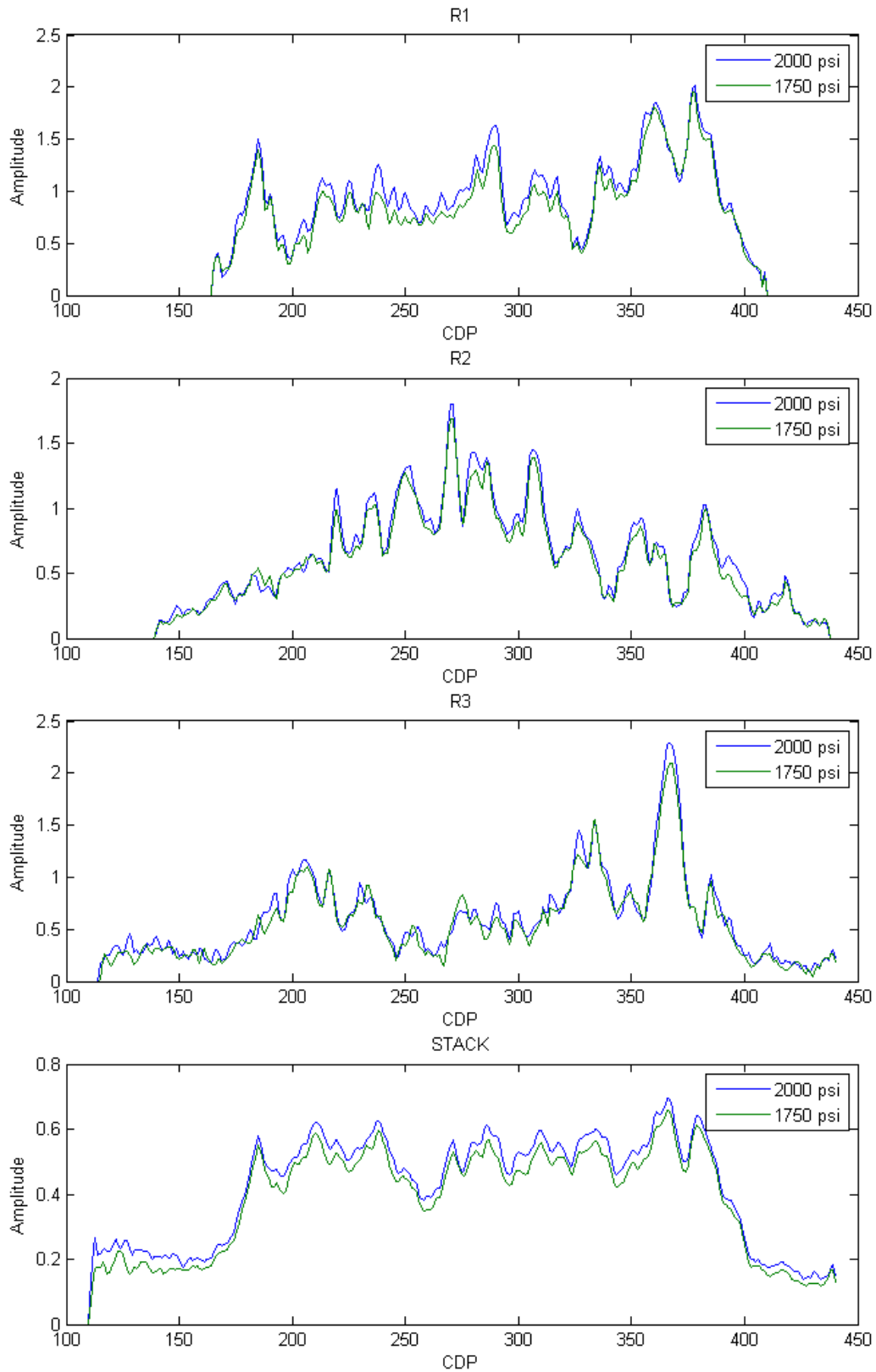
Figure 8.52: Shows RMS amplitude over reflectors 1-3 as well as the whole stack (RMS from 200-3000 ms). With and without pre-stack FK filter. RMS values averaged between the two surveys.
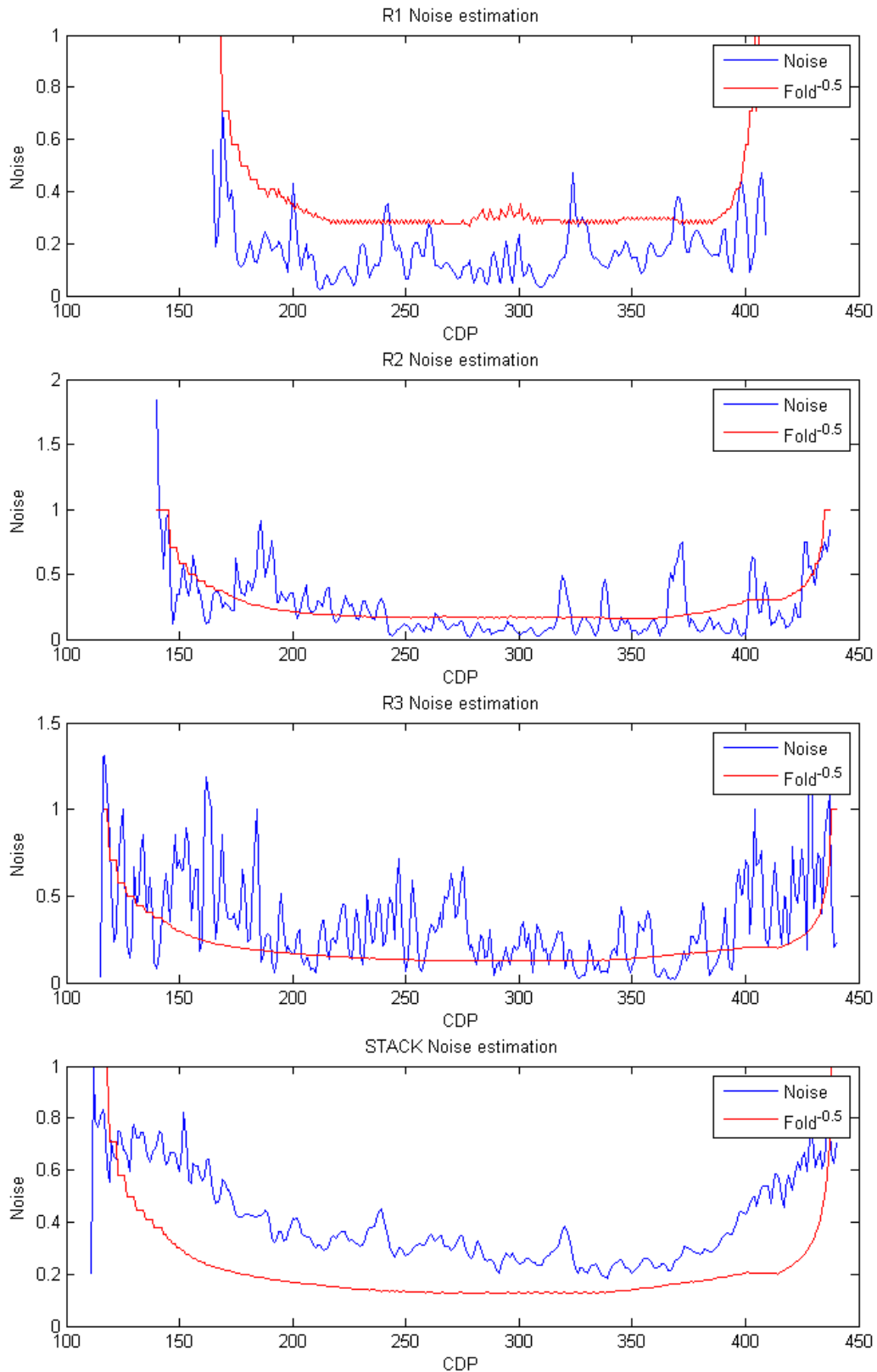
Figure 8.53: Shows noise over reflectors 1-3 as well as the whole stack (RMS from 200-3000 ms). With and without pre-stack FK filter.
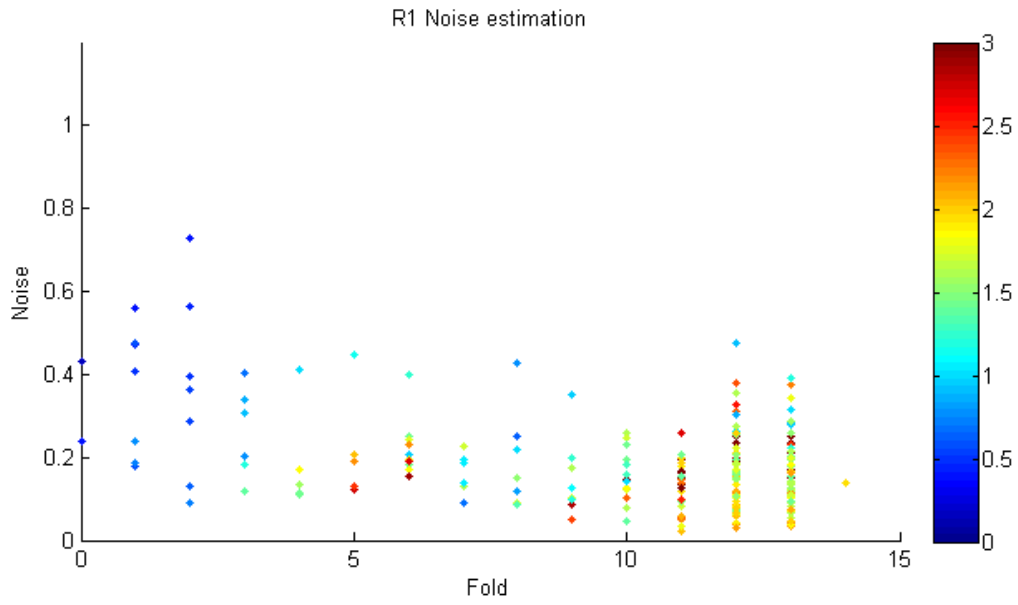
Figure 8.54: Scatter plot showing the interaction between noise fold and reflection strength of R1.
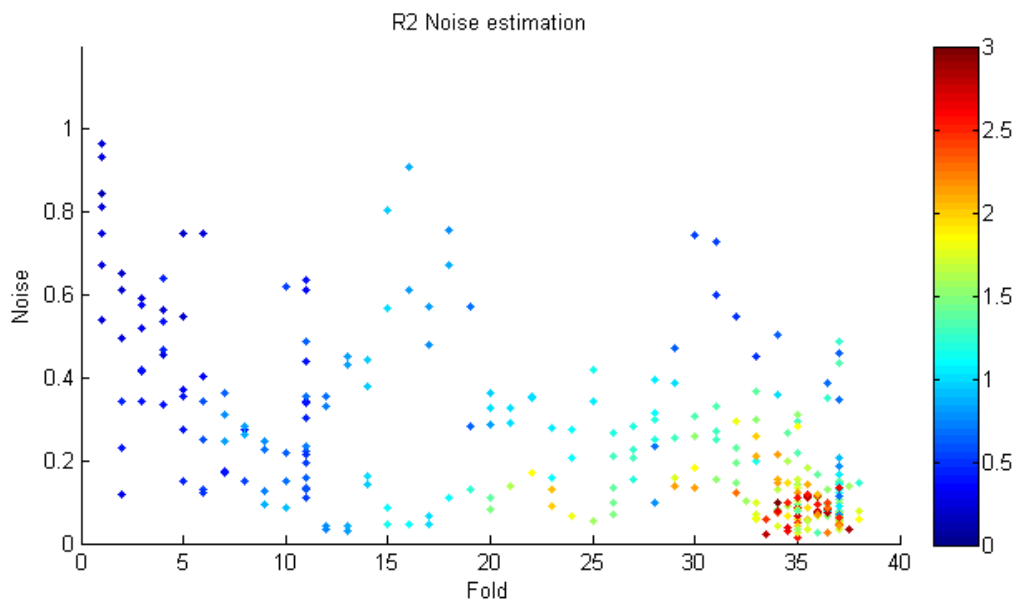
Figure 8.55: Scatter plot showing the interaction between noise fold and reflection strength of R2.
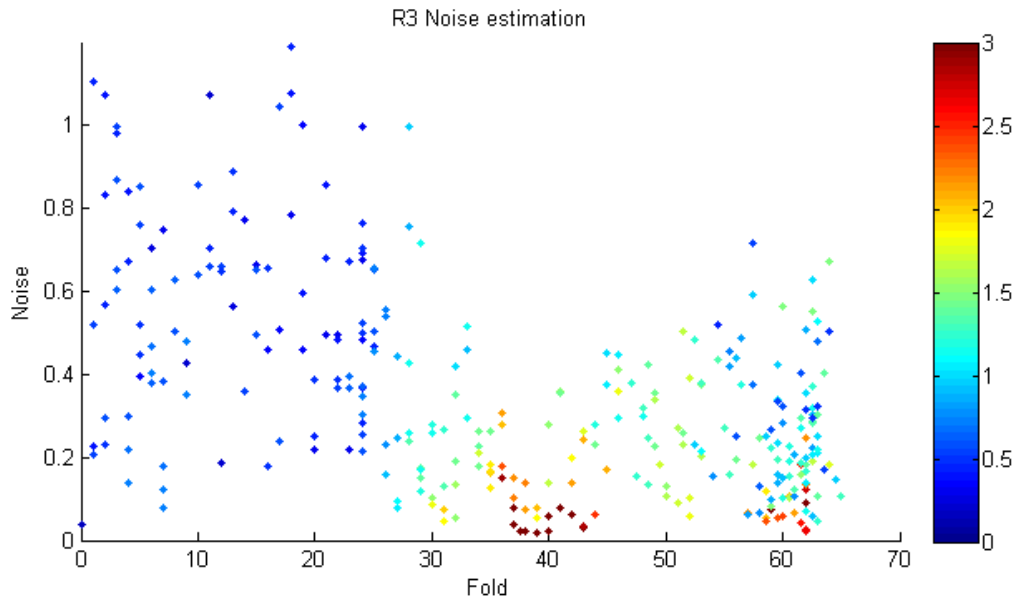
Figure 8.56: Scatter plot showing the interaction between noise fold and reflection strength of R3.
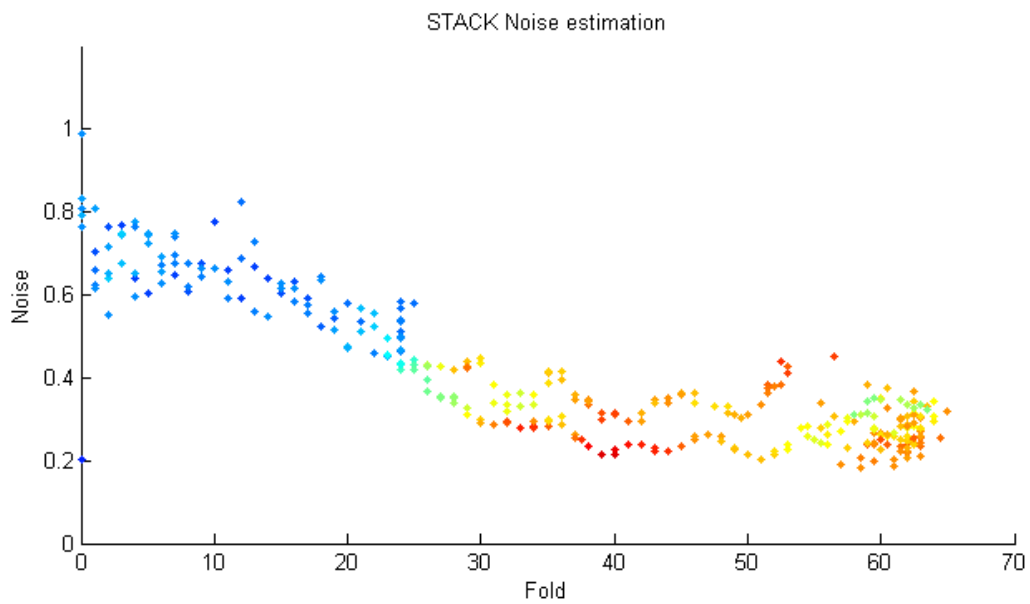
Figure 8.57: Scatter plot showing the interaction between noise fold and reflection strength of the stack.
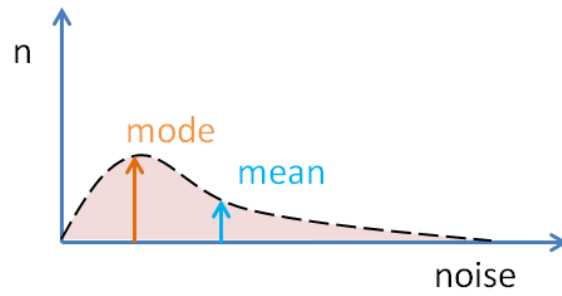
Figure 8.58: Shows the principle and basic nature of the mean and mode method.
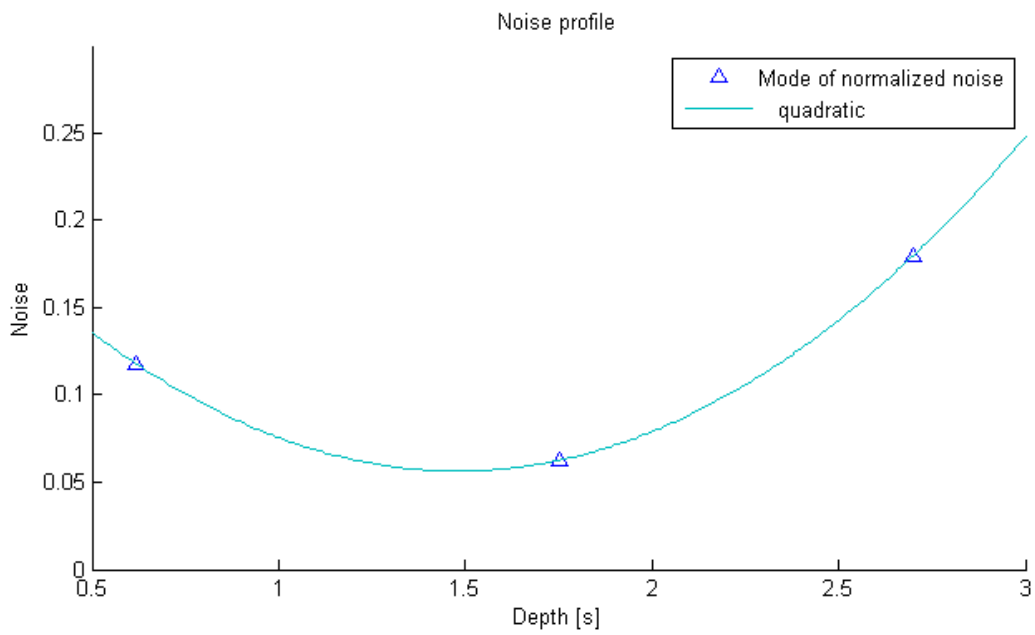
Figure 8.59: Shows the noise as a function of depth using the mode method to extract the noise-base value.
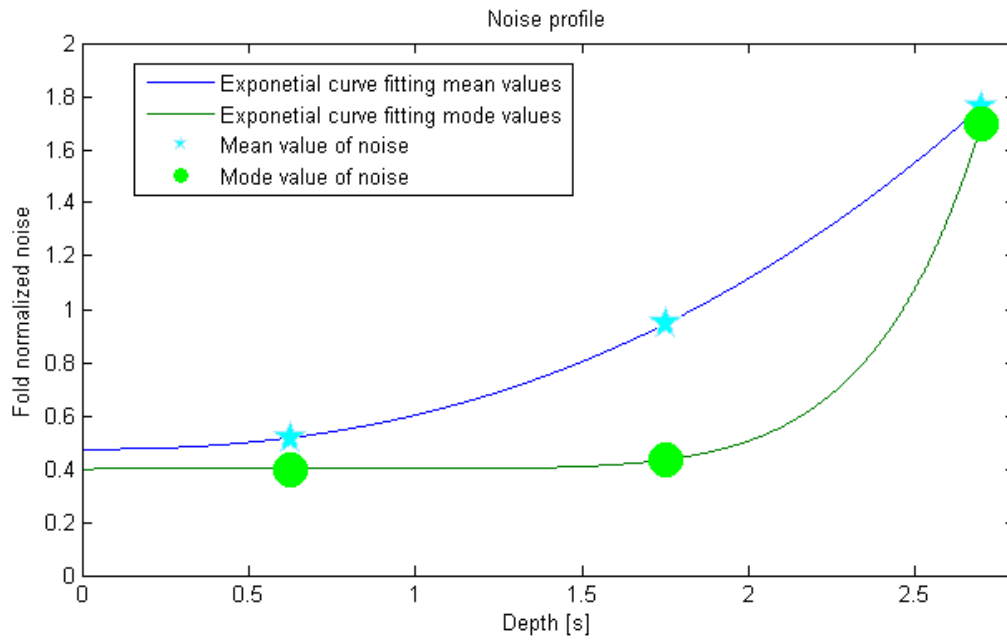
Figure 8.60: Shows the noise as a function of depth using both mode and mean method to extract the noise described in a normalized matter.

8.5 Q-Factor Estimation

In this section the same reflectors as in section 8.4 has been evaluated in an attempt to estimate the Q-value using a new experimental method suggested by the authors advisor Martin Landrø (more info in section 3.2). Since the anelastic absorption acts on a per-cycle basis the frequency content of the signal is expected to drop with depth. Figure 8.61 shows a F-t plot of the two stacked datasets. Notice how the frequency content of the data is reduced as a function of depth. Figure 8.62 shows the difference of the F-t plots and is used as a QC for further analysis. The black areas indicate where the difference is negative i.e. the test-line has a higher spectrum value than the standard pressure. This is not expected and could be explained by the poor processing of the data. Another observation worth noticing is the high difference cloud around 3000-3500 ms and 20-90 Hz. This cloud is interpreted as a noise cloud, possibly a response to the difference in the background noise levels of the two surveys (section 8.3). It is worth keeping in mind that these spectral data are normalized for each time value which means that the noise cloud gets more prominent with depth as the reflection strength decreases. Another interesting feature in the noise cloud is the dimming of the cloud around our two deeper reflectors. This indicates a higher signal to noise ratio and is regarded as a positive indicator for the validity of these reflectors. It is also worth noticing how the difference in figure 8.43 could be a cross line trough figure 8.62.
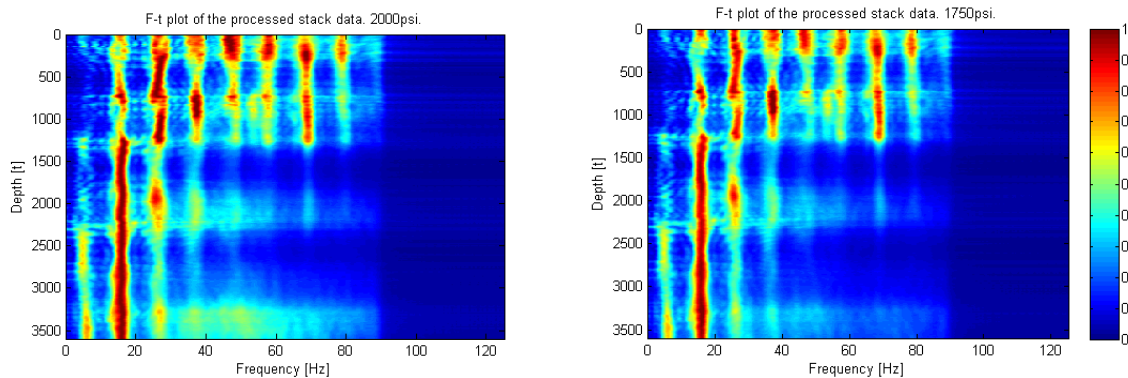
Figure 8.61: Frequency content as a function of depth. Left: 2000 psi. Right: 1750 psi. Normalized for each t value.

As mentioned above the data basis for this Q-estimation process is the three most prominent reflectors at 625, 1750 and 2700 ms displayed in figure 8.50 and 8.51. By running each of the reflectors trough the algorithm displayed in figure 8.65 an estimate of Q could be accomplished.

Firstly the datasets are loaded into the program after which a bandpass filter is applied. The filter used is a bandpass filter designed with the built-in Matlab filter design func-
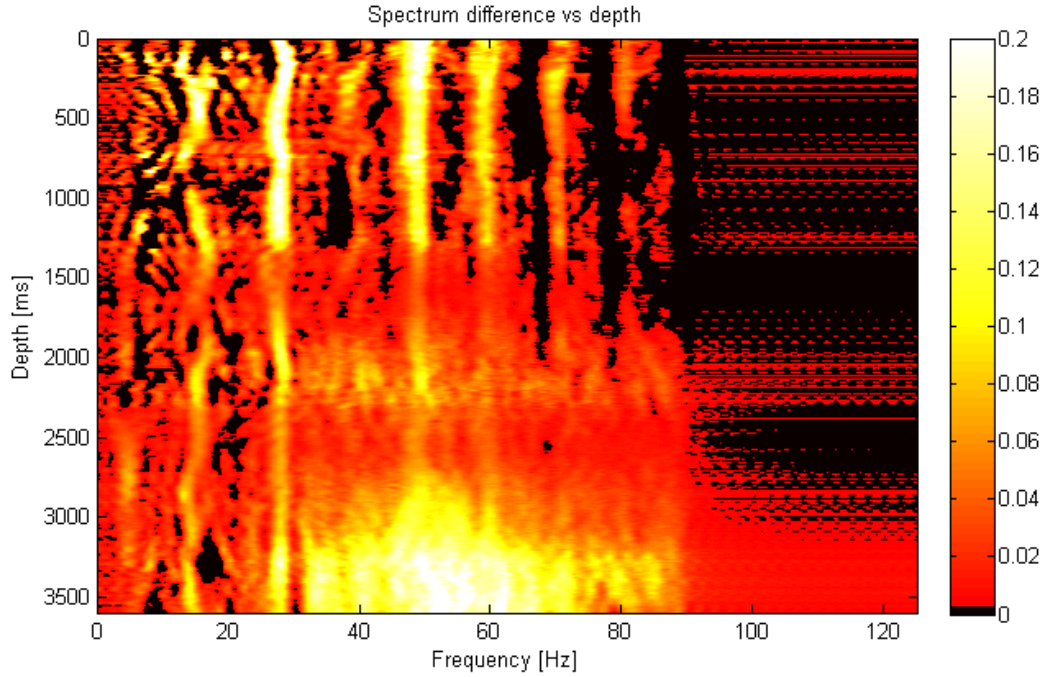
Figure 8.62: Shows the difference of the plots in figure 8.61.

tion. After the data has been filtered to a limited frequency content the amplitude is extracted from the reflector +-40 ms. By extracting the RMS amplitude from the data centred around the reflector the extraction of lower frequencies is easier, also since the multiple travel time is roughly 100 ms minimal multiple energy will be included. Then the difference of the two datasets are taken. The filter is moved one step and the whole process is repeated until k=kmax. The natural logarithm of the outcome of this process is shown in figure 8.63. In theory these lines should have behaved like straight lines. Since they are obviously not the next step would be to find a proper representation of the linear features of the lines. This could be done in several different ways. Firstly, by choosing data points from strong frequencies over the reflectors the data is believed to be most correct. The points are chosen based on the average spectrum of the given reflector shown in figure 8.64. Picked frequency values are found in table 3 The spectrum seems to show the same periodicity and representative values have been picked out. They are represented by stars in figure 8.63.

By using both the hand picked values and all available data from 5-80 Hz, two different slopes for each reflector was derived using the built-in Matlab linear regression function "robustfit". By combining the slope estimates with equation 22 it is possible to estimate a Q value for each slope. This is the average Q value to the analysed reflector, the interval Q factor is unwrapped using equation 23. These estimates are found in table

Table 3: Frequency values where the amplitude is large for reflectors 1-3.

Strong frequencies [Hz]				
R1	35	45	55	66
R2	12	23	35	NA
R3	12	23	34	NA

4. Both data selections seems to give plausible results when comparing the average Q-factor with normal values found in table 1. They are also both increasing with depth which is expected. However if the Q_{int} values are evaluated the hand-picked points gives a negative interval which is illogical. The intersection with the y-axis should also be taken into account to give a more complete understanding of the validity of the derived parameters. Even though the data has been corrected for geometrical spreading with a t^2 function, the deeper reflectors are still expected to weaken with depth as a result of transmission losses and reflectivity. The intersection with the y axis is therefore expected to decrease with depth. This is the case for the hand-picked data in the lower part of table 4. Based on the criteria of decreasing intersection with Y axis and plausible Q_{avg} and Q_{int} values, none of the derived Q value sets are believed to be good approximations. However, even though the points does not make sense in relation with each other, one (or more) of the values could be a valid estimate. It is expected that the reflector R1 will display the best results as it is the shallowest reflector with the strongest S/N ratio.

A further increase in application for this method could be achieved with a simple change in the algorithm in figure 8.65. By changing the averaging (fourth from the top) into a smoothing operation it is possible to derive a method that estimates how the Q value varies along the line. The result is shown in figure 8.66. These Q-values are derived from all frequency data only. The reason for this is that the algorithm for deriving the horizontally varying Q values seems to be unstable due to the few data points used in the regression.

Figure 8.67 show the result of equation 23 used on the laterally varying data in order to extract an interval Q-factor. For the first interval the average Q-factor is the same as the interval Q-factor giving the same result as in figure 8.66. The $Q_{int,2}$ calculation showed an unstable behaviour (as discussed section 3.2) while the $Q_{int,3}$ show a more stable behaviour. The reason the $Q_{int,2}$ is unstable is because of a to large increase in the the average quality factor from R1 to R2. Physically this corresponds to the signal being amplified in interval 2 which is logical unsound.
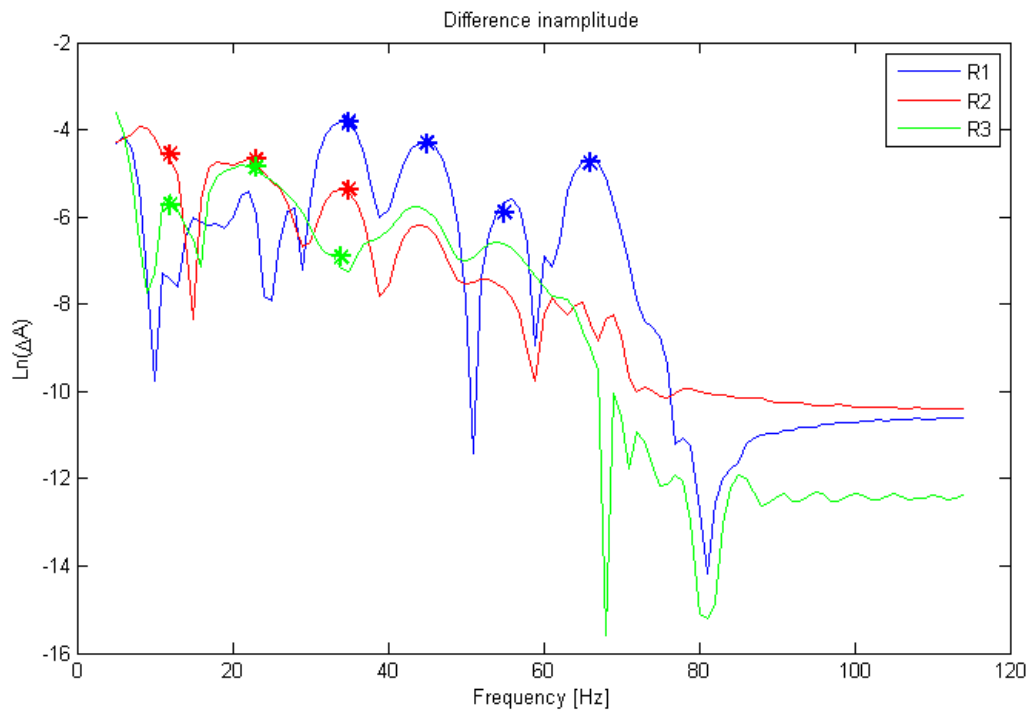
Figure 8.63: Shows the natural logarithm of the amplitude difference for reflectors R1, R2 and R3.

Table 4: Showing Q value estimates for both data selection for all three reflectors

	Intersection with Y axis	Slope	Depth	Qavg	Qint
R1 - All data	-4,668	-0,049858	0,625	39,38	39,38
R2 - All data	-3,9355	-0,077579	1,75	70,86	127,49
R3 - All data	-3,6863	-0,099222	2,7	85,49	137,89
R1 - Selected points	-2,6133	-0,041432	0,62	47,01	47,01
R2 - Selected points	-4,0386	-0,035787	1,75	153,62	-628,86
R3 - Selected points	-4,5973	-0,053586	2,7	158,29	167,67
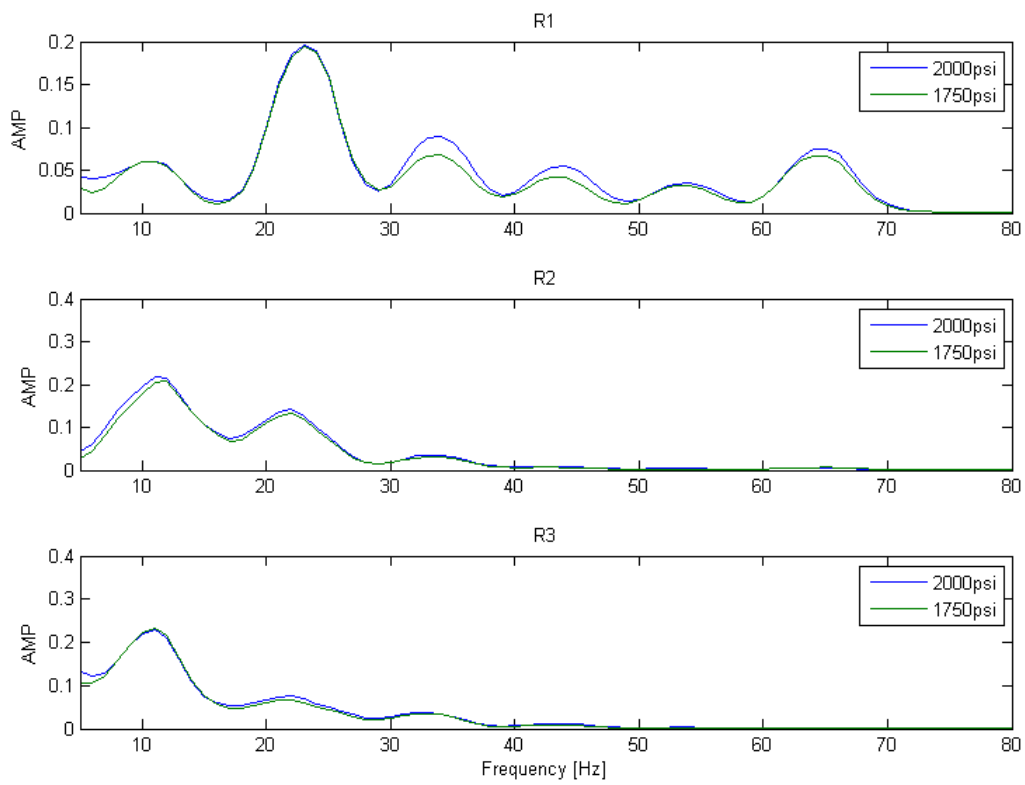
Figure 8.64: Spectrum of reflectors R1, R2 and R3.
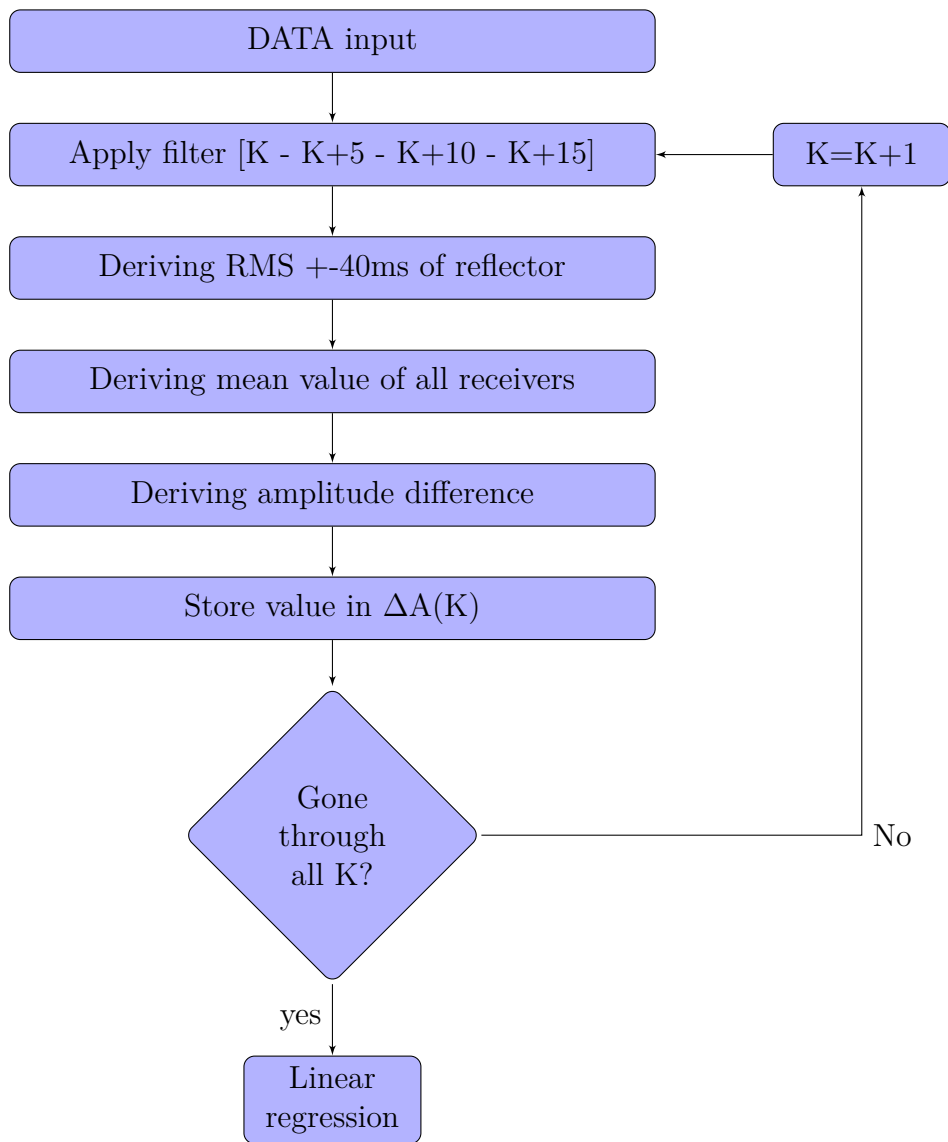
Figure 8.65: Flow chart describing the Q extraction process
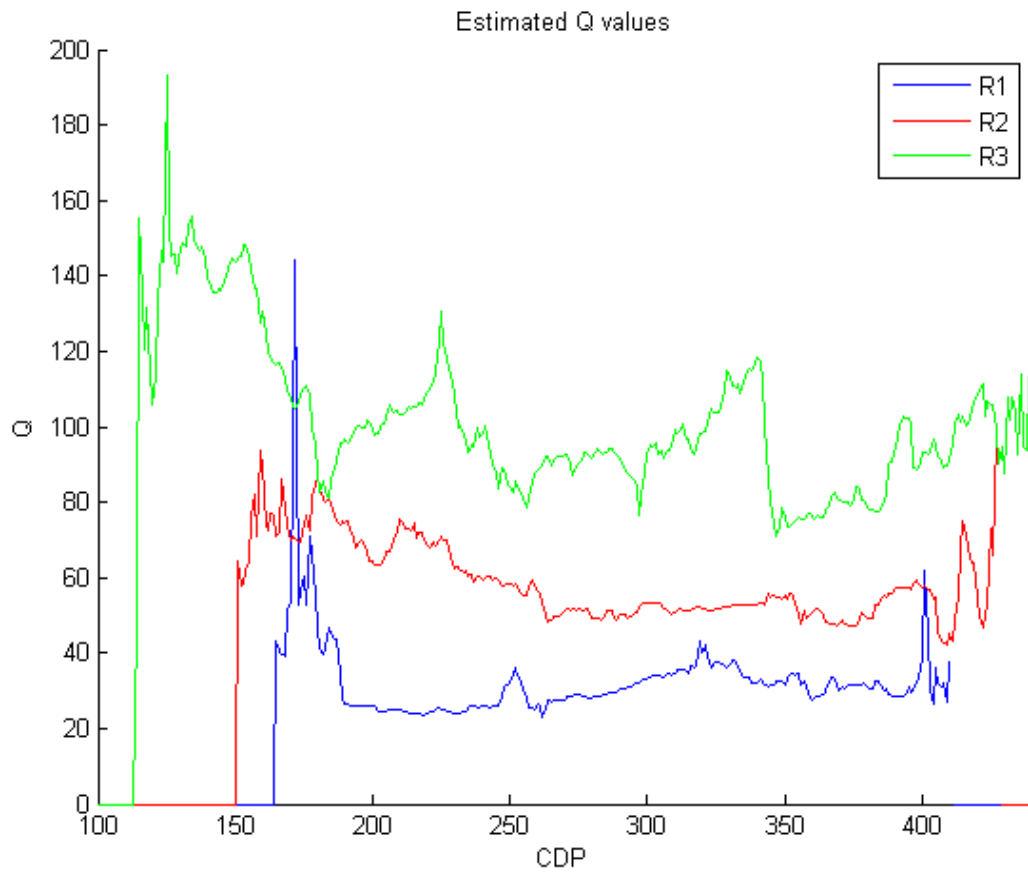
Figure 8.66: Q value estimation. Inline variations.
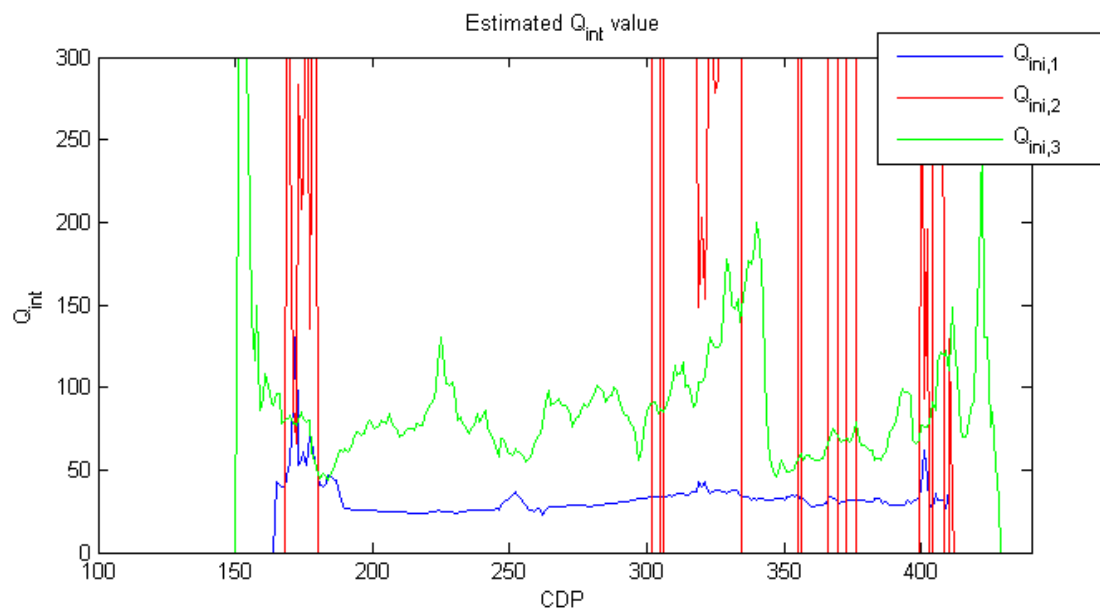
Figure 8.67: Q_{int} value estimation. Inline variations.

9 Discussion

In order to provide an efficient managing of a 4D project, it is important to know how large changes are observable. By simulating a change in the reflector-strength by varying the source pressure a noise evaluation could be preformed as a part of the first survey. Together with rock physics it is possible to determine when the changes in seismic parameters are big enough to be observed, thus improving the understanding of the seismic. This test-survey was a response to an idea proposed by Martin Landrø (M. Landrø 2008) with a main motivation of determining the 4D noise. Along the way several different phenomena has been detected and analysed. In addition a new method of utilising the different pressure lines to derive the quality factor was investigated.

The line analysed was processed by a simplistic processing flow which is considered below production standards. No attempt was made in order to remove the multiple reflection energy or migrate the data. It is believed that in order to keep the original amplitude relation between the surveys special care should be taken. The author therefore chose to keep the processing flow simple in order to not corrupt the amplitudes. Nevertheless the data should optimally have been processed as two vintages in a 4D survey with production standards.

By reducing the firing pressure from 2000 psi to 1750 psi, the amplitude in the reduced pressure survey is theoretically expected to be about 91.5% of the production pressure survey. However several amplitude analysis was conducted and suggested a more subtle change than theoretically expected. Table 5 shows the results of the different amplitude analysis. As described earlier all these analysis are conducted on different data-selection, with different methods and they all but two suggest that the pressure reduced amplitude is more around 95%. The exception is the optimal scaling factor analysis of the whole data as described in first part of section 8.2.2. This is the only test with all offset data included and should be compared with the other test results with care. As suggested by the apparent reflection coefficient in fig 8.10 the changes in directivity as the pressure changes is not understood and should be further investigated. Another test that gives similar results as the theoretical estimate is the optimum scaling factor analysis done on the Nucleus simulated wavelet. In this simulation the receiver is located 60 meter straight bellow the source array and should be comparable with the other "direct data" analysis. It should be noted that the difference in amplitude is derived by spectral division and may not be comparable with what equation 29 means with amplitude change. Since the most likely meaning of an amplitude change would be by comparing the RMS value of the given wavelet the "RMS value. Direct data" test should be a good comparison. This

test has however a deviation in reduction of amplitude of about 45% compared to the theoretical value. If the rawest and most unaltered signal is analysed, the direct wave without ghost, the change is even more subtle.

If the change in pressure is taken into the frequency domain the analysis show an amplitude difference varying both with frequency and offset as shown in figure 8.25-8.26. The most unaltered signal, the minimum offset direct wave without the source ghost (figure 8.30) show a behaviour similar to that of the simulated wavelet in figure 8.38, disregarding the difference in amplitude change. This indicates that the changes in amplitude difference as a function of frequency could be a result of changes in the source ghost signal. The analysis done on the pure ghost reflection shows a high difference in the lower frequencies (0-30 Hz) a negative difference in the mid frequencies (30-70 Hz) and a lower positive difference again in the higher frequencies. This indicates that the cause of the frequency dependence for the amplitude difference is rooted in changes in the ghost signal. Possible explanations for these changes could be a "wavy surface effect" that changes the seismic signature as it is reflected from the sea surface (Laws and Kragh 2002). Another possible effect could be that as the bubble characteristics change the weak early bubble signature could interfere differently with the source ghost for the two set ups. The latter could have been more thoroughly investigated if the seismic signal without source ghost was derived. This was not done and could be a way forward in order to better understand the amplitude difference variations.

There are still great uncertainties regarding how the source response change as a function of firing pressure and further research should investigate both how the signal changes (both in frequency and amplitude domain) and why it deviates from the expected theoretical value. But one thing should be concluded from these tests; they indicate a different change than theoretically expected.

Since the amplitude variation analysis for the most part implies a more subtle amplitude change than simulated in nucleus, it should also be mentioned that this could have impact on the debubble-filter used. Since the debubble-filters was derived based on the simulated nucleus pulse where the simulated source of 1750 psi was about 92% of the production 2000 psi pressure. Ideally the debubble process should not corrupt the amplitudes, but it should be noted that the debubble filter may have been derived on unsuitable wavelets and corrupting the analyses done on the stack in section 8.4 and 8.5.

Another effect poorly understood with a potential for corrupting the results is the instability of the receivers. As previously discussed (section 8.2.1) the response of the different receivers seems to display an inconsistent behaviour. Since the Valhall LoFS project is

Table 5: Amplitude data

Methode	Percentage of production pressure
Theoretical	91.5%
Maximum value. Direct data	95.8%
Minimum value. Direct data.	94.6%
RMS value. Direct data	95.0%
Optimal scaling factor. All data	89.9%
Optimal Scaling factor. Direct data	94.1%
Optimal Scaling factor. Nucleus	92.2%
Spectrum division. Direct signal (no ghost)	95.7%
Spectrum division. Ghost signal	96.4%

the first full sized project with permanent receiver cables it is possible the receivers are not holding up after nine years at the sea-bottom. If this is the case it would corrupt amplitude analysis done across receivers. Although the absolute values given by the receivers may vary, the relation in which a signal increases, should be usable as long as the receivers are showing the proper amplitude relations. Meaning a pressure increase from 100 to 1000 µbar should give the same difference in response as a change in pressure from 1100 to 2000 µbar. Less dramatical explanations would be the variation of ultra-shallow reflectors and known difference in sensitivity. It is recommended to preform further analysis on the life of field set-up at Valhall. An interesting approach would be to compare direct arrivals from the first LoFS survey with the data from LoFS 14 to see if the receiver stability has been compromised during the years.

Since no known work has been done on a source variation survey no established method of deriving noise exists. The method used in this thesis is therefore not absolute and caution should be used when evaluating its results. For further improvements other ways of deriving the noise should be investigated.

The noise derivation analysis done implies an general increase in noise with depth. Some methods has been investigated in order to quantify how the noise change with depth. Since this is the first multi-pressure survey shot (to the authors knowledge), no established work flows exist. The nature of the noise term derived is not fully understood but the analyses done implies that the noise consist of a random- and a more systematic component.

By increasing the fold the random noise component could to a certain degree be suppressed. If noise from different areas of the stack should be analysed they could be multiplied with the square root of the fold in order to normalize the noise and make it comparable. Another approach is to derive the base noise level i.e. the high fold "base

noise" level. Both these methods has been used with results displayed in figure Figure 8.59 and Figure 8.60. In figure Figure 8.59 R2 seems to have a lower noise value than R1. This is counter intuitive as the noise is generally believed to increase with depth. It could however be explained by that the more shallow reflectors is more effected by the ground roll (observable as two straight lines radiating from the shot position in figure Figure 8.46). Even for the fold normalized noise profile R2 seems to contain similar amounts of noise as R1. This could be a result of the same ground roll and the fact that it is not random and therefore the normalization process is illogical. Nevertheless the mean method of deriving a value for the normalized noise terms seems to give an expected result. Efforts should be made in obtaining increased understanding of the noise derivation equation (equation 17).

Another interesting application for a source varying survey is the possibility to derive the formation quality factor. Previous methods compares the frequency content of the output signal with that of a deeper signal and estimates the quality factor based on the frequency decay profile. Since these methods compares the signal with different travel paths, travel time and possibly recording methods there are many variables that could corrupt the data. By having two identical surveys shot with different source strength the new method of deriving the quality factor is believed to be more accurate. Since both signals have been through the same processes in the ground and in the processing step the only thing that should be different is the difference in amplitude and absorption. The method has been demonstrated on the dataset in section 8.5 with some success. By using both a selection of frequencies with a high amplitudes and all available amplitude-difference data the results are to some degree plausible. However several factors question the validity of the quality factors derived. Both unlikely interval estimations of the quality factor and illogical derived y-axis crossings implies an incorrect result. To validate the estimates found in this thesis the estimated q values should be compared with estimations made by BP with conventional methods. Despite some unlikely results the method is considered to have great potential. As previously mentioned the change in signal is found to be around 5%, if the amplitude change change were to be higher the analysis would not be that susceptible to noise leading to a more accurate result. Also if the data had been processed by a higher standard the result could also have been better. In figure 8.64 it is clear that a periodical feature with a periodicity of 10 Hz is present in all reflectors. This corresponds well with the multiple reverberation time, around 95ms, which gives periodical notches in the frequency spectrum of about 10 Hz. Although the amplitude extraction window was designed to minimize multiple energy it is clear that the removal of multiples was unsuccessful. If the multiples were to be removed in a responsible matter when processing the natural logarithm of the difference of the spectra would contain

84

more information and give a more linear slope resulting in a more accurate q-estimation. An attempt on deriving the spatial q factor has also been conducted. Although the results are found unlikely when deriving the interval q-value the first line could still give a rough estimate of how the q-factor varies laterally along the line. Further research on this method is highly recommended as the q-factor is a parameter that contain important information about the rock properties. It is also imaginable that as the q-factor estimation gets more accurate it could be conducted 4D quality factor estimations to aid monitoring both fluid- and rock property changes.

10   Conclusion

Since this is the first study done on data with different pressure no established method of utilized the potential exist. The work in this theses should therefore be regarded as suggestions on application for this type of data.

One of the most interesting findings in this study is the possible inconsistency in the LoFS receivers. If the integrity of the receivers has been altered care should be taken when investigating the findings in this thesis.

For the noise evaluation and Q-factor estimation the biggest uncertainty is the validity of the processing. Care was taken in order to keep the same amplitude relations induced by the different firing pressure. However it is believed that the debubble process could have altered this relation slightly.

If this type of survey should be a more common occurrence it would be wisely to understand how the amplitude changes with alterations in firing pressure. The evaluation done in this theses suggest that the established equation (Equation 10) gives an incorrect value for the amplitude change. With the findings in this thesis this claim should be further investigated with a study dedicated to the connection between source firing pressure and seismic amplitude. It should also focus on how the amplitude spectra change with firing pressure.

A method of evaluating the noise profile using several different methods was established suggesting both a continuously increase in noise with depth and also a decrease from the first to second reflector. The validity of the derived noise term is not perfectly understood and should be further investigated.

Using the same survey shot with the intentions of deriving 4D noise, it is also possible to estimate the quality factor in the formation. The attempt in this thesis is the first attempt on real data and gives somewhat plausible results. It is believed that the validity of the results could be increased further with better processing of the data and a stronger source strength variation.

References

Amundsen, L. and M. Landrø (Oct. 2007a). "4D Seismic – Status and Future Challenges, Part I". In: *GeoExpro*, pp. 66–68.

— (Dec. 2007b). "4D Seismic – Status and Future Challenges, Part II". In: *GeoExpro*, pp. 54–58.

Ashton, C. Peter, Brad Bacon, and Christian Dèplantè (1994). "3D Survey Design". In: *Oilfield Review*.

Bale, Richard A. and Robert R. Stewart (2002). *The impact of attenuation on the resolution of multicomponent seismic data*. Tech. rep. REWES.

Barker, D. and M. Landrø (2012). "Controlled source strength variation by changing the firing pressure - a sensitivity study for 4D calibration". In: *Geophysical Prospecting*.

Barkved, O. I., L. Amundsen, and M. Landrø (2009). "The Valhall LoFS Project". In: *GeoExpro*.

Barkved, Olav et al. (Sept. 2003). "Valhall Field - Still on Plateau after 20 Years of Production". In: *Society of Petroleum Engineers*.

bp.com (Dec. 2012). *Valhall*. URL: `http://www.bp.com/genericarticle.do?categoryId=9003561&contentId=7007483`.

Explorational Seismology [Utdrag] (1995). Tapir akademiske forlag.

Gassmann, F. (1951). "Über die elastizität poröser medien". In: pp. 1–23.

Hansen, Thomas M. (2013). *SegyMAT : Read and Write SEG-Y files using Matlab and Octave*. URL: `http://segymat.sourceforge.net/`.

Jakobsen, Fredrik G. (2012). "Estimation of 4D parameters by source strength variation - project work". Semester Project. Department of Petroleum Engineering and Applied Geophysics, NTNU.

Landrø, M. (1999). "Repeatability issues of 3-D VSP data". In: *Geophysics*.

— (2008). "Source strength variations and 4D seismic". In: *SEG Las Vegas Annual Meeting*.

Landrø, Martin (June 6, 2013). "METHOD OF ESTIMATING ATTENTUATION OF SEISMIC WAVES". Patent GB1310014.4. (UK).

Laws, Robert and Ed Kragh (2002). "Rough seas and time laps seismic". In: *Geophysical Prospecting*.

Lien, Trond (2012). *Weather-data from the Ekofisk area*. Tech. rep. Meteorologisk institutt.

matlab.com (May 2013). *Matlab*. URL: http://www.mathworks.se/products/matlab/.

Mindlin, R.D. (1949). "Compliance of elastic bodies in contact". In: *Journal of Applied Mechanics*, pp. 259–268.

Munns, J.W. (1984). "The Valhall Field: a geological overview". In: *Marine and Petroleum Geology*.

NPD (Apr. 2012). *Valhall*. URL: http://www.npd.no/en/Publications/Facts/Facts-2012/Chapter-10/Valhall/.

"Petroleum Geoscience: From Sedimentary Environment to Rock Physics, chapter 19" (2010). In: Springer Heidelberg. Chap. 19.

SeisSpace® ProMAX® Software Family.

Stainsby, S. D. and M. H. Worthingtont (1985). "Q estimation from vertical seismic profile data and anomalous variations in the central North Sea". In: *Geophysics*.

The Rock Physics Handbook (2009). Cambridge University Press.

York, S.D., C.P. Pong, and T.H. Joslin (1992). "Reservoir Management of Valhall Field, Norway". In: *Journal of Petroleum Technology* Volume 44, Number 8.

A   Appendix

Deepender™ 5000-X Hydrophone

Hydrophone mounted (bonded) in 4C SubSea Digitizer

Features

- Cylindrical Piezoelectric pressure sensor element
- <1.5 dB change in sensitivity from 0 to 3500 meter water depth
- 5,000 psi pressure rating

DEEPENDER 5000-X

GENERAL SPECIFICATIONS: (*Document No. 592-00320-01*)

Sensitivity (Free Field Voltage)	4.0 µV/µbar	-208.0 +/-2 dB re 1V/µPa
Sensitivity (Free Field Charge)	-181.9 +/-2.5 dB re 1nC/µPa	
Sensitivity verses Depth	<1.5 dB from 0—11,480 feet	0—3,500 meter
Frequency Response	3 Hz to 15 KHz	
Capacitance	20.0 nF +/- 35%	
Maximum Operating Pressure	5,000 psi	34.5 MPa
Operating Temperature	14 to 167 °F	-10 to 75 °C
Outside Diameter	2.0 inch	50.8 mm
Length	1.5 inch	38.1 mm

Note: All specifications @ 25 °C
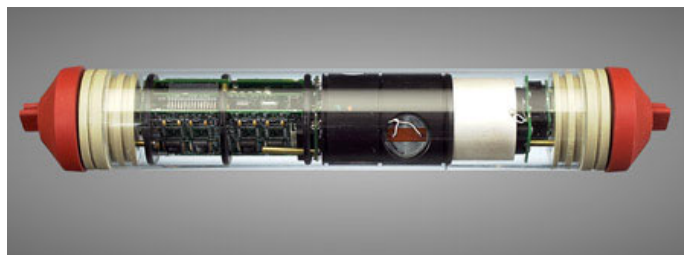
DEEPENDER 500-X mounted in SubSea Digitized 4C Sensor

GEOSPACE
ENGINEERING RESOURCES INTERNATIONAL

Reservoir Characterization Specialists

7007 Pinemont
Houston, Texas, U.S.A. 77040
Tel: 713 986-4444
Fax: 713 986-4445
www.geospacetech.com

Deepender 5000-X 032004

GEOSPACE
TECHNOLOGIES

Exploration Product Specialists